TOPOGRAPHY EFFECTS ON THE GROUND MOTION CHARACTERISTICS

A DISSERTATION

Submitted in partial fulfilment of the

requirements for the award of the degree

of

MASTER OF TECHNOLOGY

in

EARTHQUAKE ENGINEERING

(With Specialization in Soil Dynamics)

By

VISHVENDRA TIWARI

(16525015)

DEPARTMENT OF EARTHQUAKE ENGINEERING

INDIAN INSTITUTE OF TECHNOLOGY ROORKEE

ROORKEE-247667 (INDIA)

MAY, 2018

CANDIDATE'S DECLARATION

I hereby declare that the study which is being presented in this Dissertation entitled "TOPOGRAPHY EFFECTS ON THE GROUND MOTION CHARACTERISTICS", submitted in the partial fulfilment of the requirements for the award of the degree of Master of Technology in Earthquake Engineering with specialization in Soil Dynamics, Indian Institute of Technology Roorkee, is an authentic record of my own work carried out for a period from June 2017 to May 2018, under the supervision of Dr. J P Narayan, Professor, Department of Earthquake Engineering, Indian Institute of Technology Roorkee.

The matter embodied in this dissertation work has not been submitted by me for the award of any other degree or diploma.

Place: Roorkee **(Vishvendra Tiwari)**

Date: **(16525015)**

CERTIFICATE

This is to certify that the above statement made by the candidate is correct to the best of my knowledge and belief.

Place: Roorkee **(Dr. J P Narayan)**

Professor

Date:

Department of Earthquake Engineering

Indian Institute of Technology Roorkee

ABSTRACT

Surface topography consists of series of hills and valleys in the Himalayan region. These topographical features modify the seismic response of ground and play a crucial role in the design of life-line structures like dams, bridges etc. in the hilly areas. Spatial amplification and de-amplification of ground motion characteristics depends upon various phenomenon like focusing, de-focusing, scattering, reflection and diffraction of waves. In this paper, the response of number of triangular and elliptical ridge-valley models are simulated numerically using SH-wave. Finite difference algorithm developed Narayan and Kumar (2013) has been used to compute the SH-wave responses along the surface of the considered topography models. The response of multi-ridge- valley shows unusual and complex behaviour due to the diffraction, scattering, reflection, focusing and de-focusing of waves. The obtained ground motion level is highly different at the crest of ridge and base of valley as compared to those obtained using single ridge or valley. In multi-ridge-valley system, ground motion response for any hill or valley is influenced by its shape as well as the features of neighbouring valleys or ridges. For the same shape-ratio, more amplification is obtained at the crest of triangular ridge than elliptical ridge. The inferred complex behaviour of multi-ridge-valley topography suggests to go for even more complex topography models in order to explain the observed amplification/de-amplification pattern along the surface of topography during an earthquake.

ACKNOWLEDGEMENT

With respect, I express my gratitude to my guide Dr. J P Narayan, Professor, Department of Earthquake Engineering, Indian Institute of Technology Roorkee, for his valuable guidance, co-operation and untiring encouragement at all levels of work. Without his support, completion of this dissertation work would not have been possible. I am honoured to work under him.

I also want to extend my thanks to research scholars, Mr. Neeraj Kumar and Mr. Luv Joshi for their valuable inputs during project.

Lastly I would like to thank my parents and friends for motivation and constant support without which project would not have been completed.

CONTENTS

LIST OF FIGURES

LIST OF TABLES

CHAPTER #1

INTRODUCTION

1.1 GENERAL

Ground motions from earthquakes are known to be affected by earth's surface topography. Topographic effects are a result of several physical phenomena such as the focusing or defocusing of seismic waves reflected from a topographic feature and the interference between direct and diffracted seismic waves. This typically causes an amplification of ground motion on convex features such as hills and ridges and a de-amplification on concave features such as valleys and canyons. There have been cases where unusually high peak ground accelerations (PGAs) were observed in the vicinity of a topographic feature. An example of such an amplification is the recording at the Tarzana site from the 1994 Northridge earthquake where a PGA of 1.8 g was observed, whereas the neighbouring regions recorded PGAs of less than 1g. Numerical studies confirmed that these amplifications were caused due to the topography at the site. There are several other cases where the evidence of topographic amplification was observed in the form of uneven damage distribution in the neighbouring regions. In most of these cases, buildings that were located on the hilltops suffered much more damage than buildings that were located on the base region. Examples of such earthquake are the Lambesc earthquake (France 1909), the San Fernando earthquake (1971), the Friuli earthquake (Italy 1976), the Irpinia earthquake (Italy 1980), the Chile earthquake (1985), the Whittier Narrows earthquake (1987), The Aegion earthquake (Greece 1995) and the Athens (Greece 1999) earthquake, the Eje-Cafetero earthquake (Colombia 1998), and the Bingol earthquake (Turkey 2003).Topographic effects are known to be frequency dependent and the spectral accelerations can sometimes reach high values causing significant damages to the structures located on the feature. A number of researchers have studied the effects of topography on ground motions using numerical and analytical schemes (Narayan et al, 2018). These studies provide valuable insights into the physics behind the observed effects, and show that a number of factors influence the magnitude of amplifications observed at the surface and the frequencies at which these effects are observed. These factors include: the type of the incident wave, wavelength, the angle of incidence, slope angles, and soil stratigraphy. Numerical

analyses however have certain limitations. Most of the numerical studies are performed using an idealized 2D geometry with simple soil layering and properties. As a consequence, they often under-predict the amplifications observed in the field (Geli et al., 1988). A few studies have used more realistic 3D models of a terrain to compute amplifications due to surface topography (e.g., Lee et al, 2009; Chaljub et al., 2010; Maufroy et al., 2012). Though, such studies are able to predict the effects observed in the field more accurately, they are usually more computationally expensive to perform than the 2D studies (Chaljub et al., 2010).

Currently, most of the people are using fourth-order staggered-grid finite-difference (FD) method to simulate the ground motion characteristics (Kumar and Narayan, 2008). The finite difference method belongs to the grid-point methods. In the grid point methods a computational domain is covered by a space-time grid and each function is represented by its values at grid points. The space time distribution of the grid points may be arbitrary but it significantly affects the accuracy of the approximation. Usually, no assumption is made about the values in between the grid points. A derivative of a function is approximated by finite difference formula which uses values of a function at a specified grid points.

Due to its definition, the finite difference method is one of the most important numerical methods in seismology and certainly still dominant in earthquake ground motion modelling. It is applicable to complex models, and is relatively accurate and computationally efficient. Also, it is relatively easy to encode. Since the finite difference operators are local, the method enables parallelization. Moreover, due to the difficulty in application of boundary conditions, its application to complex models still requires much more elaboration. Time domain finite difference modelling is generally used.

A staggered grid time domain finite difference program was used for the simulation of SH wave propagation in the viscoelastic homogenous medium for different shape ratios and quality factors. The material through which the wave propagates is assumed to be viscoelastic and homogeneous. A set of receivers are applied to record the response on the free surface along the hill. A line source is generated at some depth using Gabor pulse. The simulated responses are analysed in both time domain and the frequency domain for different shape ratios and quality factors.

1.2 OBJECTIVES

- To study the effect of shape ratio of ridge on the amplification factor.
- To study about the spectral amplification and de-amplification in single and multi-ridges.
- To study about the spectral amplification and de-amplification in single and multi-valleys.

1.3 ORGANIZATION OF THE THESIS

The thesis has been divided into 5 chapters. Chapter 1 gives a brief introduction to the thesis. It also justifies the need for the present study and further lays emphasizes the objectives of work. Chapter 2 provides the summarized literature review of the work done in the field, and the factors which effect of topography on ground motion characteristics. Also, it highlights finite difference method. Chapter 3 contains SH-wave response of single and multi-ridges for triangular and elliptical shapes. Chapter 4 contains SH-wave response of single and multi-valleys for triangular and elliptical shapes. Chapter-5 contains conclusions based on numerical modelling of multi-ridges and valleys.

CHAPTER #2

TOPOGRAPHIC EFFECTS: A LITERATURE REVIEW

2.1 OBSERVATIONAL AND EXPERIMENTAL STUDIES

Boore(1972), in his discussion on the observed evidence of topographic effects, revisited some cases where the induced vertical ground accelerations locally exceeded gravity and resulted in regions of churned, overturned ground and boulders. These events included the Indian earthquake of 1897 (Richter, 1958), the Cedar Mountain earthquake of 1932(Gianella and Callaghan, 1934), the Hebgen Lake earthquake of 1959 (Hadley, 1964), among others. They quoted Hadley (1964) who noted that these regions of churned earth were found mostly on ridges, crests, or other topographic eminences. These observations led them to identify a dependence of ground motion amplifications on topography. Since these early mentions of topographic effects, observational evidence of topographic amplifications has been found in numerous other cases (e.g., Celebi, 1987, 1991; Hartzell et al., 1994; Hatzfeldet al., 1995; Gazetas et al., 2002). These studies showed that the structures that were located on ridges suffered much more damage than those located on the base. An example of a case with a distinctive observational evidence of topographic effects was the M 7.8 Central Chile earthquake where the four to five storied buildings located on the ridges of the Canal Beagle subdivision suffered extensive damage (Celebi, 1987). Celebi(1991) studied the aftershock data from the earthquake recorded on a dense array temporarily established at Canal Beagle and found that the spectral ratios of the observed ground motions were amplified on the ridges of Canal Beagle for a frequency of 2 to 4 Hz and 8 Hz. The 2 to 4 Hz frequency range was well within the fundamental frequency of typical four to five storied buildings that suffered heavy damage during the main event.

Similar damage patterns were reported in the field during the Lambesc earthquake (France 1909), the San Fernando earthquake (1971), the Friuli earthquake (Italy 1976), the Irpinia earthquake (Italy 1980), the Chile earthquake (1985), the Whittier Narrows earthquake (1987), the Aegion earthquake (Greece 1995) and the Athens (Greece 1999) earthquake, the Eje-Cafetero earthquake (Colombia 1998) and

the Bingol earthquake (Turkey 2003) (Assimakiet al., 2005). An exception to this pattern was observed during the Whittier Narrows earthquake of California in 1987, where most of the damage was concentrated along the slopes of the hill instead of the hill tops (Kawase and Aki, 1990). Kawase and Aki (1990) suggested that this anomaly was probably a result of the combined effects of topography and critically incident SV waves.

In addition to the observational evidence of topographic effects showing non-uniform damage in the vicinity of a topographic feature, there is also ample evidence of topographic amplifications in the recorded ground motions from earthquakes. Two notable cases are the Pacoima dam abutment recording from the San Fernando earthquake of 1971 that recorded a maximum horizontal peak ground acceleration (PGA) of 1.25 g (Trifunac and Hudson, 1971) and an extremely high PGA of 1.78 g observed on a relatively gently sloped site in Tarzana, California during the M 6.7 Northridge earthquake of 1994 (Shakal et al., 1994). Both these PGAs were one of the highest recorded at the time. A number of other studies show that ground motions were typically amplified on the hill tops and ridges, with respect to the motions at the base and that these effects were frequency dependent (e.g., Davis and West, 1973; Griffiths and Bollinger, 1979; Tucker et al., 1984; Celebi, 1987). The spectral periods at which amplifications occurred were typically proportional to the size of the feature on which the recordings were made (e.g., Davis and West, 1973; Tucker et al., 1984; Celebi, 1991). Davis and West (1973) deployed several seismographs at the base and crest of Kagel.

Mountain and Josephine peak in California and recorded aftershocks from the San Fernando earthquake of 1971. They also deployed seismographs at the base, crest, and slope of Butler Mountain near Nevada and recorded the signals from cavity collapse in a Nevada Test Site detonation. They computed the crest to base ratios of the 5 percent damped pseudo-velocity spectra and found that the magnitude and periods of amplification varied with the size of the mountains. In general, frequency-dependent amplifications were observed at the crest of all the three mountains. The smallest mountain amplified the motion in a narrow range of period (peaking at 0.3 to 0.5 s), the medium size mountain amplified motions over a slightly broader range (peaking at 0.4 to 0.5 s), and the largest mountain showed less amplifications, but over a broader range of periods. A reversal of this general trend of observing highest amplifications on the ridges and hill tops was observed by Griffiths and Bollinger (1979) who noted de-

amplifications on one of the five ridges that had a less pronounced peak than the other. They believed that this was either a result of an irregular, 3D configuration of this particular ridge compared to the relatively 2D slopes on the other ridges, or a result of a combined effect of multiple ridge systems.

A few other factors have been shown to influence the magnitude of amplifications in the recorded ground motions such as the wave type, where observed amplifications were higher for horizontally polarized signals than for vertically polarized signals (Tucker et al., 1984), and the direction of the feature, where a directional resonance in the top to base spectral ratios were observed in the direction transverse to the elongation of the hill (Spudich et al., 1996).

2.2 ANALYTICAL AND NUMERICAL STUDIES

An earthquake produces different types of body (P, S) and surface waves (Rayleigh, Love). The body waves that are generated when a fault ruptures interact with the surficial layers and the surface of the earth generating surface waves (Kramer, 1996). When a topographic feature is present, the seismic waves experience focusing or defocusing and scattering. The focusing, defocusing, and the interference of the direct and diffracted wave causes wave amplifications and de-amplifications at the surface (Bard, 1999). This problem has been studied analytically and numerically by several researchers in the past. With the advent of advanced numerical techniques, researchers have been able to identify a number of factors that affect the response of a topographic feature to an incident wave. These factors include: the type of incident waves, the angle of incidence, the dimensionless frequency (fl/Vs, where f is the frequency of input motion, l is the characteristic length of the feature, and Vs is the shear-wave velocity), slope angle, smoothed curvatures, the direction of elongation of the feature, shear wave velocity structure, and the material damping, among others. Some of these numerical studies are reviewed below.

To study topographic effects, researchers have used methods such as finite difference (e.g., Boore, 1972, 1973; Boore et al., 1981; Bouckovalas and Papadimitriou, 2005), finite elements (e.g., Smith, 1975; Assimaki and Gazetas, 2004; Assimaki et al., 2005; Tripe et al,2013; Assimaki and Jeong, 2013), boundary element methods (e.g., Sanchez-Sesma et al,1982; Nguyen and Gatmiri, 2007) and discrete wave-number method (Bard, 1982; Durand et al., 1999). Some of these studies are parametric studies where the

effect of changing one or more model parameters on topographic effects is studied, while others are case studies that try to model past cases of earthquakes where topographically correlated amplifications were observed.

. A majority of case studies consider 2D models and often under-predict the observed magnitude of amplifications in the recorded ground motions (Geli et al., 1988; Bouchon and Barker, 1996). Some believe that this discrepancy in the predicted and observed amplification is a result of the numerical models lacking the complexity of the real-world scenarios (Geli et al., 1988; Bouchon and Barker, 1996), while others suggest that the choice of reference site to compute amplifications can lead to either overestimation or underestimation of the amplification factors on top of the hills (Tucker et al., 1984; Geli et al., 1988). Nevertheless, most of these numerical studies provide good qualitative estimates of the observed amplification. According to a review article by Geli et al. (1988), most of the numerical studies predicted amplifications on top of the ridges over a broad range of frequencies, and a de-amplification of the low frequency waves (for wavelengths larger than mountain width) at mountain base, with an alternation of amplification and de-amplification at higher frequencies. On mountain slopes, the phase and amplitude varied rapidly causing differential motion. In the ensuing, we look at the effects of some of the factors that have been shown to influence the ground motions in numerical studies.

2.3 FACTORS AFFECTING GROUND MOTION

2.3.1 Ridge Effects

The topographic effects caused by simple irregularities can be estimated from exact solutions to idealized problems (Aki, 1988). For a triangular infinite wedge subjected to vertically propagating SH-waves (with particle motion parallel to its axis), apex displacements are amplified for those wavelength whose wavelength matches with the width of the base of the ridge, by a factor $2\pi/\phi$, where ϕ is the vertex angle of the wedge (Figure 2.1).

Amplified ground motion = $(2\pi/\phi)A_0$

A where Φ is the ridge wedge angle in radians and A is amplitude of incident SH-wave.

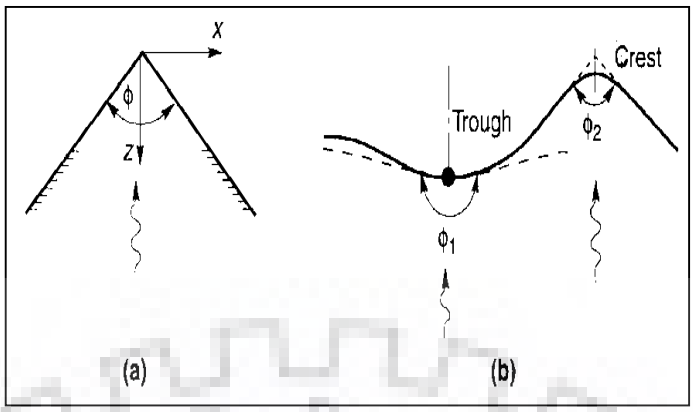

Figure 2.1 Characterization of simple topographic irregularities; (a) notation for a triangular wedge; (b) approximation of actual ground surface at trough & crest by wedges (Faccioli, 1991)

Amplitude of ground motion increases with the increase of elevation of the recording station on the same slopping side of the ridge. Increased amplification near the crest of a ridge was measured in five earthquakes in Matsuzaki, Japan (Jibson, 1987). Figure 2.2 shows how the normalized peak acceleration varied at different points along the ridge. The average peak crest acceleration was about 2.5 times the average base acceleration.

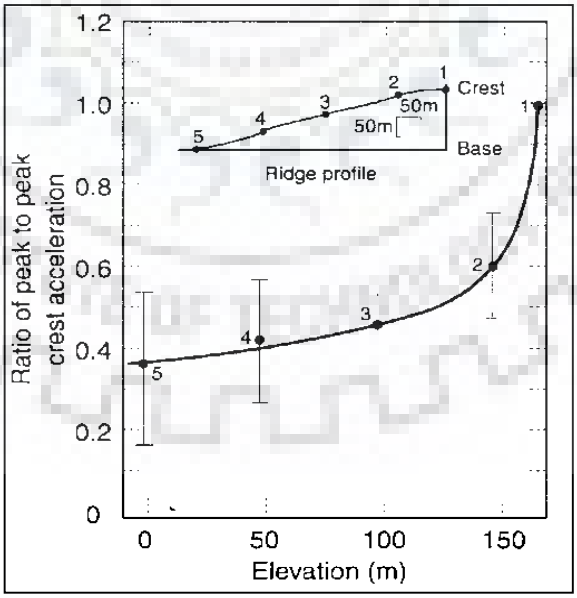

Figure 2.2 Normalized peak accelerations (means and error bars) recorded on mountain ridge at Matsuzaki, Japan. (After Jibson, 1987)

2.3.2 Valley Effects

De-amplification caused by the valley-de-focusing is frequency independent in contrast to the amplification caused by the ridge-focusing (Geli et al., 1988). In contrast to de-amplification at the trough, the valley causes amplification of all the frequencies very near its top-corners. Both de-amplification at the trough and amplification near the top-corners are larger in case of the triangular valleys as compared to the elliptical valleys.

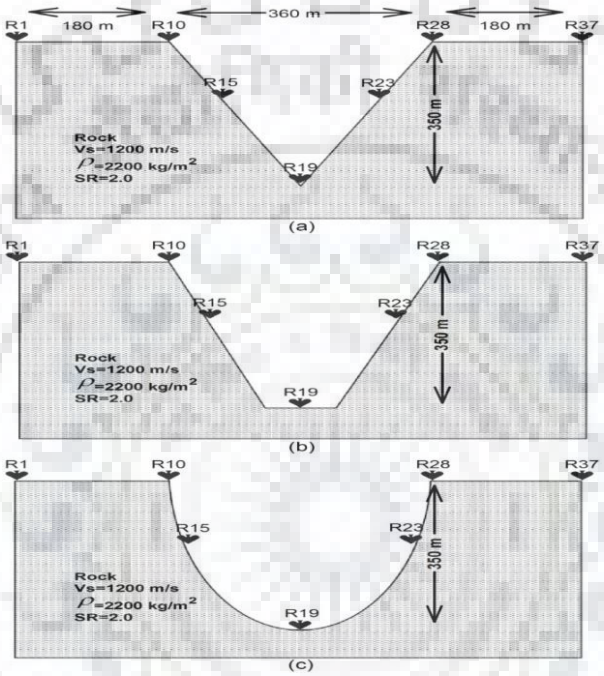

Figure 2.3(a),(b)&(c) Triangular, trapezoidal and elliptical valley models, respectively. . (NARAYAN, ARAFAT, and KAMAL, 2015)

2.3.3 Slope Variation

Complicated damage pattern have been observed on the hills with variable slopes. The houses situated on or near the bank of a steeply sloping hill suffered much more damage as compared to the houses which were at some distance from the steep portion or on the gentle sloping part of the same hill. Damage observed in lower and upper Chamoli, during the Chamoli earthquake was attributed to the effect of slope variation (Narayan and Rai, 2001). The intense damage at the higher elevation of lower Chamoli and just after the steep slope in the upper Chamoli was to some extent in accordance with the French Recommendation-AFPS 92.

2.3.4 Incident wave type

A few 2D numerical studies have compared the effects of different incident wave types (SH,P, SV) on the predicted amplification. Typically, for simple 2D slopes, amplification of the SV waves was found to be higher than the SH waves (Ashford and Sitar, 1997). In case of incident SV waves, generally a zone of amplification existed near the slope due to interaction of the primary SV and the diffracted Rayleigh waves (e.g., Boore et al., 1981; Bouchon, 1973; Wong, 1982). In addition to the nature of the input waves, its polarization also affects the response of the feature, e.g. Bouchon and Barker (1996) studied the response of a three dimensional topography to incident shear waves polarized in different directions using the boundary integral equation method. They observed that the hill produced higher amplification of ground motions when the input waves were polarized transverse to the direction of elongation of the hill compared to when it was polarized parallel to the direction of the elongation of the hill. They also observed a rotation of the polarization of particle motions from the base to the top of the hill, with particle motions being more transverse to the hill at the top than the base.

2.3.5 Angle of Incidence

Some researchers have investigated the effects of incidence angle on the topographic amplifications for cases of simple 2D topographies (Boore, 1973; Wong and Jennings, 1975; Ashford and Sitar, 1997) and suggest that it has a significant effect on the amplification of waves. Ashford and Sitar (1997) studied the response of a stepped half-space subjected to an inclined shear wave from 0 to 30 degree using generalized consistent transmitting boundaries and found that the horizontal motion at the crest of the slope is amplified for waves traveling into the slope and de-amplified for waves traveling away from the slope, in comparison to the free-field motion behind the crest of the slope. They measured the incidence angles clockwise from the vertical axis, and referred to the waves with positive incidence angle as traveling away from the slope, and those with negative angles as traveling into the slope. They also suggested that these amplifications can be twice the amplifications observed for a vertically propagating wave. A similar study on a more realistic model using inclined incident shear waves showed that even though topographic amplifications are greater for inclined waves, the magnitude of horizontal and vertical acceleration at the crest is

usually greatest for the case of vertical incidence. Boore (1973) used a simple finite difference model to study the topographic effects observed on Pacoima Dam site during the 1971 San Fernando earthquake in California. As the topography at the site of the Pacoima dam abutment recording station was complicated, they considered two site geometries to adequately represent the site: A ridge model with two angles of incidences at 0 and 45 degrees and a canyon model with vertical incident waves. They observed that the ridge model with vertical incidence produced the greatest amplification for frequencies between 3 Hz and 10 Hz. At shorter frequencies, the effect of the canyon became relatively more important and produced attenuation of wave motion.

2.3.6 Site geometry and wavelength of input motion

Past numerical studies have shown that topographic effects are more pronounced for input wavelengths that are comparable to the dimensions of the feature (e.g., Geli et al., 1988; Ashford et al., 1997; Ashford and Sitar, 1997). In addition, the slope angle has been shown to influence the amplifications observed at the crest in 2D slopes (e.g., Ashford et al., 1997; Bouckovalas and Papadimitriou, 2005; Tripe et al., 2013; Maufroy et al., 2015). In particular, Ashford et al. (1997) studied the response of steep slopes using generalized consistent transmitting boundaries and found that the topographic effects are most visible for slopes greater than 60 degrees and decrease with slope angles. Also, for a stepped layer over a half space, the response is dominated by the natural frequency of the site behind the crest. Bouckovalas and Papadimitriou (2005) performed a parametric study using a simple 2D finite difference slope model and studied the influence of slope inclination, normalized height of the slope (H/l, where H is the height of the slope and l is the wavelength), number of significant excitation cycles and critical hysteretic damping on the amplifications. They found that both slope angle and the normalized height of the slope have a significant effect on horizontal and vertical ground motions. They also found that the only effect of damping is on the distance to the free-field, while the number of significant cycles of excitation has only a minor effect overall. More recently, Maufroy et al. (2015) performed numerical analysis using a realistic 3D model of a terrain, and found that the average amplifications at a site were highly correlated with curvatures that were smoothed using a window proportional in size to the wavelength of input motion.

2.3.7 Soil Stratigraphy

Soil stratigraphy plays an important role in the surface response to input motion and can cause both amplification and de-amplifications of the wave (e.g., Assimaki and Gazetas, 2004; Assimaki et al., 2005; Assimaki and Jeong, 2013). When topography is present at the surface, the observed response is a result of a combined effects of the topography and the surface layering effects (Geli et al., 1988). Assimaki and Gazetas(2004) studied different configurations of layered soil profile in a 2D slope and found that the topographic amplification of the motion is more pronounced for a layered medium in a certain frequency range due to multiple reflections and transmissions of the vertically incident S-waves through the horizontal layers, causing an additional amplification at the crest. Assimaki and Jeong(2013) performed site-specific numerical simulations to understand the severe damage caused during the 2010 M 7 Haiti earthquakes and found that the observed amplifications were most likely caused by a combined effects of soil layering and topographic amplifications.

2.4 SUMMARY

An extensive literature review on topographic effects has been done in the past so we consolidate the findings from these studies and summarize them as following:

➢ In the time domain, grounds motions are amplified on convex features such as hill tops and ridges and de-amplified on concave features such as valleys and canyons. In the frequency domain, a broadband amplification of ground motions occurs on the top of the hill and a de-amplification occurs at the base with alternating amplification and de-amplification at higher frequencies. On the slopes, the amplitude and phase vary rapidly causing a differential motion.

➢ Ridge Effect

- The maximum amplification corresponding to the wavelength equal to width of ridge may be larger than that predicted analytically (Faccioli, 1991).
- Amplification decreases with increase of angle of incidence of body waves.

- On an average, there is increase of amplification with elevation and slope of the ridge. The numerically obtained an increase of ASA with an increase of the shape-ratio supports this, particularly for the low frequency range.
- The frequency content of the input motion is also a key parameter. It is observed that for long wavelengths, i.e. very low frequencies, topographic effects are negligible, while the effects become significant for wavelengths comparable to the geometric characteristics of the relief.
- The presence of neighbouring ridges increases the topographic effects.
- Interference between the incident waves and outgoing diffracted waves produces rapidly varying amplitude and phase, and thus differential motions along the slope of the topography.

➢ Valley Effect

- The de-focusing caused by the valley is frequency-independent.
- In contrast to de-amplification at the trough, the valley causes amplification of all the frequencies very near its top-corners.
- For an equal shape-ratio, the valley de-amplification at the trough and amplification at the top-corners are larger for the valley whose surface area is lesser.
- There is decrease of the spatial variations of average ASA for both the non-weathered triangular and elliptical valleys with an increase of the shape-ratio.
- Both de-amplification at the trough and amplification near the top-corners are larger in case of the triangular valleys as compared to the elliptical valleys.

➢ There is a qualitative agreement between theory and observation regarding the existence of ground motion amplification; however, the amplitude of such effects is mostly under-predicted in numerical analyses. This under-prediction is believed to be a result of the numerical models not being complex enough. Some believe that this under predictions a result of an inappropriate selection of the reference station in the field for computing amplifications.

➢ Topographic effects are prominent for wavelengths comparable to size of the irregularity. For wavelengths larger than the dimensions of the feature, amplifications are negligible.

➢ The magnitude of crest to base amplification ratios depends on the ratio of mountain height to mountain half width which is called shape ratio and found to be proportional to this ratio. The amplifications also depend on the angle of incidence of the incoming wave, more so at the near critical incidence.

➢ The amplifications are also affected by incident wave type. The amplifications are typically larger for horizontal components than for vertical component of the motion. The amplifications were however not found to be affected by the damping ratio of the soil and the duration of the motion.

➢ In numerical studies using more realistic topographic, amplifications were found to be strongly correlated to frequency-scaled curvatures.

➢ Topographic amplifications are affected by soil stratigraphy. In particular, amplifications are magnified in the presence of soft, shallow soil layers.

➢ With increasing slope angle, the tangential stress increases which result in increase in shear stress thus reducing its stability.

➢ With increasing angle of shear resistance seismic slope stability decreases.

2.5 FINITE DIFFERENCE METHOD

2.5.1 General

In this chapter, we have discussed the finite difference scheme that has been used to compute the seismic responses of a horizontal array of receiver at free surface in homogeneous models. The finite-difference method is a robust numerical method applicable to structurally complex media. Due to its relative accuracy and computational efficiency, it is the dominant method in modelling earthquake motion. It is also becoming increasingly more important in the seismic industry and for structural modelling. Numerical simulation of seismic wave propagation is carried out using standard methods of solving partial differential equations that appear in different branches of science and engineering. There are some inherent limitations of the method which makes its application to complex models a little difficult. Also, if the finite difference method is used as a black box method, which, unfortunately, is not the unusual case, the method can give considerably inaccurate results. Finite difference (FD) is the most widely used numerical approach. FD-based methods still remain very popular due to the ease of their implementation, computational efficiency and relative accuracy. The application of the method for a particular differential problem includes:

1. Construction of a discrete FD model of the problem
2. Analysis of the FD model
3. Numerical computation

The analysis of the FD model or numerical computation may lead to redefinition of the grid and FD approximations, if numerical behaviour is not satisfactory. The SH-wave responses of the model have been computed using a fourth-order accurate finite-difference program (Narayan and Kumar, 2013).

2.5.2 Salient features of used FD algorithm

A frequency-dependent damping in the time-domain simulations of responses of models is essential for accurate prediction of ground motion characteristics. A forth-order accurate SH wave viscoelastic FD programs have been used for the simulation of responses of the considered various models (Narayan and Kumar, 2013). Figure 2.4 shows the staggering technique, where particle velocity and the density are defined at

the nodes and the shear stresses, unrelaxed modulus of rigidity, an elastic coefficients and anelastic functions are defined at the midway between the two adjacent grid points.

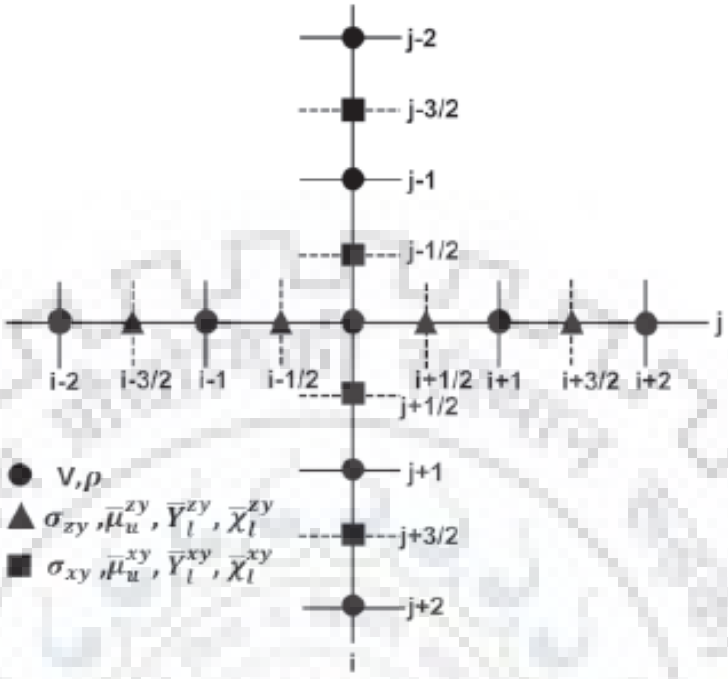

Figure 2.4 Staggering technique for SH-wave modeling with fourth order spatial accuracy (Narayan and Kumar, 2013)

The frequency-dependent damping in the FD simulations is incorporated based on the GMB-EK rheological model (Emmerich and Korn, 1987). In the stress-strain relations, material independent anelastic functions have been used since it is beneficial in case of material discontinuities in the model. The details of computations of the unrelaxed moduli (MU), anelastic coefficients (Yl) and anelastic functions (cl) are given in Narayan and Kumar (2013). The effective values of the unrelaxed Lame's parameters and density at the desired location in the staggered-grid are obtained using the harmonic and arithmetic means, respectively.

2.5.3 Discretisation of model

The FD solution is a discrete approximation of a true solution. The phase and group velocities in the grid in general differ from the true velocities in the medium. Grid dispersion is a very important grid phenomenon. It has a cumulative effect on wave propagation, the longer the travel distance, the larger the effect of the difference between the grid and true velocity. Therefore, grid dispersion has to be analysed prior to

the numerical calculations. Given the desired travel path, one has to choose appropriate spatial sampling of the minimum wavelength to be propagated with a desired level of accuracy. The grid velocities depend on the spatial sampling ratio s=Δx/λ, where λ is the wavelength that is to be propagated in the grid. Studies reveal that at least 5 or 6 grid spacing should be used to sample the wavelength λ in order to avoid grid dispersion of the phase velocity and group velocities for wavelength λ in 4th order approximation. In this study, we take 6 grids spacing to sample the minimum wavelength λ_{min}.

$$\lambda_{\min} = 6\Delta x \tag{2.1}$$

The grid dispersion relation, that is, the relation between grid velocity, spatial grid spacing, time step and material properties can be obtained from stability analysis. The stability condition for the SH wave FD simulation of 4th order spatial accuracy is given by

$$\frac{V_{\max}\Delta t}{\min(\Delta x or \Delta z)} = \frac{6}{7\sqrt{2}} \tag{2.2}$$

2.5.4 Source implementation

A plane horizontal SH-wave front is generated in the FD numerical grid at some depth, using various point sources along a line. A particular point source was generated using shear stress σ_{ZY} in the form of Gabor wavelet. The mathematical form of the Gabor wavelet is given below:

$$S(t) = Exp(-\alpha)\cos(\omega p(t - t_s) + \varphi) \tag{2.3}$$

Where $\alpha = \left(\frac{\omega p(t-ts)}{\gamma}\right)^2$, f_p is predominant frequency, γ controls the oscillatory character, t_s controls the duration (duration =2 t_s) and ϕ is phase shift the generated. The frequency content in the Gabor wavelet is 0- 15.0 Hz. The Gabor wavelet used for the purpose of the study has f_p= 5 Hz, t_s= 0.0016 s, γ=1.5 and ϕ=0.

2.5.5 Free surface boundary condition

Free-surface boundary condition is one of the most important factors governing the accuracy of elastic wave modeling technique. Free surface boundary condition can be achieved using either the stress imaging technique (Levander, 1988; Graves, 1996; Gottschammer and Oslen, 2001) or the vacuum formulation (Boore, 1972; Zahradnik et al., 1993; Oprsal and Zahradnik, 2002). In this study, we have used the vacuum formulation technique. In the vacuum formulation, the values of elastic parameters are set to zero and density is reduced marginally above the free surface. This approach is attractive because it can be implemented with the same finite difference equation as used in the interior of the model.

2.5.6 Absorbing boundary condition

Because of the limited available computer memory, the numerical models have a certain fixed dimension. The waves travelling through the grid of the model are reflected back from the model edges, known as edge reflections. To avoid these edge reflections, non-reflecting boundaries or absorbing boundary conditions are applied along the edge of the model. The Clayton and Engquist(1977) boundary condition and sponge absorbing boundary condition (Israeli and Orszag, 1981) is implemented on the model faces up to 200 grids from all the edges, to avoid the edge-reflections.

CHAPTER #3

QUANTIFICATION OF COMPLEX HILL TOPOGRAPHY EFFECTS ON THE GROUND MOTION CHARACTERISTICS

3.1 INTRODUCTION

The extensive literature review on the ridge-topography effects on the ground motion reveals that most of the researchers have used a single ridge with different shape-ratio. In most of studies the reported amplification caused by the ridge is less than 3.0. On the other hand, the reported ridge-amplification based on the records reveals the level of amplification even more than 10-15. In order to infer the possible reasons for the failure of the theoretical studies to under predict the ridge-amplification, a complex ridge-topography model has been considered. The SH-wave responses of the considered complex triangular and elliptical ridge-topography models have been computed and analysed in this chapter.

3.2 DISCRETIZATION OF MODELS AND INPUT PARAMETERS

The first step for the spatial and temporal discretization of model is to fix the grid size. Grid size is calculated by satisfying the stability conditions given for the fourth order approximation in homogenous medium. Condition for grid dispersion is also satisfied. Grid size should be equal to one-sixth of the shortest wavelength of interest in the fourth order FD approximation.

$V = f^{*}\lambda$

V= velocity of SH-wave

f= highest frequency in the frequency band

λ= shorted wavelength of SH-wave

After satisfying required conditions, the obtained minimum grid size is 4 m.

Minimum grid size is necessary to avoid grid dispersion and to incorporate geometry of topography model in the numerical grid. The considered numerical model is in north and vertical direction. Total size of models in north direction is 6000 m. Uniform grid size of 4 m is taken in north direction. Absorbing boundary conditions (dampers) are applied from 0-800m and then from 5200-6000m in the horizontal direction. In between these two boundary conditions main model lies.

Total size of models in the vertical direction is 5750 m. varying grid size is taken in vertical direction as 4 m up to 1500 m and 10 m thereafter. Dampers are applied from 3750-5750m in the vertical direction at the bottom. Free surface is taken at 1200m from top in homogenous and ridge models. There is air above free surface and below is rock. Density in air is assumed as one-tenth of density of rock.

The plane wave front of the SH-wave have been generated by using shear stress in the form of Gabor wavelet at a depth of 550 m below the free surface. 5Hz dominant frequency is taken for Gabor wavelet for which frequency band is 0-15 Hz. The time step is taken as 0.0016 sec to avoid the stability problem. The value of SH-wave velocity at a reference frequency (Fr=1), density and quality factor for the homogenous visco-elastic medium have been given in table 3.1. Quality factor is taken as 10% of SH-wave velocity. The unrelaxed moduli and the anelastic coefficients for both Rock and air have been calculated at four relaxation frequencies of 0.02, 0.2, 2, 20 Hz and given in table 3.2

Table 3.1 Parameters for homogenous visco-elastic material

Material	Density(kg/m^3)	V_S(m/s)	Q_s
Rock	2000	1500	150

Table 3.2 Computed input parameters

Material	Unrelaxed moduli (Pa)	Anelastic coefficients			
Air	10^{-9}	0	0	0	0
Rock	4588780790	0.01091	0.00933	0.00944	0.01148

3.3 SH-WAVE RESPONSE OF HOMOGENOUS MODEL

To compare the effects of ridge topography, first response of ground motion without topography is computed and analysed. Figure 3.1 shows the homogenous model named PLANE. 51 Recorders are placed from -1000m to 1000 m at an interval of 40 m spacing.

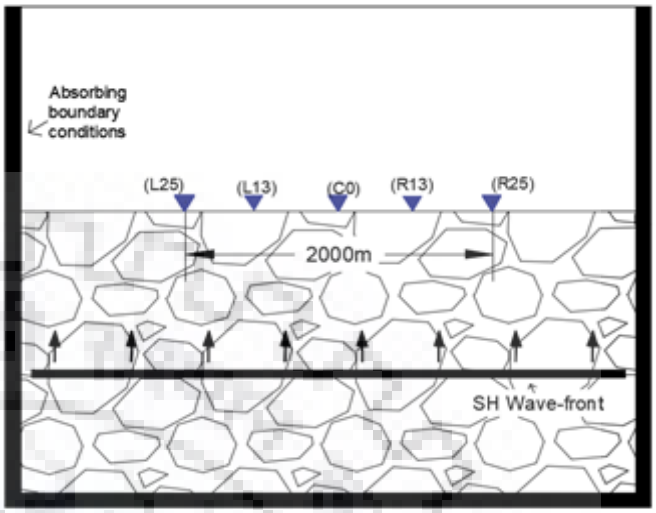

Figure 3.1 Homogenous half-space model

Figure 3.2 shows the SH-wave response of homogeneous model at different receiver points. Analysis of figure 3.2 reveals that the amplitude is same for all the receiver points at surface, which is obvious for homogenous medium.

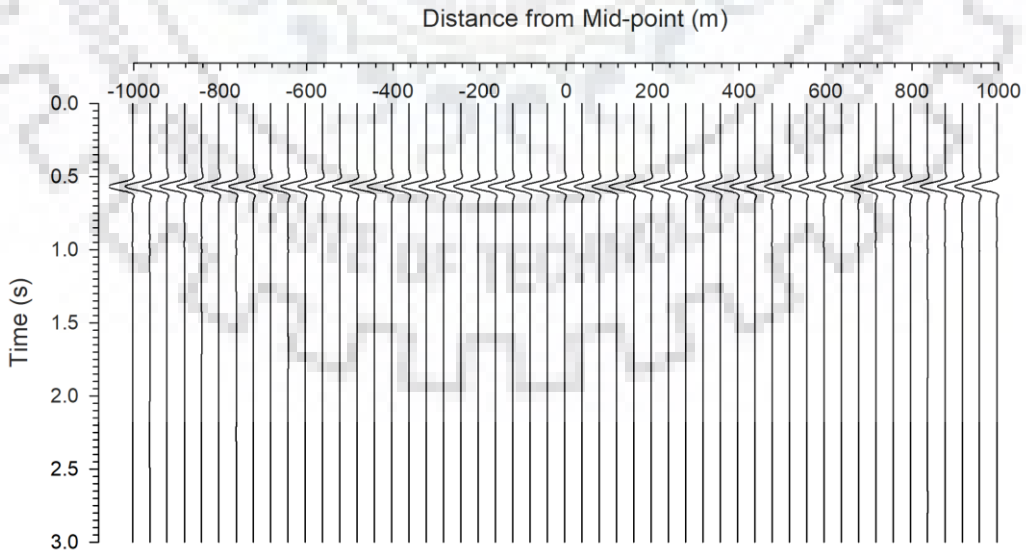

Figure 3.2 SH-wave response of the homogeneous half-space model

Figure 3.3 shows the variation of spectral amplitude of SH-wave with respect to frequency for central receiver C0. The frequency bandwidth for generated wave is 0-15 Hz. The dominant frequency is 5 Hz. Figure clearly shows that spectral amplitude stays almost constant at lower frequencies and gradually decreases as frequency increases

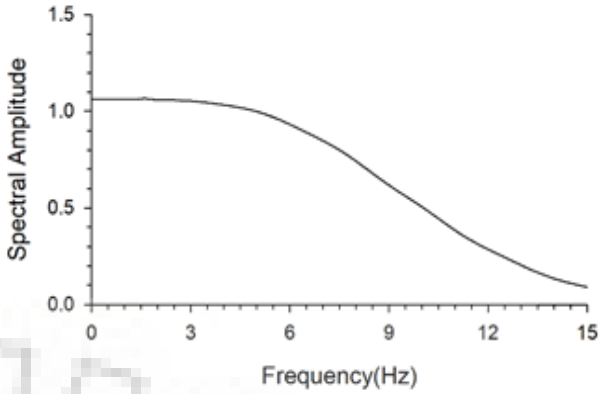

Figure 3.3 Spectra of recorded ground motion

3.4 SH-WAVE RESPONSE OF TRIANGULAR RIDGES

Table 3.3 Ridge models

TR1	Single triangular ridge	ER1	Single elliptical ridge
TR3	Three triangular ridge	ER3	Three elliptical ridge
TR5	Five triangular ridge	ER5	Five elliptical ridge
TR7	Seven triangular ridge	ER7	Seven elliptical ridge

Four triangular and elliptical ridge models have been considered with one, three, five and seven ridges as given in the table. The overall dimension of all the ridge models is same. Further, the position of receiver array and source are also same.

3.4.1 SH-wave response of single triangular ridge

To see the response of single triangular ridge, the considered model is named as TR1 with a single triangular ridge. 51 Recorders are placed from -1000m to 1000 m at an interval of 40 m spacing. We have considered ridge of height of 1000m and width 2000 m i.e. shape ratio of hill is 1.0

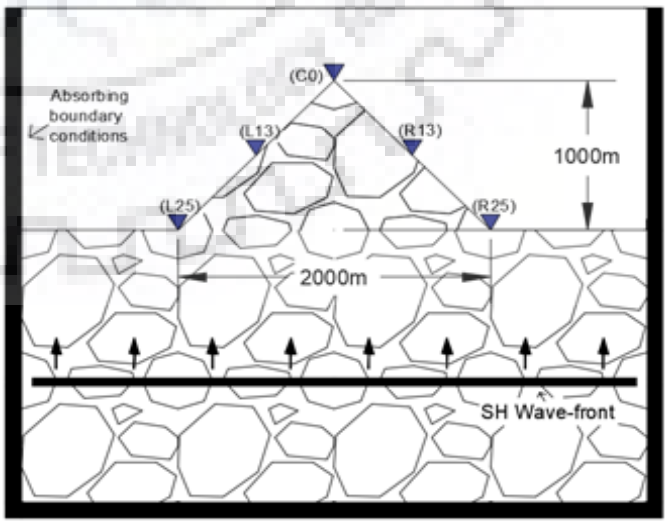

Figure 3.4 Single triangular ridge model (TR1)

(a) Time domain response

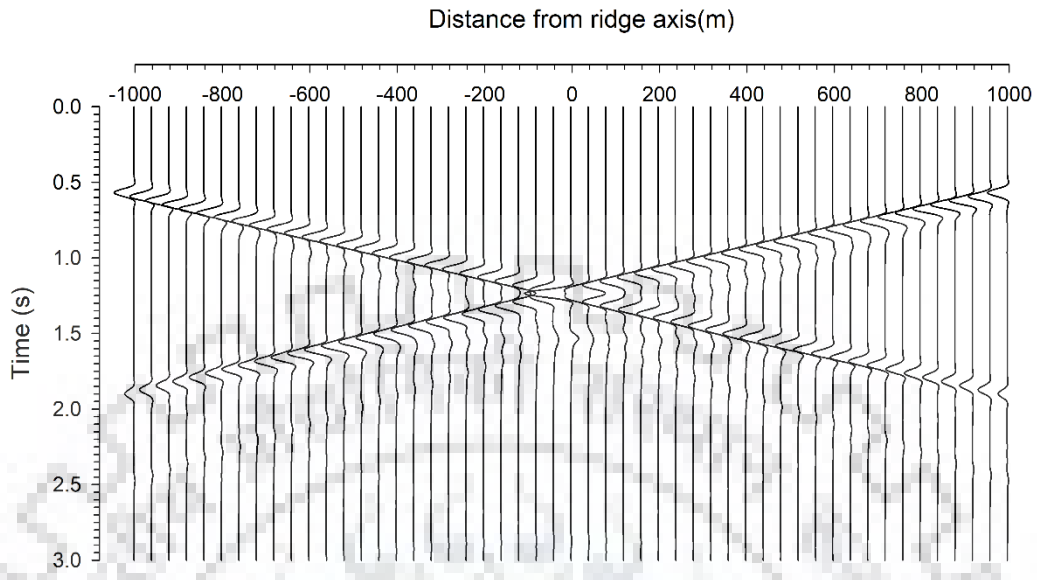

Figure 3.5 Particle velocity response for the TR1 model

The seismic response of the TR1 model is shown in figure 3.5. The analysis shows the amplification of seismic response at the crest of ridge compared to homogenous half-space model. Figure 3.5 shows that maximum amplitude occurs at the crest of ridge due to focusing of waves. The incident SH-wave and the diffracted waves from the base-corners are very clearly visible.

(b) Snapshots of wave-field

To infer the behavior of SH-wave after interacting with the ridge topography, snapshots have been computed at different moments from 0.5s to 2.25s and shown in Fig 3.6. It can be seen from snapshots that as wave-front moves upwards, it is reflected by ridge topography and it reaches the crest of ridge at time 1.25s hence maximum amplitude is shown there. The snapshot at time 0.5s shows only the incident wave in the considered area. The snapshot at time 0.75s shows the incident plane wave front as well as the reflected waves from the flanks of the triangular ridge. The incident, diffracted and reflected waves are annotated in snapshot at time 1.0s. The snapshot at time 1.25s clearly illustrates that the incident and reflected waves from the flanks are reaching simultaneously along the ridge axis. This is the reason for the very large amplitude at

the ridge top in case of a symmetrical triangular ridge. The reflected diffracted waves are only phases present in the snapshot at time 2.0s.

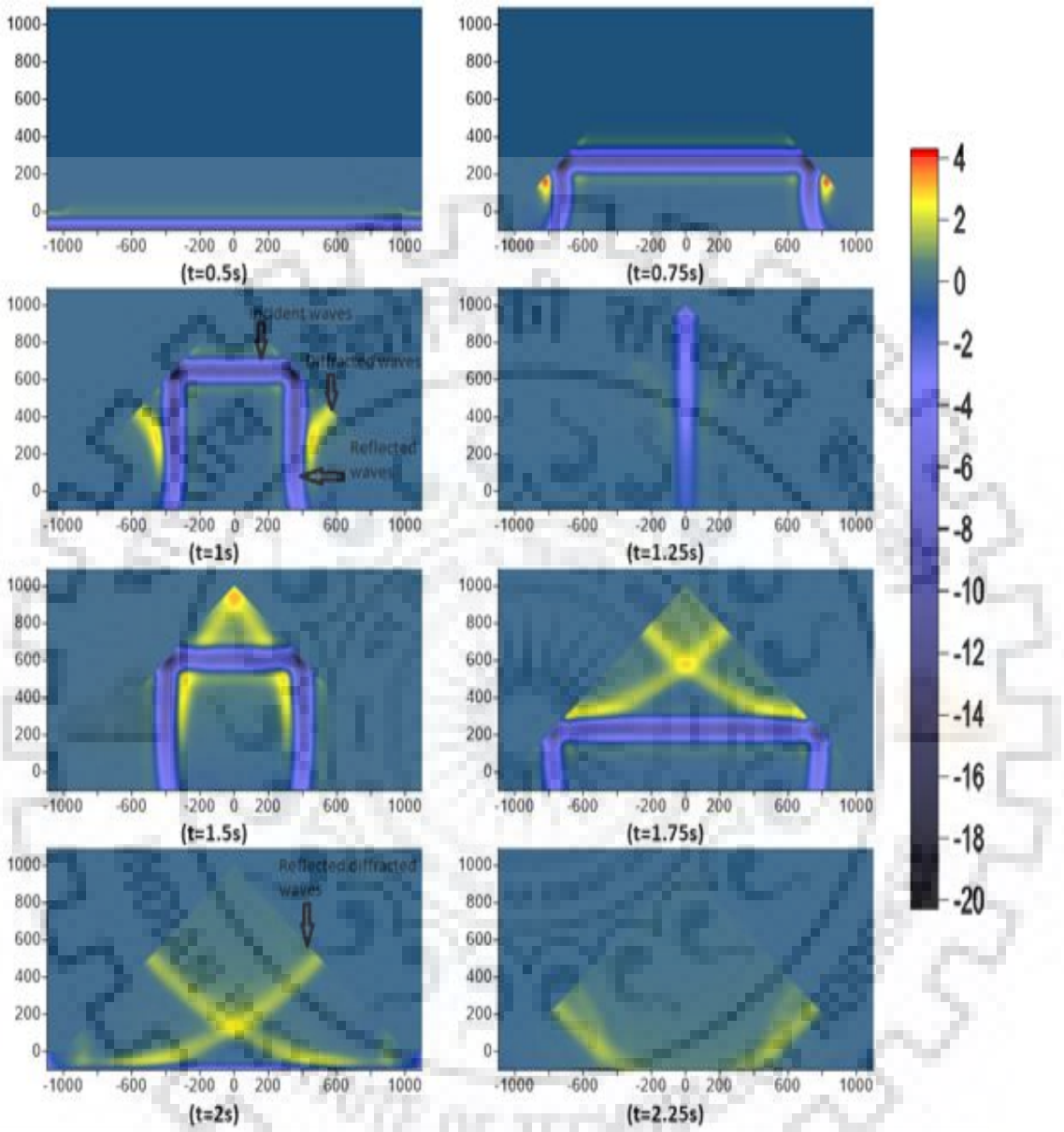

Figure 3.6 Snapshots of SH-wave at different moments for TR1 model

(c) Spectral amplification factor

Figure 3.7a&b shows the spectral amplification factor of TR1 at L13 and C0 recording point, respectively which is found by dividing the spectral amplitude of TR1 to that of half-space model at that corresponding location.

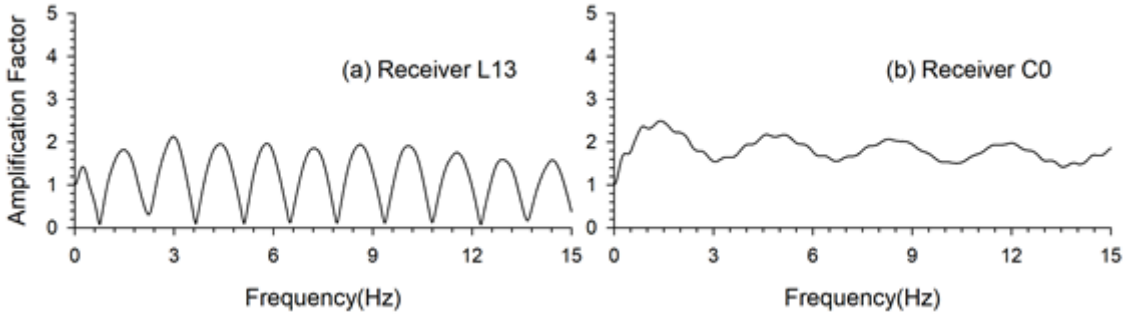

Figure 3.7 Spectral amplification factor at two locations for TR1 model

Table 3.4 A comparison of spectral amplification factor (SAF), average spectral amplification (ASA) at different receiver points with the analytical one

Receiver location	L13	C0
Largest SAF: Numerical value	2.1	2.28 at 0.75Hz
Average SAF: Numerical value	1.178	1.82
SAF : Analytical value	---	2.0 at 0.75Hz

The largest SAF for wavelength matching with the width of the base of the ridge can be obtained analytically as

$\pi/\varphi=2.0$ Apex angle $\varphi=90^0$

at frequency $f=V/\lambda$ Velocity of SH-wave V= 1500m/s

f=1500/2000 = 0.75Hz Width of hill base λ= 2000m

An analysis of table 3.4 reveals that the largest obtained SAF numerically is 2.28 at frequency 0.75Hz which is larger than that of obtained analytically (2). Analytical value of amplification factor is found lesser than numerical value. This may be because of non-consideration of diffracted waves in the analytical solution.

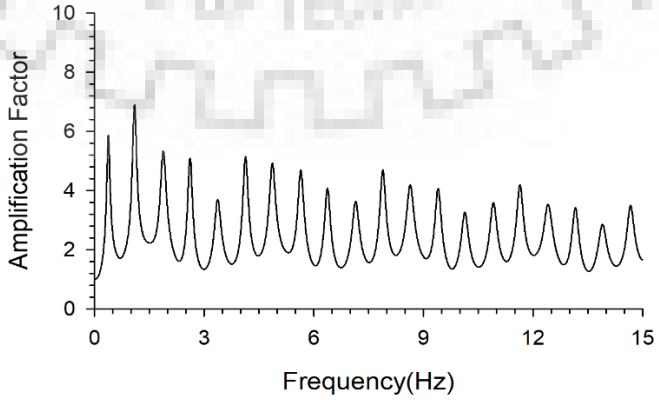

Figure 3.8 Spectral amplification at the top of ridge wrt the record at the base

The spectral amplification at the top of ridge wrt the record at the base, as shown in figure 3.8, depicts that the largest SAF is 6.86 at frequency 1.07 Hz. This is much larger than the same obtained using numerical/analytical one. So, it may be the reason behind the reported very large amplification in the case of amplification computed using the record at the top and base of the ridge.

3.4.2 SH-wave response of three triangular ridges

A topography model with three triangular ridges is shown in figure 3.9. The SH-wave response of the model is computed at 51 Recorder points, extending from -1000m to 1000 m at an interval of 40 m spacing in the horizontal direction. The height and width of this multi-ridge model 1000m and 2000m, respectively.

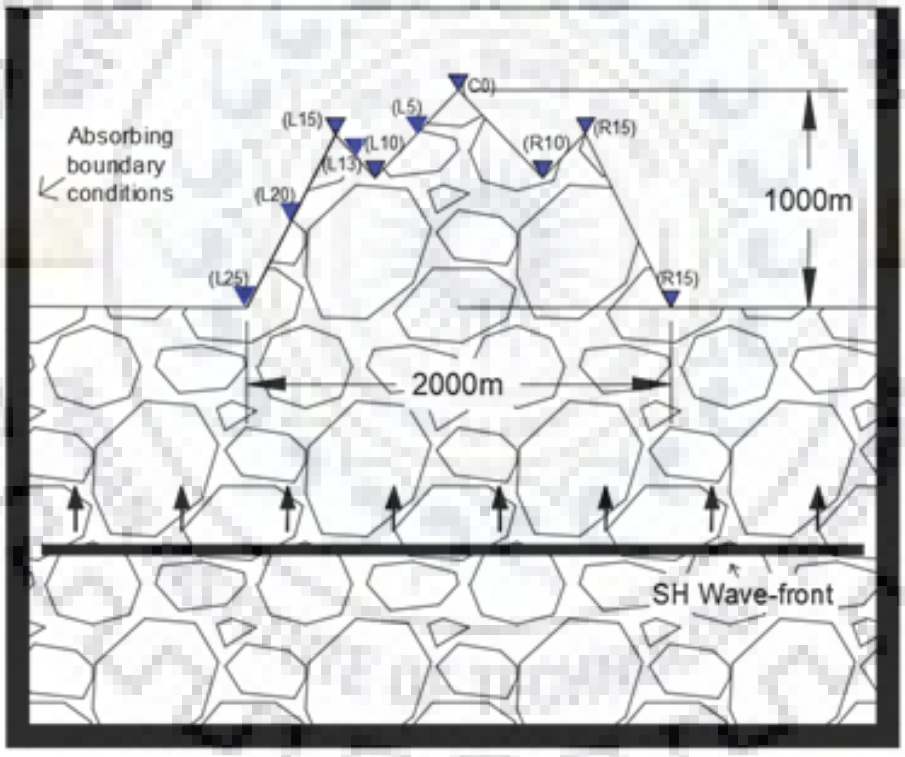

Figure 3.9 Three triangular ridges model (TR3) along with receivers array

(a) Time domain response

The seismic response of the TR3 model is shown in figure 3.10. The analysis of this figure shows the amplification of SH-wave at the crest of ridges and de-amplification of the SH-wave at base of the valleys as compared to the amplitude in the case of

homogenous half-space model. Figure 3.10 shows that maximum amplitude occurs at the crest of ridge and minimum amplitude at the base of the valley due to focusing and de-focusing of the SH-waves, respectively. The incident SH-wave and the diffracted waves from the base-corners of the ridges/top corners of the valley are very clearly visible. An increase of duration of ground motion in the case of complex ridge topography as compared to the solo-topography model can be inferred.

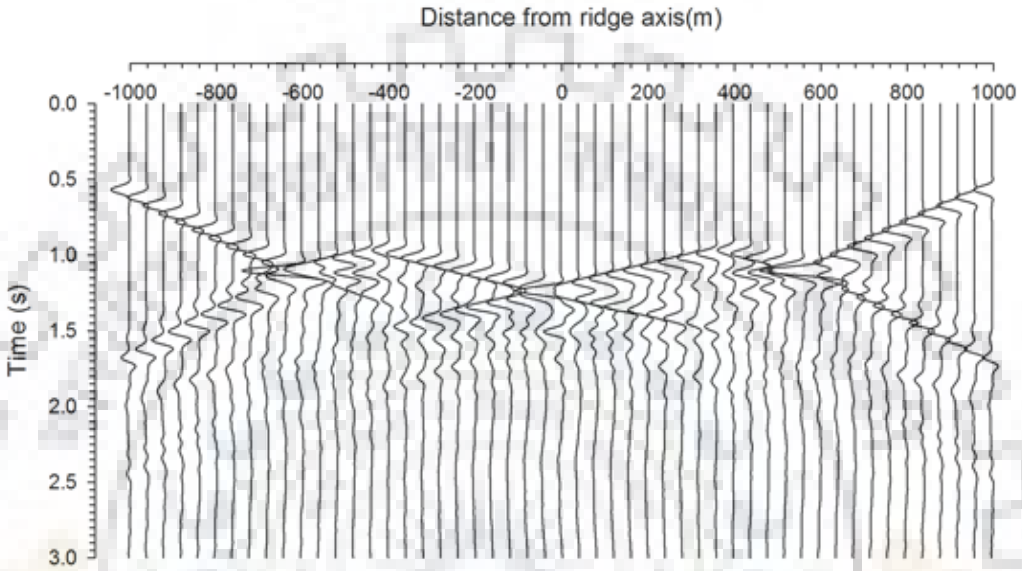

Figure 3.10 SH-wave response of the TR3 ridge topography model

(b) Snapshots of wave-field

To infer the behaviour of SH-wave after interacting with the complex ridge topography, snapshots have been computed at different moments from 0.5s to 2.25s and shown in Fig 3.11. The snapshot at time 0.5s shows only the incident wave in the considered area. The snapshot at time 0.75s shows the incident plane wave front as well as the reflected waves from the flanks of the outer triangular ridges. The incident, diffracted and reflected waves are annotated in the snapshots. A comparison of this snapshot with that of a solo-topography reveals very complex wave fronts due to the presence of multiples ridges.

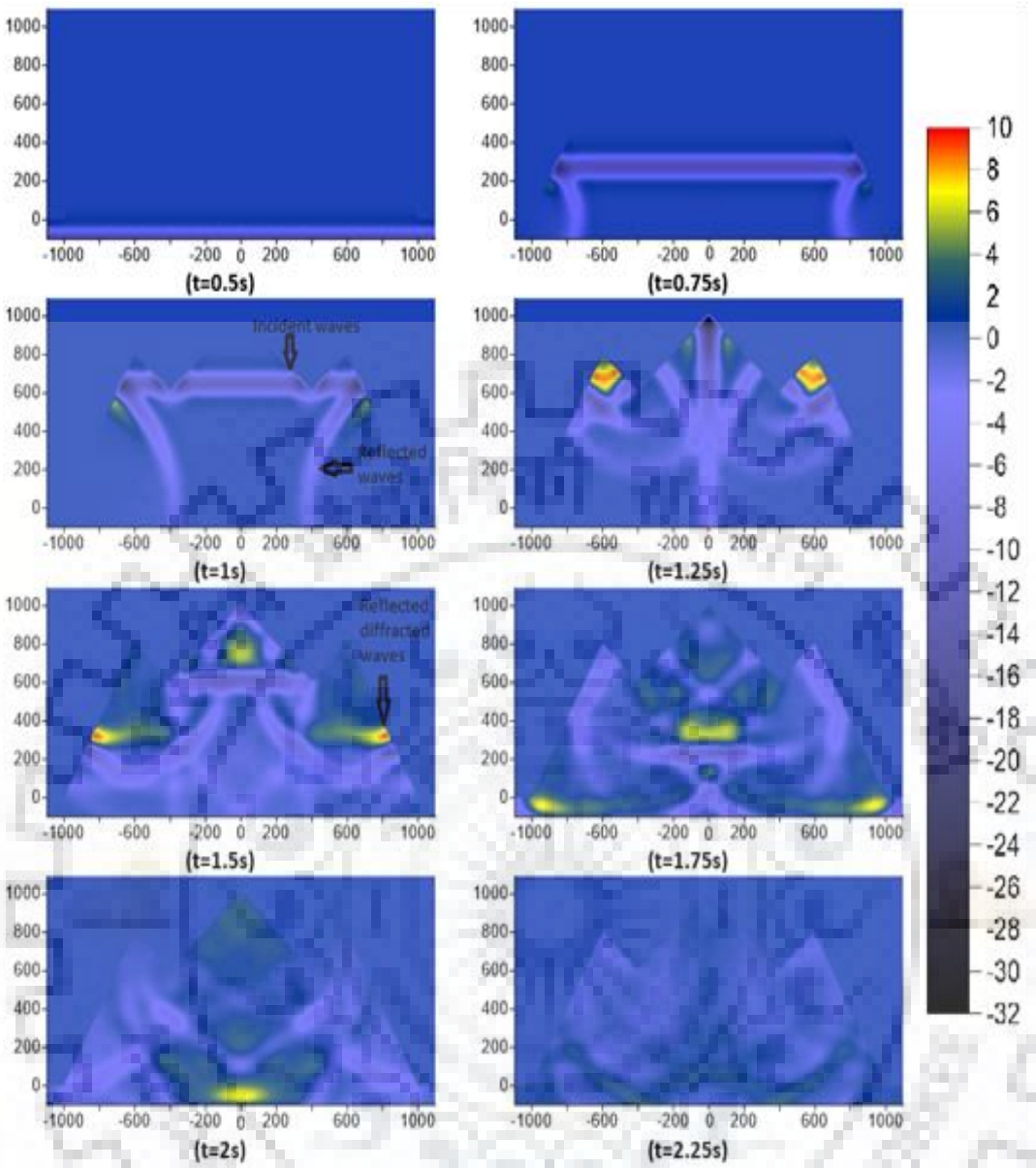

Figure 3.11 Snapshots of SH-wave front at different moments for TR3 model

(c) Spectral amplification factor

Figure 3.12 shows the spectral amplification factor at different recording points along the TR3 ridge topography model. An analysis of table 3.5 reveals that the obtained SAF numerically shows an increase of differences with the increase of number of ridges in the model. For example, the obtained largest SAF at the top of central ridge is 3.4 as to that obtained analytically (2). Analytical value of amplification factor is found lesser than numerical value at the top of the first ridge also. Further, at the trough of the valley there is amplification of ground motion as compared to the de-amplification obtained

analytically (0.69). However, ASA at the trough of the valley depicts a de-amplification of ground motion. The obtained ASA is largest at the crest of the first ridge. Amplification factor for mid-ridge is lesser than that of adjacent ridge even though it has more height because apex angle is more for mid-ridge. It reveals apex angle or shape ratio is major factor for governing amplification factor. Amplification can be found greater at low height ridges with less apex angle than more height ridges with more apex angle. Amplification factor for a ridge is affected by its own shape features as well as features of surrounding neighbouring ridges. Diffraction and refraction of waves occur and may be the reason of some unusual behaviour in the case of multi-ridges.

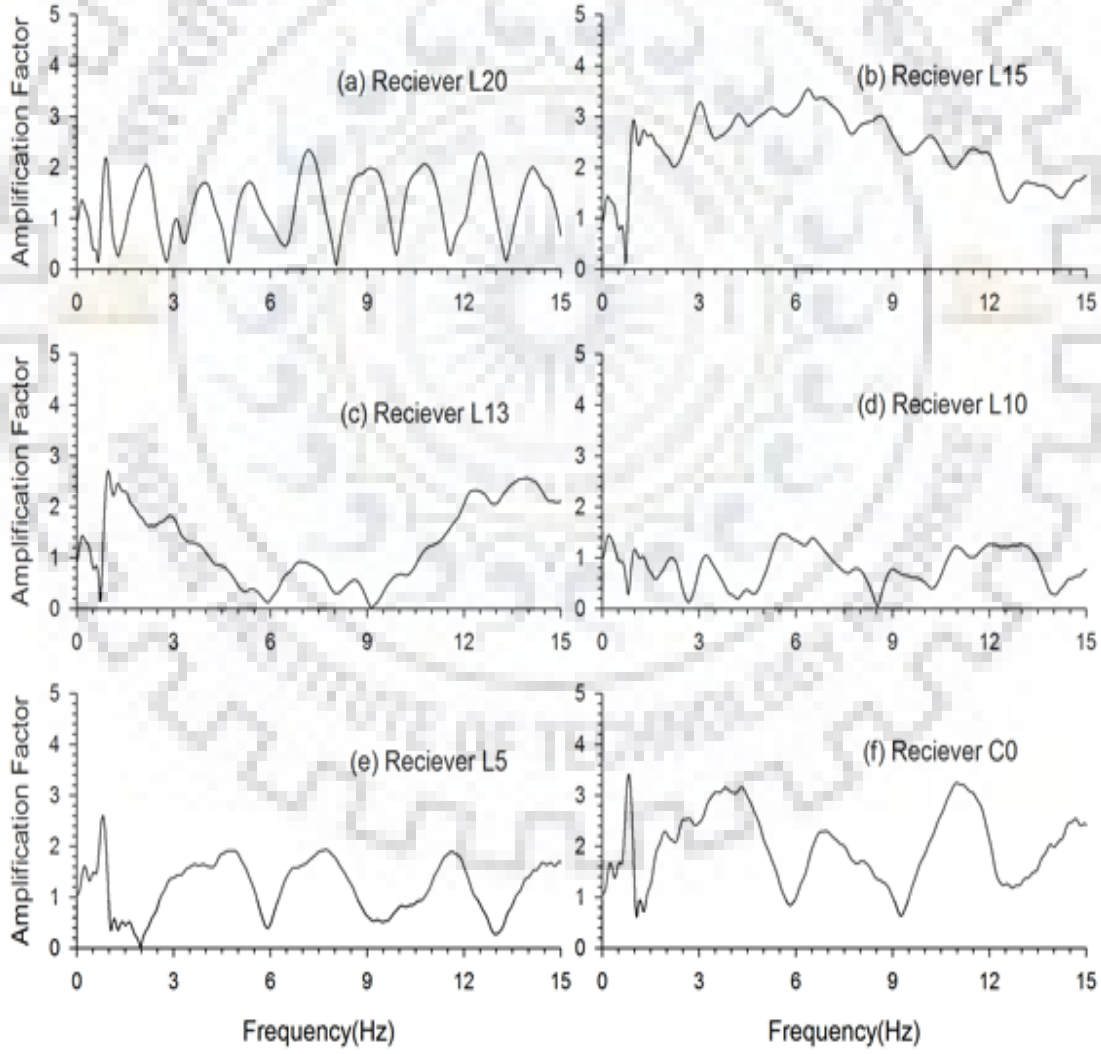

Figure 3.12 Amplification factor at various locations for TR3 model

Table 3.5 A comparison of spectral amplification factor (SAF), average spectral amplification (ASA) at different receiver points with the analytical one

Receiver points	L20(F)	L15(C)	L13(F)	L10(T)	L5(F)	C01(C)
Largest SAF: numerical	2.3	3.5	2.6	1.46	2.6	3.4
Average SAF: numerical	1.25	2.4	1.27	0.82	1.2	2
SAF: analytical	---	2.51	---	0.69	---	2

The spectral amplification at the top of ridges wrt the record at the base, as shown in figure 3.13, depicts that the obtained largest SAF is 54.5 at frequency 9.45 Hz at the top of the first small ridge. Similarly, the obtained largest SAF is 23.24 at frequency 7.7 Hz at the top of the central ridge. This is much larger than the same obtained using numerical/analytical one. So, it may be the reason behind the reported very large amplification in the case of amplification computed using the record at the top and base of the ridge.

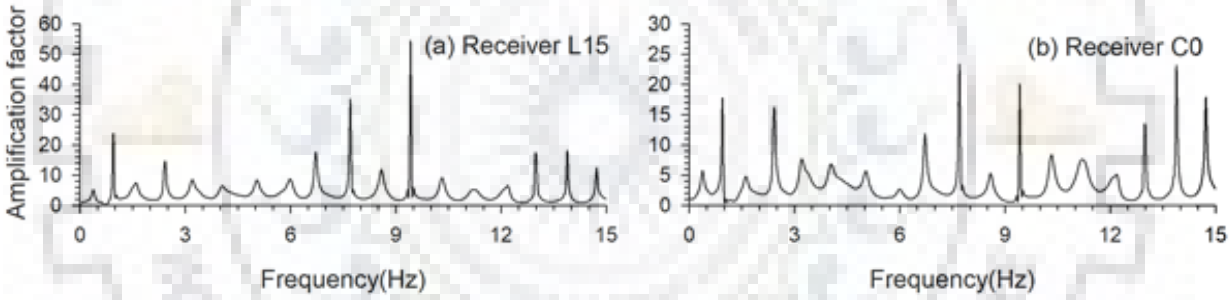

Figure 3.13 Spectral amplification at the top of the ridges wrt the record at the base

3.4.3 SH-wave response of five triangular ridges

A topography model with five triangular ridges is shown in figure 3.14. The SH-wave response of the model is computed at 51 Recorder points, extending from -1000m to 1000 m at an interval of 40 m spacing in the horizontal direction. The height and width of this multi-ridge model 1000m and 2000m, respectively.

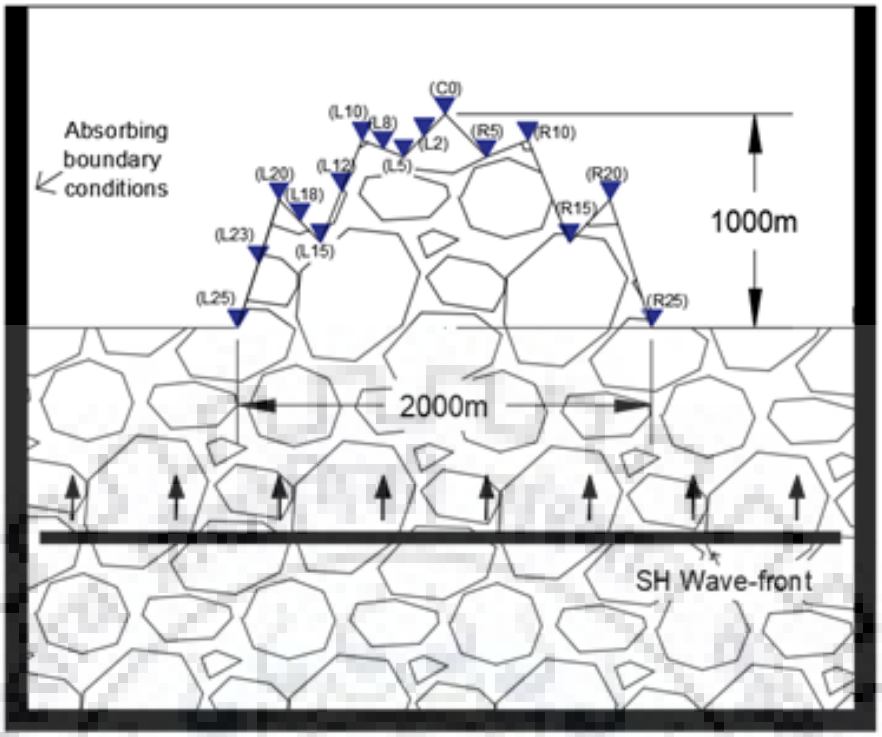

Figure 3.14 Five triangular ridges model (TR5) along with receivers array

(a) Time domain response

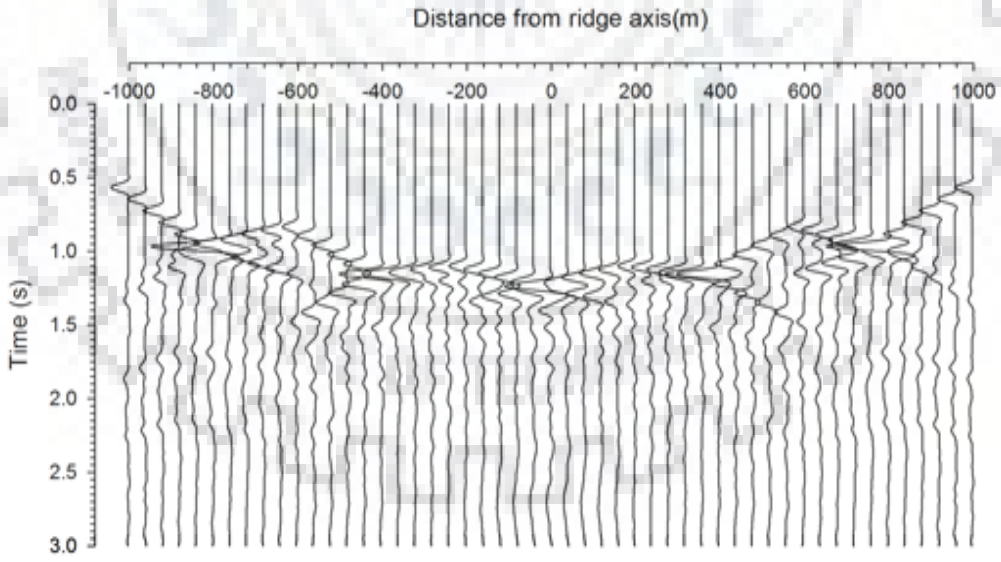

Figure 3.15 SH-wave response of the TR5 ridge topography model

The seismic response of the TR5 model is shown in figure 3.15. The analysis of this figure shows the amplification of SH-wave at the crest of ridges and de-amplification of

the SH-wave at base of the valleys as compared to the amplitude in the case of homogenous half-space model. Figure 3.15 shows that maximum amplitude occurs at the crest of ridge and minimum amplitude at the base of the valley due to focusing and de-focusing of the SH-waves, respectively. The incident SH-wave and the diffracted waves from the base-corners of the ridges/top corners of the valley are very clearly visible. An increase of duration of ground motion in the case of complex ridge topography as compared to the solo-topography model can be inferred.

(b) Spectral amplification factor

Figure 3.16 shows the spectral amplification factor at different recording points along the top of the TR5 ridge topography model. An analysis of table 3.6 reveals that the obtained SAF numerically reveals an increase of differences with the increase of number of ridges in the model. For example, the obtained largest SAF at the top of central ridge is 3.7 as to that obtained analytically (2).Analytical value of amplification factor is found lesser than numerical value at the top of the first and second ridges also. Further, at the trough of the valley there is amplification of ground motion as compared to the de-amplification obtained analytically (0.62 & 0.73, at the trough of first and second valley).However, ASA at the trough of the valley depicts a de-amplification of ground motion.

The obtained ASA is largest at the crest of the first ridge. Amplification factor for mid-ridge is lesser than that of adjacent ridge even though it has more height because apex angle is more for mid-ridge .It reveals apex angle or shape ratio is major factor for governing amplification factor. Amplification can be found greater at low height ridges with less apex angle than more height ridges with more apex angle. Amplification factor for a ridge is affected by its own shape features as well as features of surrounding neighbouring ridges. Diffraction and refraction of waves occur and may be the reason of some unusual behavior in the case of multi-ridges.

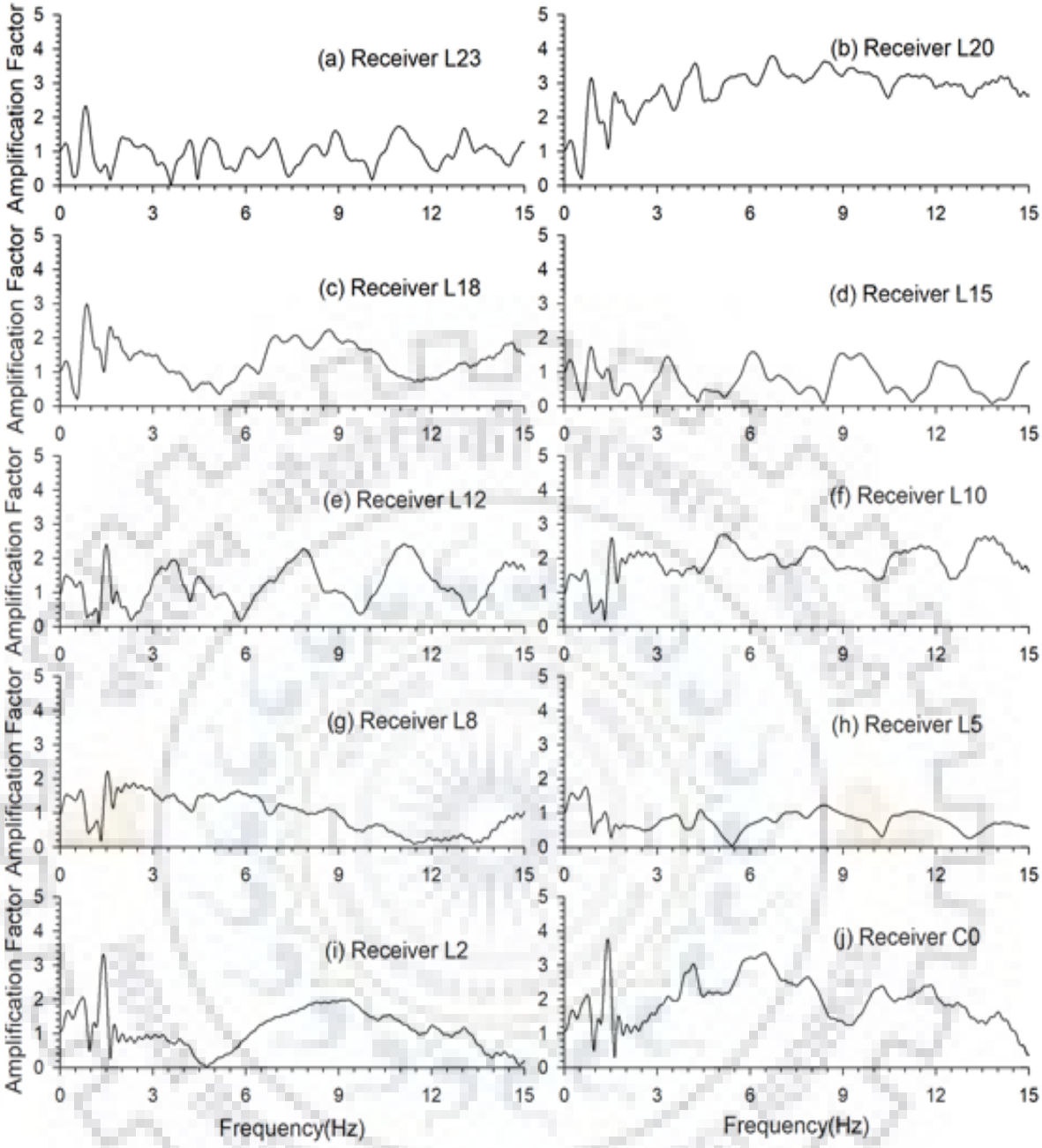

Figure 3.16 Spectral amplification factor at various locations for TR5 model

Table 3.6 A comparison of spectral amplification factor (SAF), average spectral amplification at different receiver points with the analytical one

Receivers	L23(f)	L20(c)	L18(f)	L15(t)	L12(f)	L10(c)	L8(f)	L5(t)	L2(f)	C0(c)
Largest SAF-Num	2.3	3.8	3	1.7	2.4	2.7	2.2	1.7	3.3	3.7
Average SAF-Num	0.95	2.83	1.34	0.75	1.22	1.9	.975	.77	1.17	1.95
SAF-Analytical	---	2.83	---	0.62	---	2	---	0.73	---	2

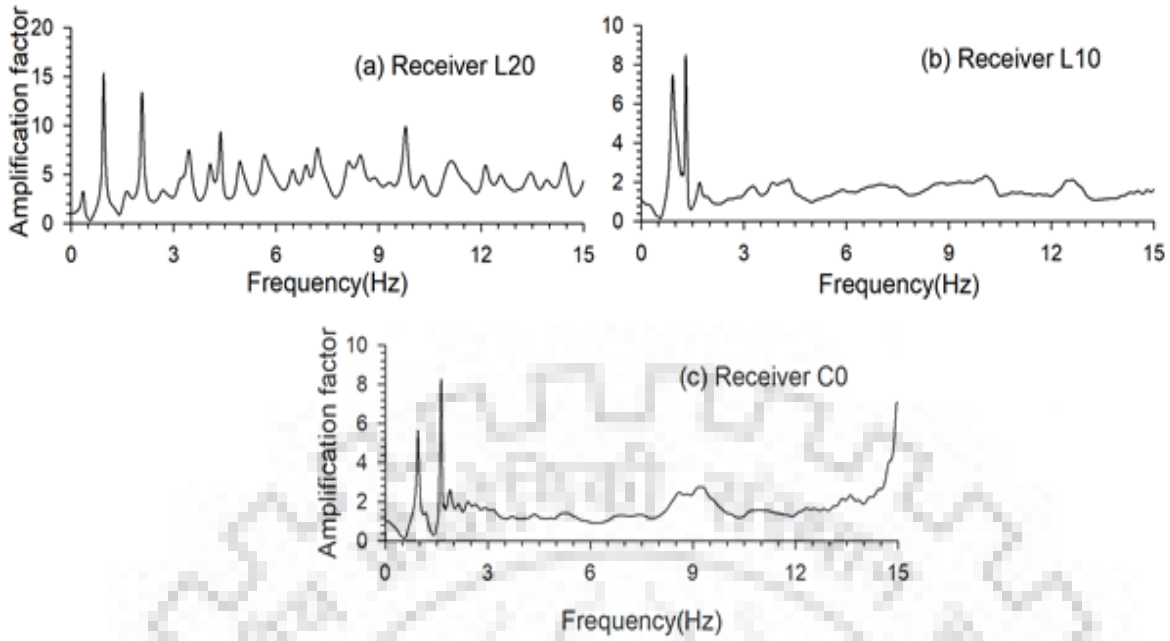

Figure 3.17 Spectral amplification at the top of the ridges wrt the record at the base

The spectral amplification at the top of ridges wrt the record at the base, as shown in figure 3.17, depicts that the obtained largest SAF is 15.27 at frequency 1Hz, 8.5 at frequency 1.34 Hz at the top of the first and second small ridge respectively. Similarly, the obtained largest SAF is 8.25 at frequency 1.68 Hz at the top of the central ridge. This is much larger than the same obtained using numerical/analytical one. So, it may be the reason behind the reported very large amplification in the case of amplification computed using the record at the top and base of the ridge.

3.4.4 SH-wave response of seven triangular ridges

A topography model with seven triangular ridges (TR7 model) is shown in figure 3.18. The SH-wave response of the model is computed at 51 Recorder points, extending from -1000m to 1000 m at an interval of 40 m spacing in the horizontal direction. We have considered total height and width of multi-ridges 1000m and 2000m respectively.

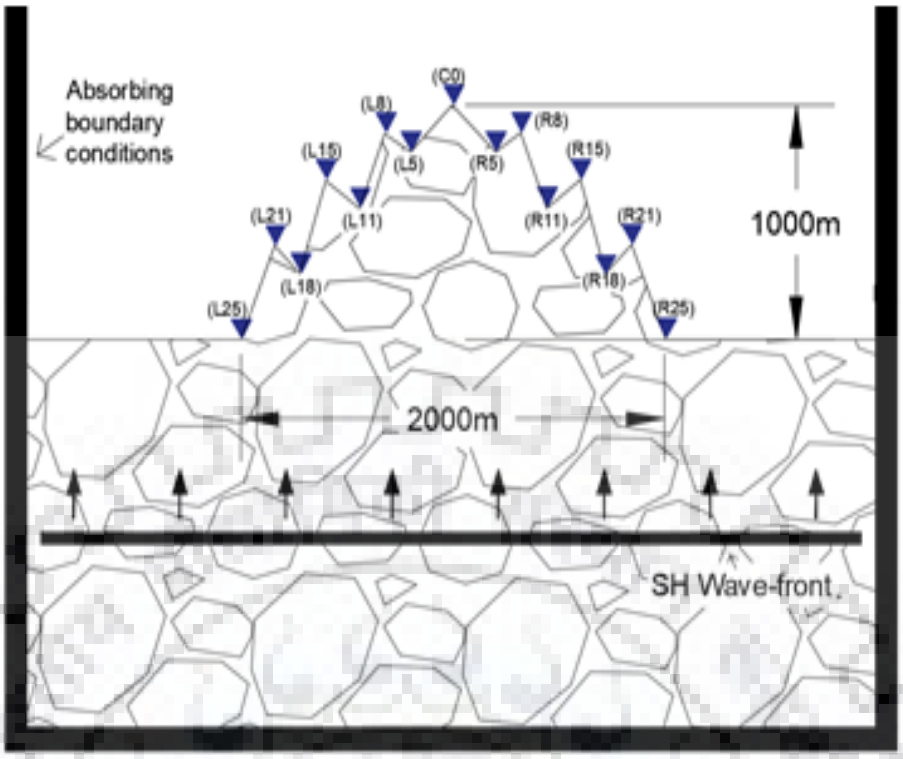

Figure 3.18 TR7 topography model with seven triangular ridges

(a) Time domain response

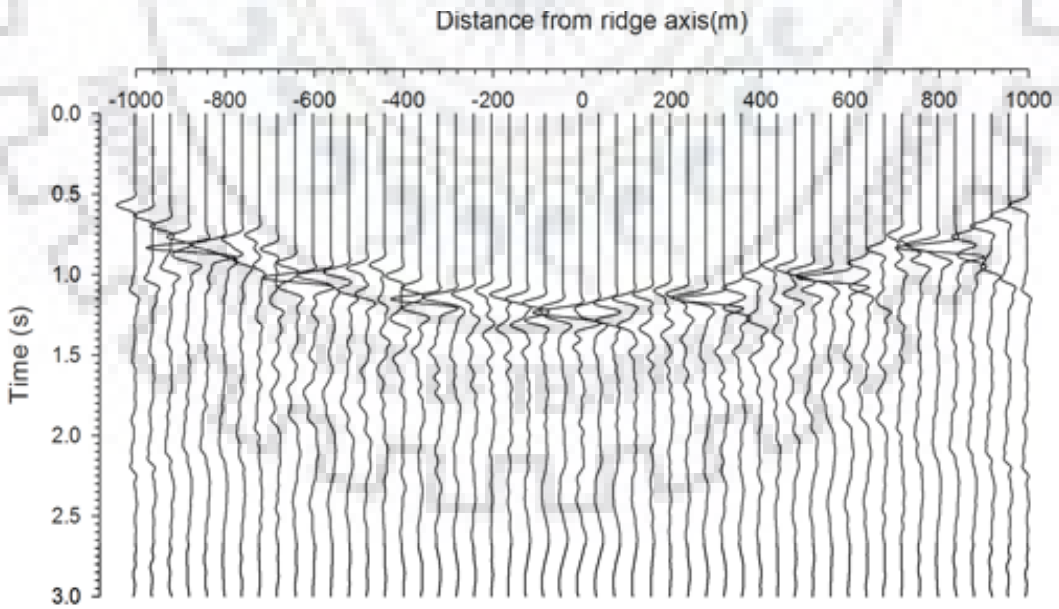

Figure 3.19 SH-wave response of the TR7 ridge topography model

The SH-wave response of the TR7 model is shown in figure 3.19. The analysis of this figure shows the amplification of SH-wave at the crest of ridges and de-amplification of the SH-wave at base of the valleys as compared to the amplitude in the case of homogenous half-space model. Figure 3.19 shows that maximum amplitude occurs at the crest of ridgesand minimum amplitude at the base of the valleys due to focusing and de-focusing of the SH-waves, respectively. The incident SH-wave and the diffracted waves from the base-corners of the ridges/top corners of the valley are very clearly visible. An increase of duration of ground motion in the case of complex ridge topography as compared to the solo-topography model can be inferred.

(b) Spectral amplification factor

Figure 3.20 shows the spectral amplification factors at different recording points along the top of the TR7 ridge topography model. An analysis of table 3.7 reveals that the obtained SAF numerically reveals an increase of differences with the increase of number of ridges in the model. For example, the obtained largest SAF at the top of central ridge is 4 as to that obtained analytically (2).Analytical value of amplification factor is found lesser than numerical value at the top of the first, second and third ridges also. Further, at the trough of the valley there is amplification of ground motion as compared to the de-amplification obtained analytically (0.58, 0.63 & 0.70, at the trough of first, second and third valley).However, ASA at the trough of the valleys depicts a de-amplification of ground motion.

The obtained ASA is largest at the crest of the first ridge.Amplification factor for mid-ridge is comparable than that of other ridges even though it has more height because apex angle is more for mid-ridge.It reveals apex angle or shape ratio is major factor for governing amplification factor. Amplification factor for a ridge is affected by its own shape features as well as features of surrounding neighboring ridges. Diffraction and refraction of waves occur and may be the reason of some unusual behavior in the case of multi-ridges.

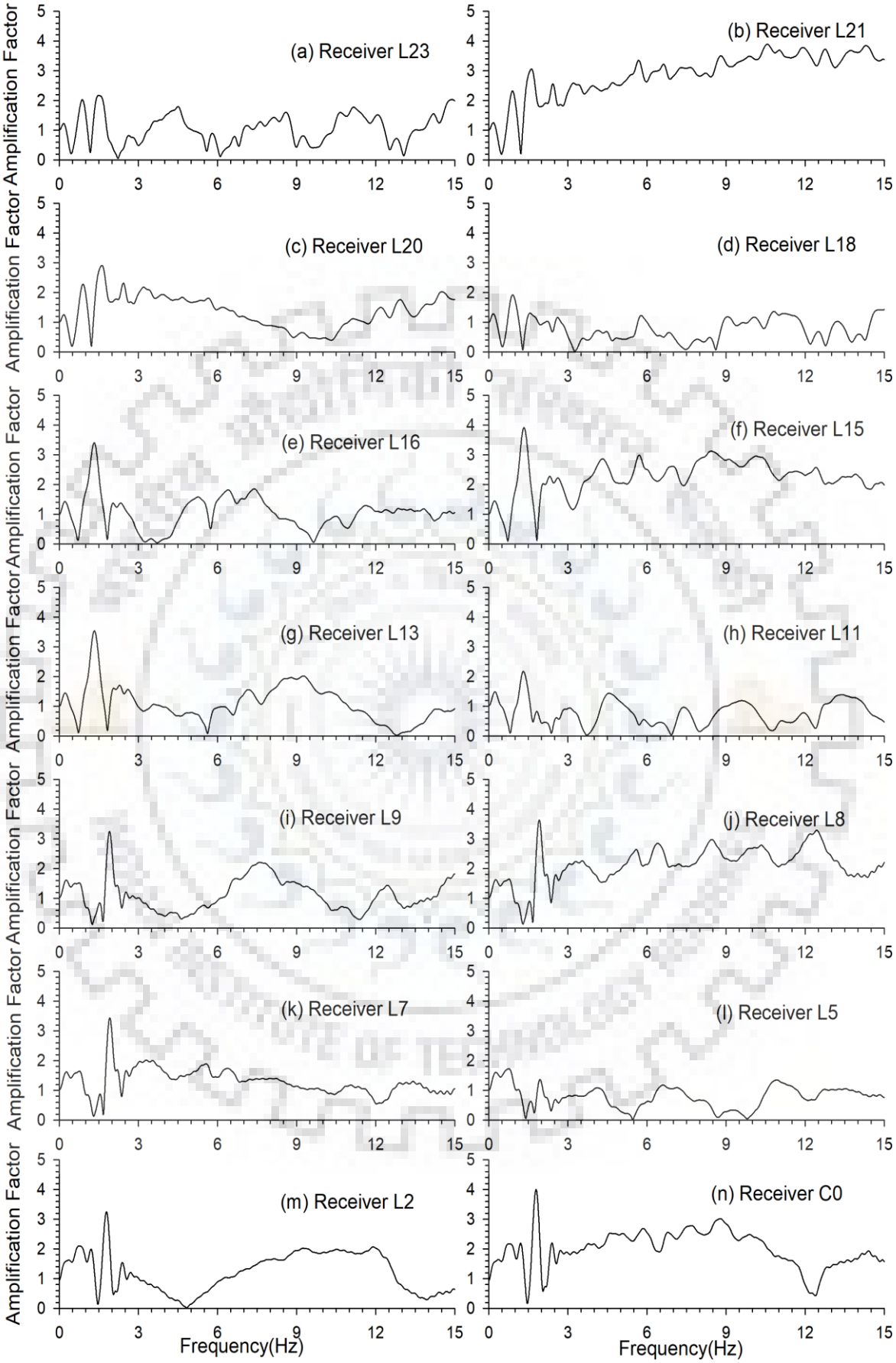

Figure 3.20 Spectral amplification factors at various locations for the TR7 model

Table 3.7 A comparison of spectral amplification factor (SAF), average spectral amplification at different receiver points with the analytical one

Receivers	L23 (f)	L21 (c)	L20 (f)	L18 (t)	L16 (f)	L15 (c)	L13 (f)	L11 (t)	L9 (f)	L8 (c)	L7 (f)	L5 (t)	L2 (f)	C0 (c)
Largest SAF:Num	2.18	3.88	2.9	1.9	3.36	3.9	3.5	2.15	3.25	3.6	3.43	1.75	3.3	4
Average SAF:Num	1.05	2.86	1.38	0.77	1.04	2.25	1.07	0.77	1.09	2.12	1.3	0.79	1.2	2
SAF:Anal	---	2.7	---	0.58	---	2.58	---	0.63	---	2.33	---	0.7	---	2

However, finally it may be concluded that the % increase of amplification at the top of central ridges is largest as compared to the other ridges. For example, it is 100% at the top of central ridge and 43.7% at the top of the first ridge.

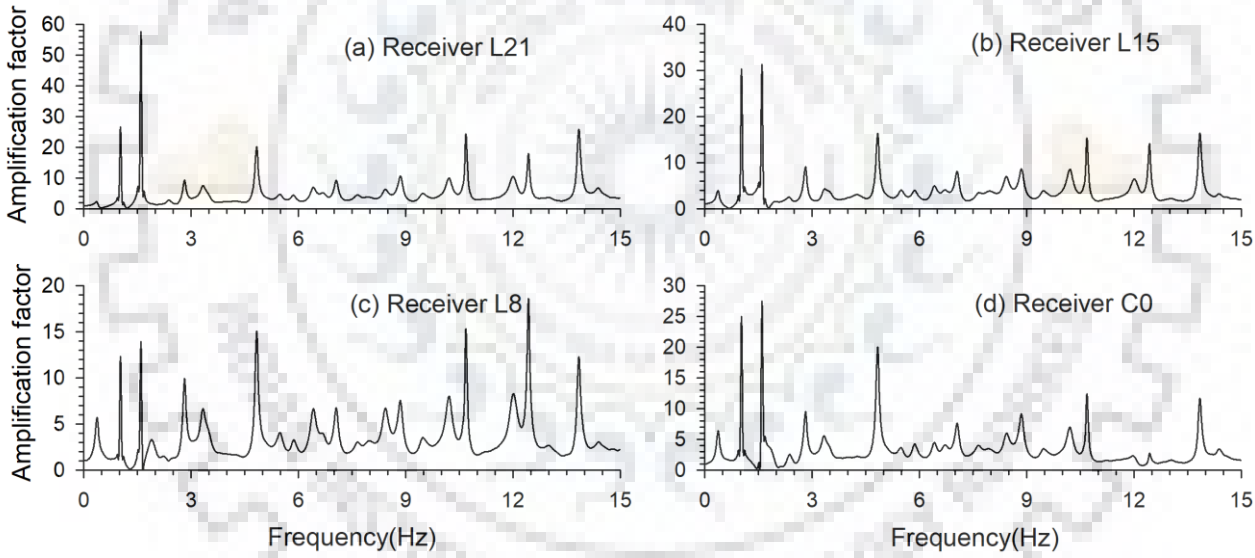

Figure 3.21 Spectral amplification at the top of the ridges wrt the record at the base

The spectral amplification at the top of ridges wrt the record at the base, as shown in figure 3.21, depicts that the obtained largest SAF is 57.5 at frequency 1.6 Hz,31.3 at frequency 1.6 Hz,18.4 at frequency 12.5 Hz at the top of the first ,second, third small ridge respectively. Similarly, the obtained largest SAF is 27.65 at frequency 1.56 Hz at the top of the central ridge. This is much larger than the same obtained using numerical/analytical one. So, it may be the reason behind the reported very large amplification in the case of amplification computed using the record at the top and base of the ridge.

3.5 SH-WAVE RESPONSE OF ELLIPTICAL RIDGES

3.5.1 SH-wave response of single elliptical ridge

A topography model with one elliptical ridge is shown in figure 3.22. The SH-wave response of the model is computed at 51 recording points, extending from -1000m to 1000 m at an interval of 40 m spacing in the horizontal direction. The height and width of this ridge model 1000 m and 2000 m, respectively.

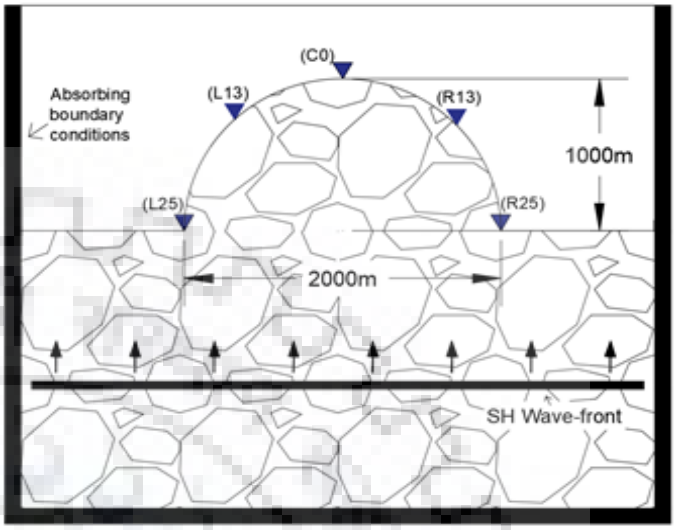

Figure 3.22 Single elliptical ridge model (ER1) along with receivers array

(a) Time domain response

The SH-wave response of the ER1 model is shown in figure 3.23. The analysis of this figure shows the amplification of SH-wave at the crest of ridge as compared to the amplitude in the case of homogenous half-space model. Apart from the incident SH-wave and the diffracted waves from the base-corners of the ridge, a new seismic phase can be seen in contrast to the response of TR1 model. This extra phase may be the Love wave, but needs verification using the snapshots of the wave-field.

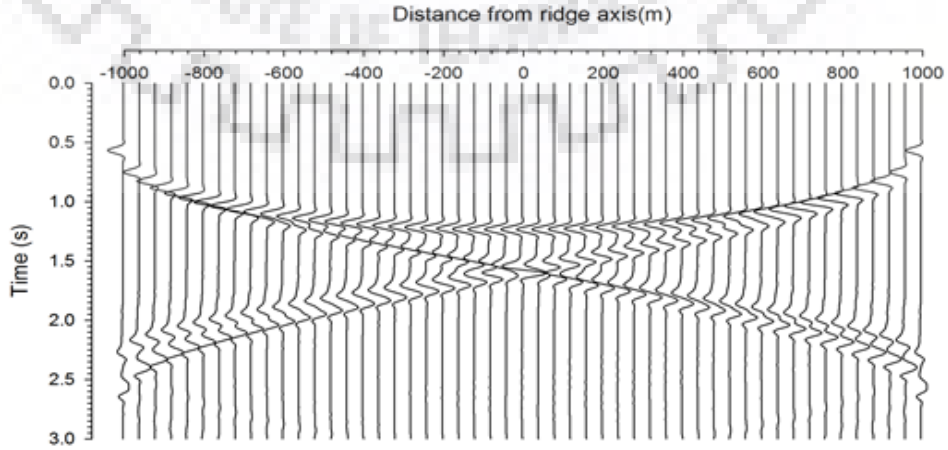

Figure 3.23 SH-wave response of the ER1 ridge topography model

(b) Snapshots of wave-field

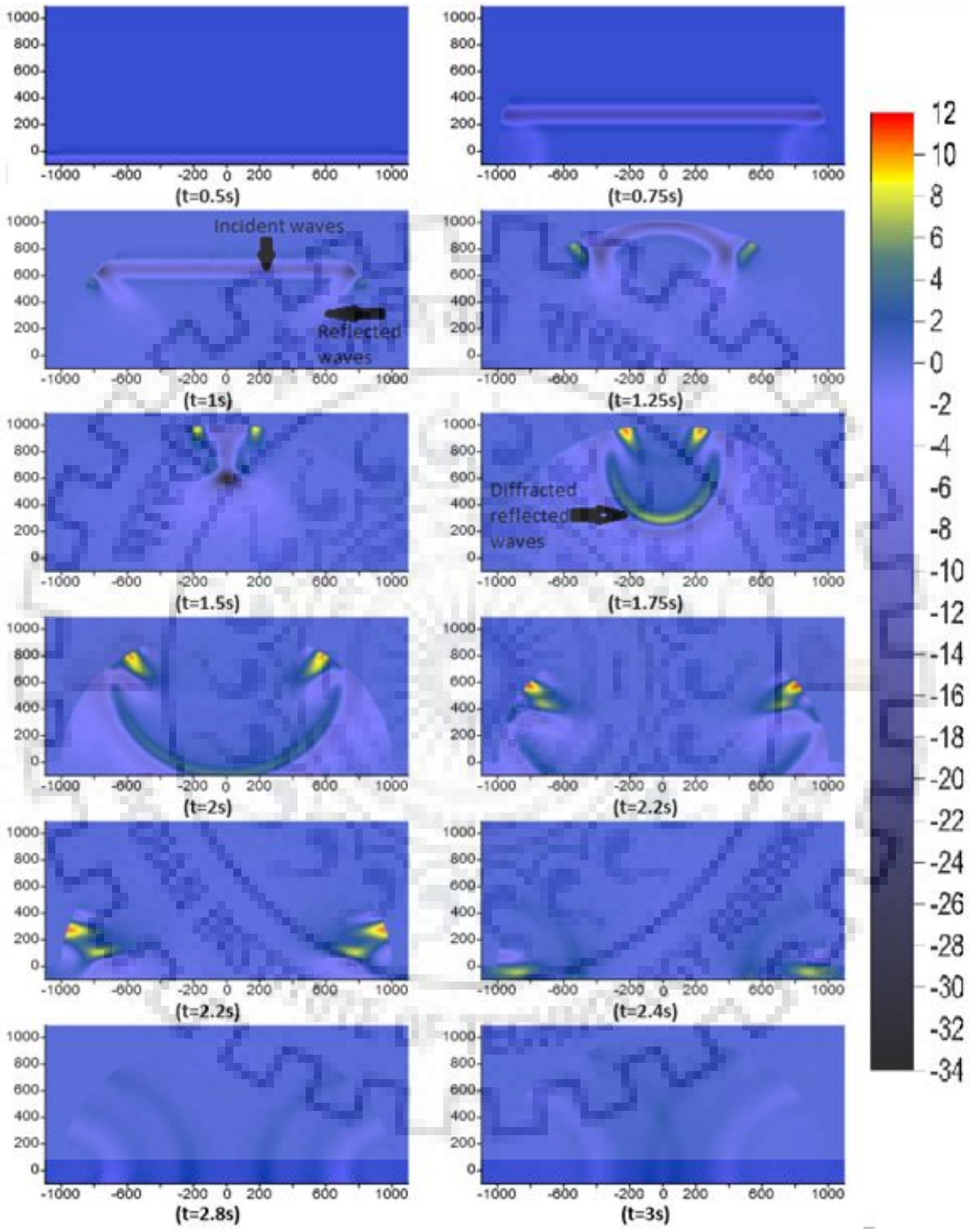

Figure 3.24 Snapshots of SH-wave at different moments for ER1 model

The snapshots have been computed at different moments from 0.5s to 3s and shown in Fig 3.24. The snapshot at time 0.5s shows only the incident wave in the considered area.

The snapshot at times 0.75s and 1.0s show the incident plane wave front, diffracted as well as the reflected waves from the flanks of the elliptical ridge. The snapshot at time 1.25s clearly illustrates that the generated Love wave and propagating towards the crest of the ridge along with the reflected diffracted waves. Further, the propagation of the Love waves along the elliptical ridge can be tracked in the successive snapshots.

(c) Spectral amplification factor

Figure 3.25a&b shows the spectralamplification factor of ER1 at L13 and C0 recording point, respectively. An analysis of table 3.8 reveals that the obtained SAF numerically is 2.55 which is larger than that obtained in case of the corresponding triangular ridge.

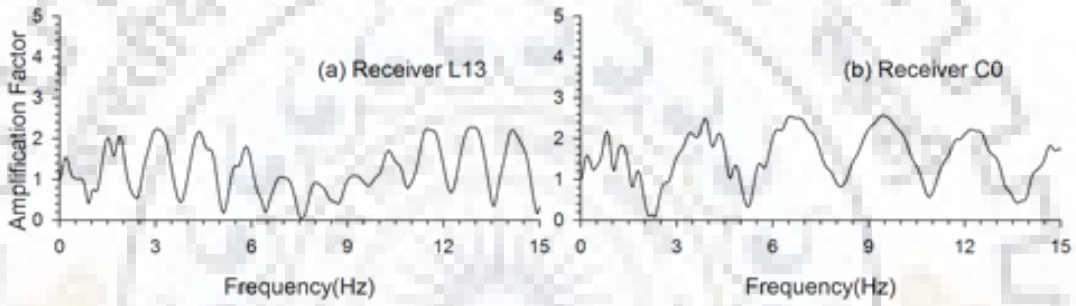

Figure 3.25 Spectral amplification factors at two locations for ER1 model

Table 3.8 A comparison of spectral amplification factor (SAF) and average spectral amplification (ASA) at different receiver points.

Receiver	L13(flank)	C0(crest)
Largest SAF: numerical	2.28	2.55
Average SAF: numerical	1.21	1.54

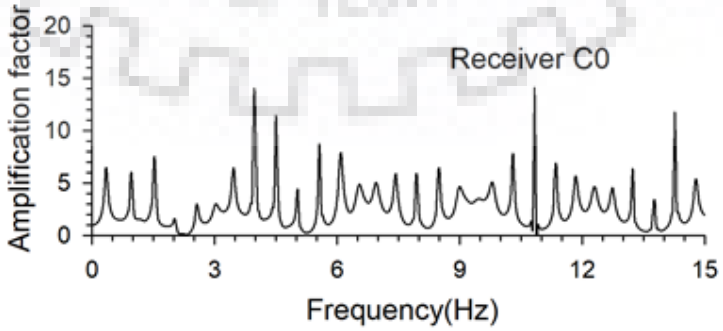

Figure 3.26 The spectral amplifications at the top of the elliptical ridge wrt the record at the base

The spectral amplification at the top of elliptical ridge wrt the record at the base, as shown in figure 3.26, depicts that the largest SAF is 14.13 at frequency 4.02 Hz. This is much larger than the same obtained using numerical one. So, it may be the reason behind the reported very large amplification in the case of amplification computed using the record at the top and base of the ridge.

3.5.2 SH-wave response of three elliptical ridges

A topography model with three elliptical ridge ER3 is shown in figure 3.27. The SH-wave response of the model is computed at 51 recording points, extending from -1000m to 1000 m at an interval of 40 m spacing in the horizontal direction.

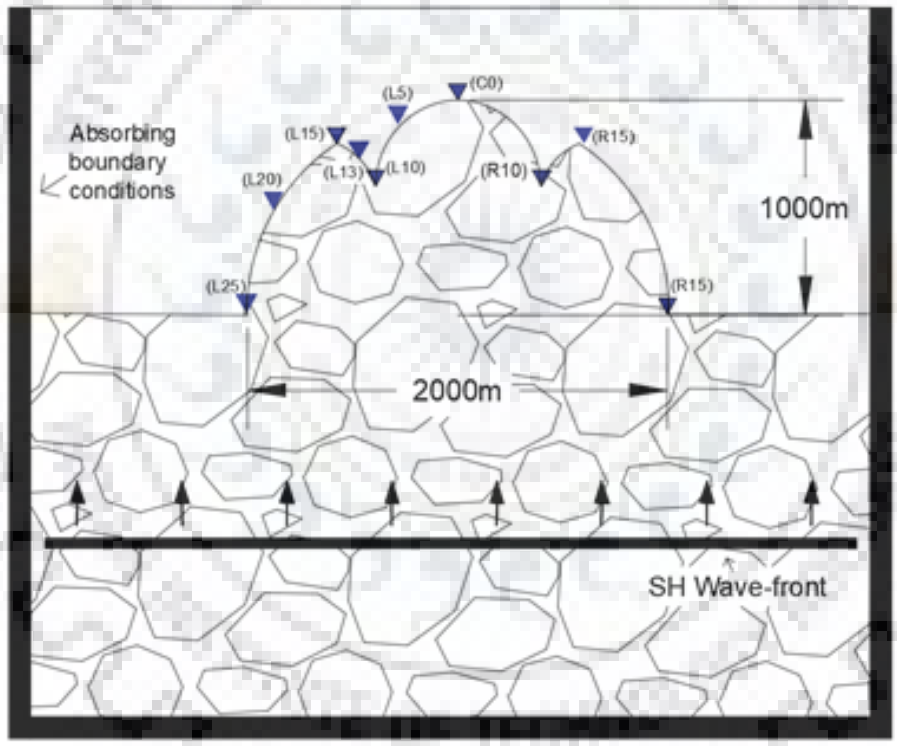

Figure 3.27 Three elliptical ridges model (ER3) along with receivers array

(a) Time domain response

The SH-wave response of the ER3 model is shown in figure 3.28. The analysis of this figure shows the amplification of SH-wave at the crest of elliptical ridge and de-amplification at the trough of the elliptical valley as compared to the amplitude in the case of homogenous half-space model. A drastic increase of duration of ground motion due to increase of complexity can be inferred.

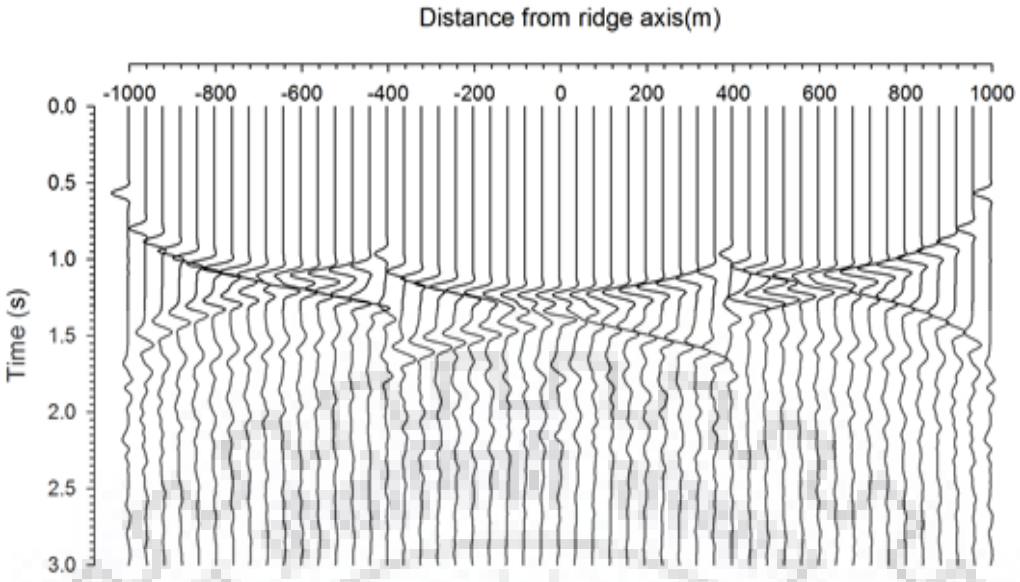

Figure 3.28 SH-wave response of the ER3 Model

(b) Snapshots of wave-field

The snapshots have been computed at different moments from 0.5s to 2.25s and shown in Fig 3.29. The snapshot at time 0.5s shows only the incident wave in the considered area. The snapshot at times 0.75s and 1.0s show the incident plane wave front, diffracted as well as the reflected waves from the flanks of the elliptical ridge. The snapshot at time 1.25s clearly illustrates that the generated Love wave and propagating towards the crest of the central ridge along with the reflected diffracted waves.

It can be seen from snapshots that as wave-front moves upwards, it is reflected by ridge topography and it reaches the crests of ridges around at 1.25s to 1.5s hence maximum amplitude is shown there at that time.

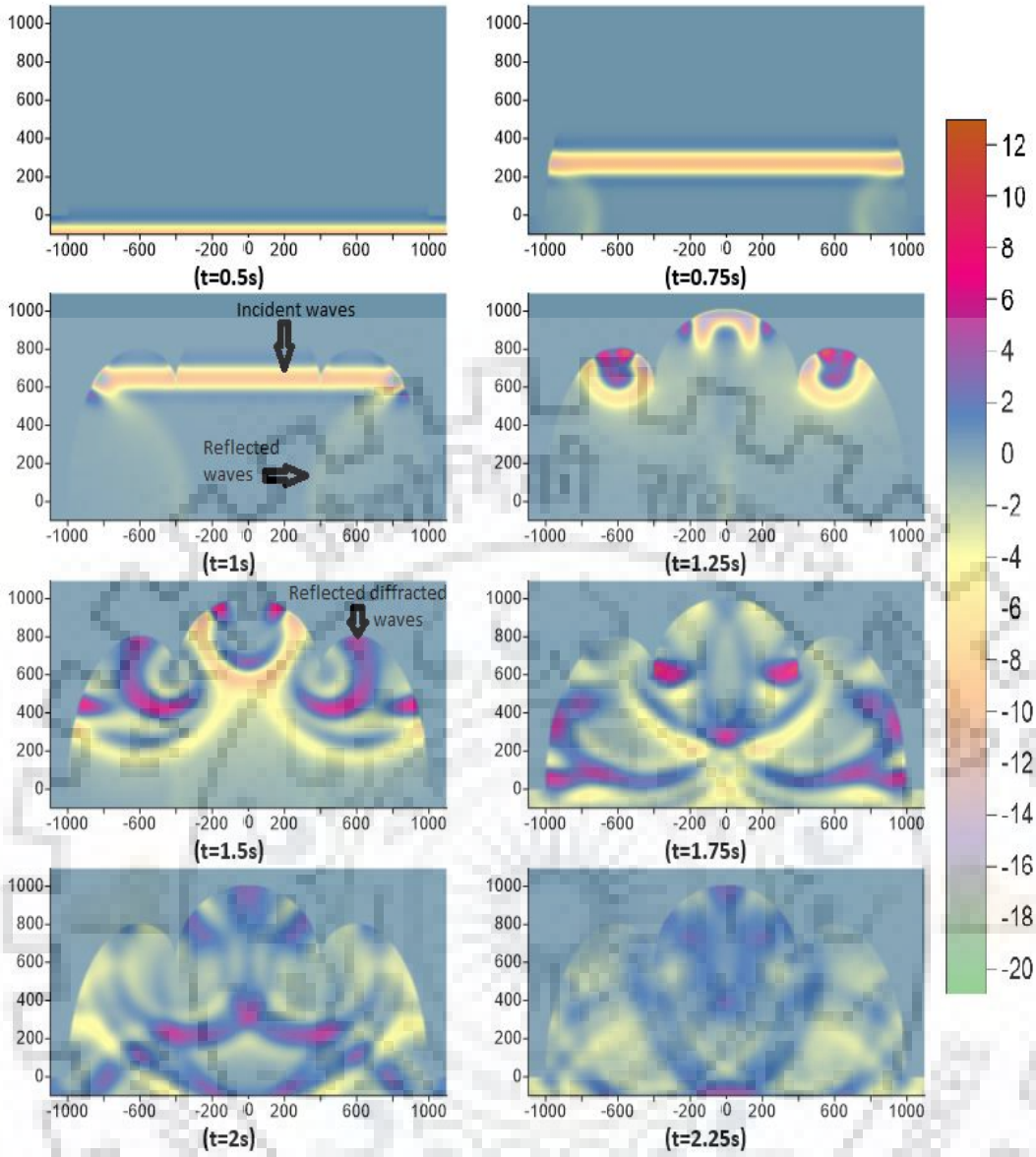

Figure 3.29 Snapshots of SH-wave front at different moments for ER3 model

(c) Spectral amplification factor

Figure 3.30 shows the spectral amplification factors at different recording points along the top of the ER3 ridge topography model. An analysis of table 3.9 reveals that the obtained SAF numerically reveals an increase of differences with the increase of number of ridges in the model. For example, the obtained largest SAF at the top of central ridge is 2.8. Further, at the trough of the valley there is amplification of ground motion as compared to the expected de-amplification. However, ASA at the trough of the valleys depicts a de-amplification of ground motion. The obtained ASA is largest at

the crest of the first ridge. Amplification factor for mid-ridge is comparable than that of other ridges even though it has more height because apex angle is more for mid-ridge.It reveals apex angle or shape ratio is major factor for governing amplification factor.

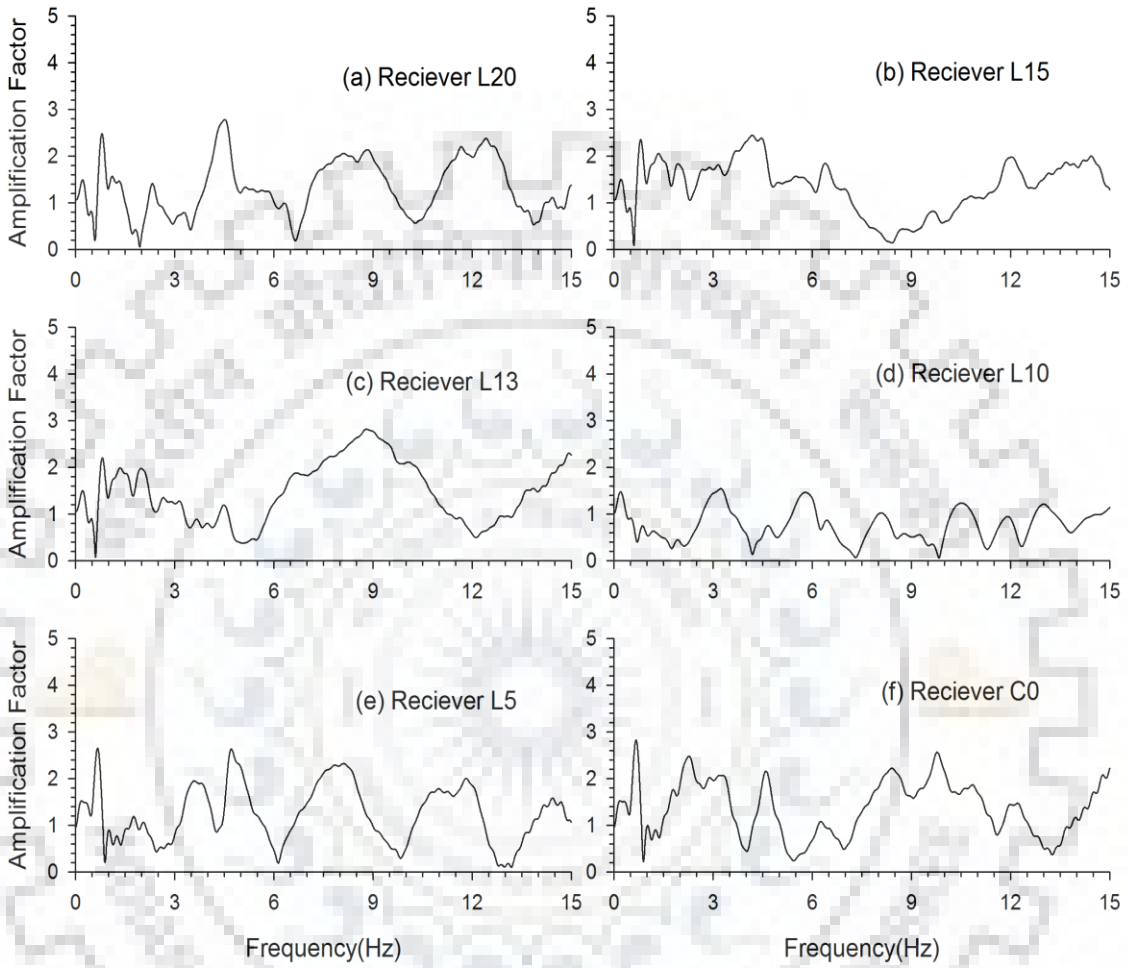

Figure 3.30 Spectral amplification factors at various locations for ER3 model

Table 3.9 A comparison of spectral amplification factor (SAF) and average spectral amplification (ASA) at different receiver points

Receiver	L20(flank)	L15(crest)	L13(flank)	L10(trough)	L5(flank)	C01(crest)
Largest SAF	2.75	2.45	2.8	1.53	2.6	2.8
Average SAF	1.32	1.36	1.4	0.76	1.24	1.37

The spectral amplification at the top of elliptical ridge wrt the record at the base, as shown in figure 3.31, depicts that the obtained largest SAF is 42.16 at frequency 13.78 Hz at the top of the first small ridge. Similarly, the obtained largest SAF is 22 at frequency 13.8 Hz at the top of the central ridge. This is much larger than the same obtained using numerical one. So, it may be the reason behind the reported very large amplification in the case of amplification computed using the record at the top and base of the ridge.

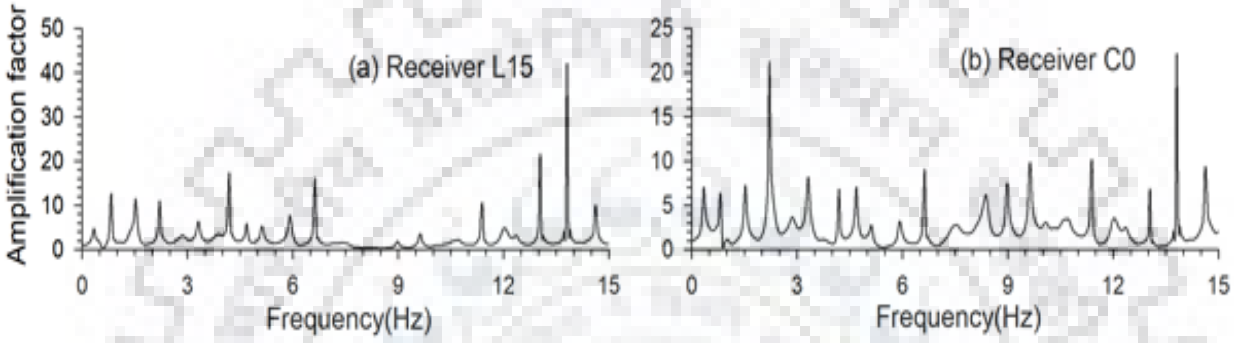

Figure 3.31 The spectral amplifications at the top of the elliptical ridge wrt the record at the base

3.5.3 SH-wave response of five elliptical ridges

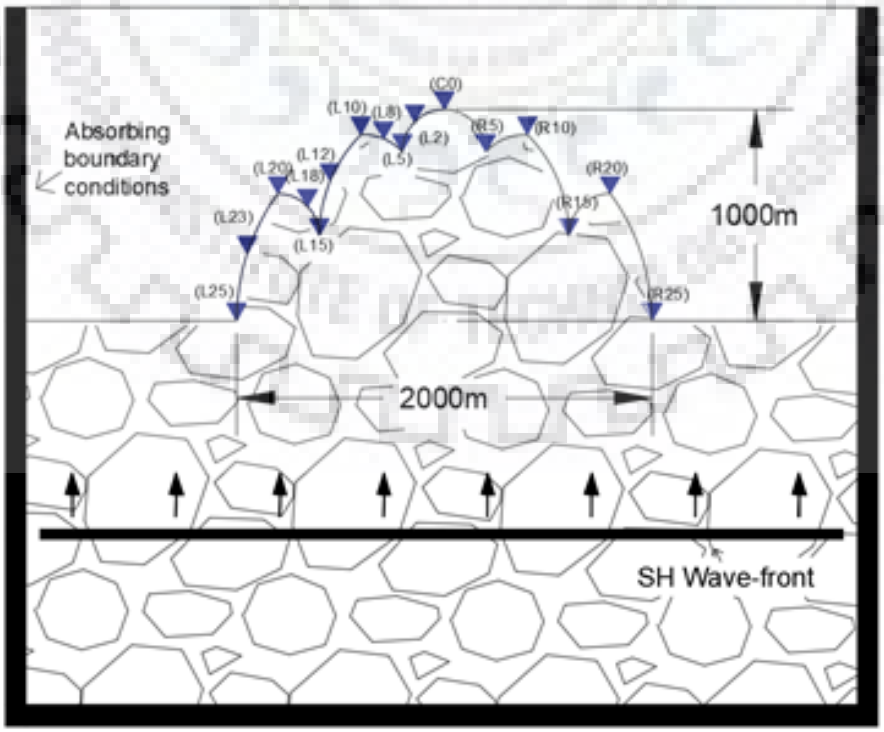

Figure 3.32 Five elliptical ridges model (ER5) along with receivers array

A topography model with five elliptical ridges ER5 is shown in figure 3.32. The SH-wave response of the model is computed at 51 recording points, extending from -1000m to 1000 m at an interval of 40 m spacing in the horizontal direction.

(a) Time domain response

The SH-wave response of the ER5 model is shown in figure 3.33. The analysis of this figure shows the amplification of SH-wave at the crest of elliptical ridge and de-amplification at the trough of the elliptical valley as compared to the amplitude in the case of homogenous half-space model. A drastic increase of duration of ground motion due to increase of complexity can be inferred.

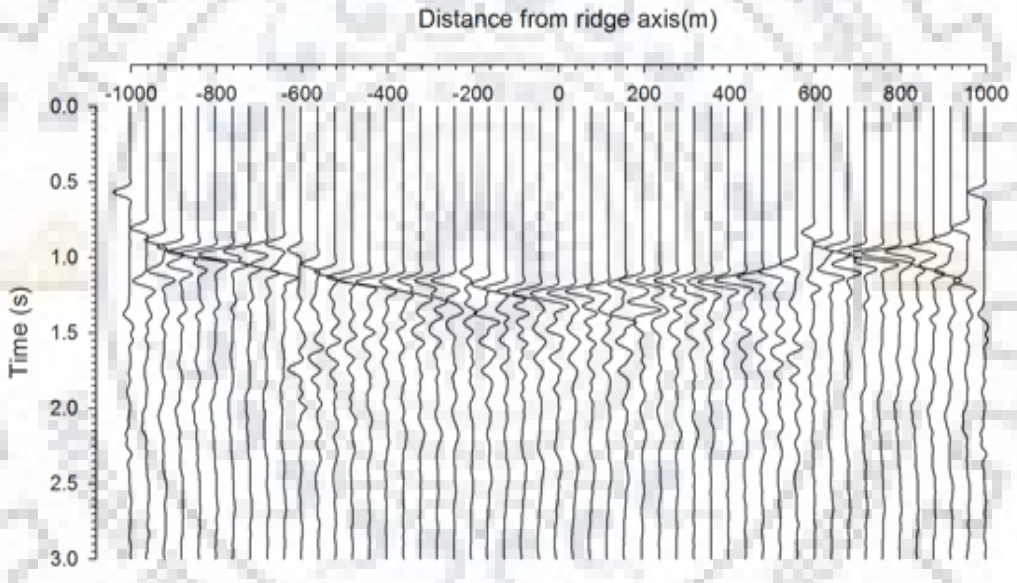

Figure 3.33 Spectral amplitude of ER5 model at various receivers along ridge profile

(c) Spectral amplification factor

Figure 3.34 shows the spectral amplification factors at different recording points along the top of the ER5 ridge topography model. An analysis of table 3.10 reveals that the obtained SAF numerically reveals an increase of differences with the increase of number of ridges in the model. For example, the obtained largest SAF at the top of central ridge is 3. Further, at the trough of the valley there is amplification of ground motion as compared to the expected de-amplification. However, ASA at the trough of

the valleys depicts a de-amplification of ground motion. The obtained ASA is largest at the crest of the first ridge.Average amplification factor for central ridge is less that of first ridge even though it has more height because apex angle is more for mid-ridge.It reveals apex angle or shape ratio is major factor for governing amplification factor.

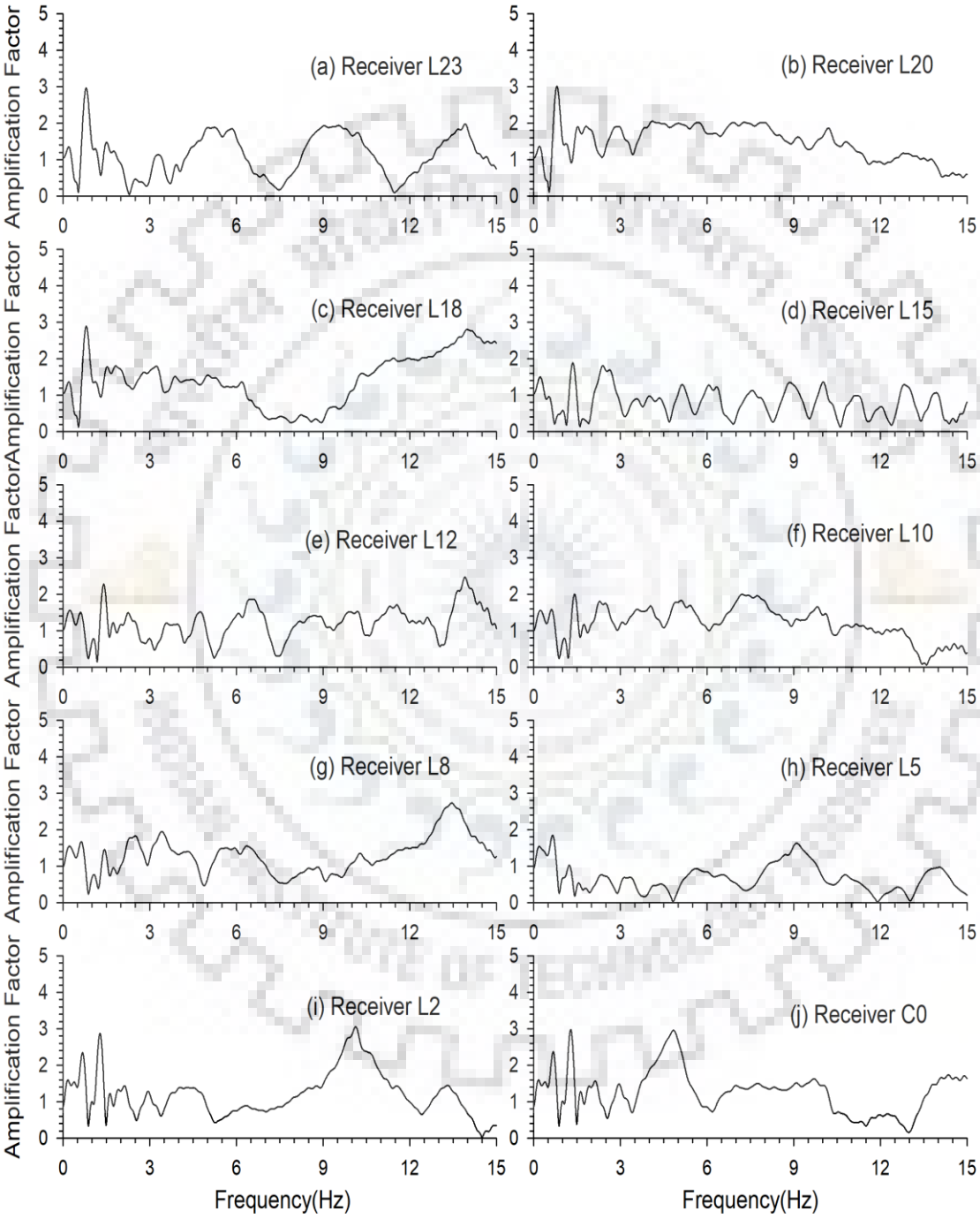

Figure 3.34 Spectral amplitude at various locations for ER5 model

Table 3.10 A comparison of spectral amplification factor (SAF) and average spectral amplification (ASA) at different receiver points

Receivers	L23(f)	L20(c)	L18(f)	L15(t)	L12(f)	L10(c)	L8(f)	L5(t)	L2(f)	C0(c)
Largest SAF	2.93	3	2.8	1.9	2.25	2	2.7	1.86	3	3
Average SAF	1.12	1.47	1.42	0.79	1.2	1.22	1.3	0.67	1.2	1.26

The spectral amplification at the top of ridges wrt the record at the base, as shown in figure 3.35, depicts that the obtained largest SAF is 25.03 at frequency 2.04Hz, 24.3 at frequency 3.3 Hz at the top of the first and second small ridge respectively. Similarly, the obtained largest SAF is 20.2 at frequency 2.04 Hz at the top of the central ridge. This is much larger than the same obtained using numerical/analytical one. So, it may be the reason behind the reported very large amplification in the case of amplification computed using the record at the top and base of the ridge.

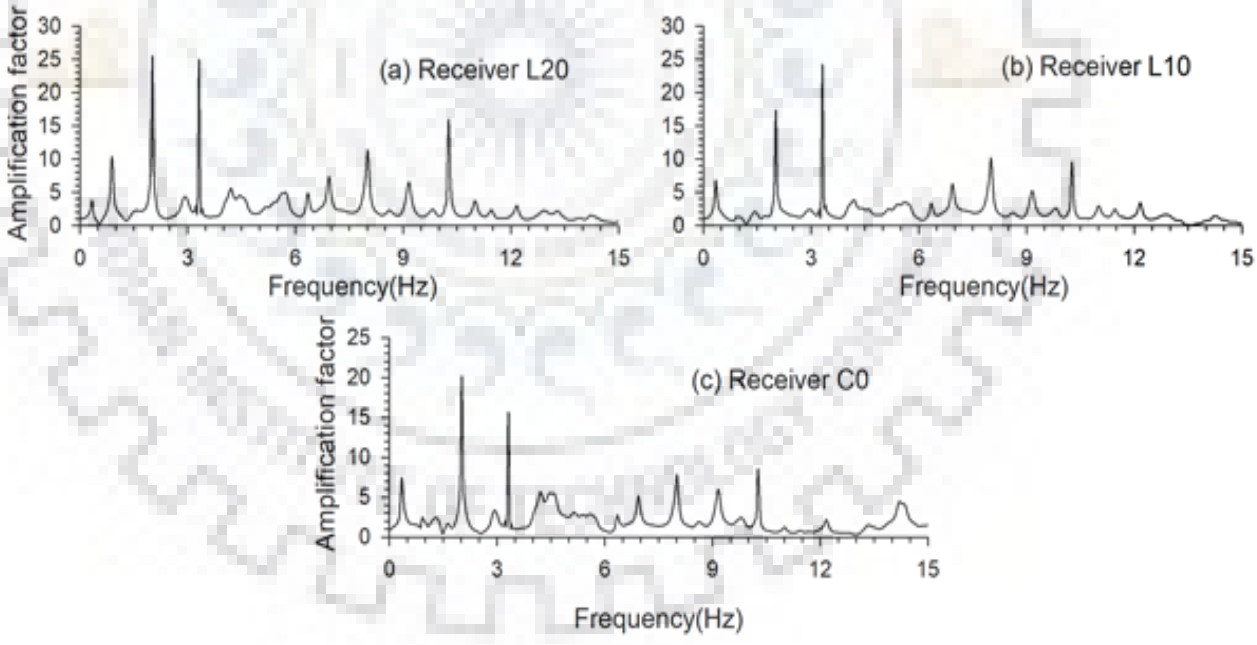

Figure 3.35 Spectral amplification at the top of the ridges wrt the record at the base

3.5.4 SH-wave response of seven elliptical ridges

A topography model with seven elliptical ridges ER7 is shown in figure 3.36. The SH-wave response of the model is computed at 51 recording points, extending from -1000m to 1000 m at an interval of 40 m spacing in the horizontal direction.

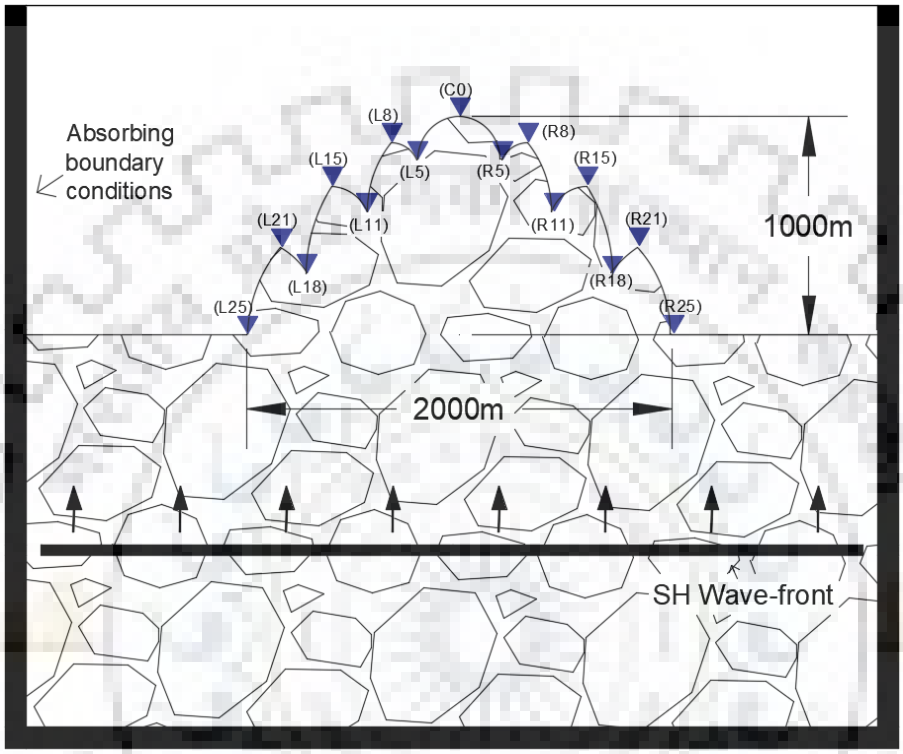

Figure 3.36 Seven elliptical ridges model (ER7) along with receivers array

.

(a) Time domain response

.

The SH-wave response of the ER7 model is shown in figure 3.37. The analysis of this figure shows the amplification of SH-wave at the crest of elliptical ridge and de-amplification at the trough of the elliptical valley as compared to the amplitude in the case of homogenous half-space model. A drastic increase of duration of ground motion due to increase of complexity can be inferred.

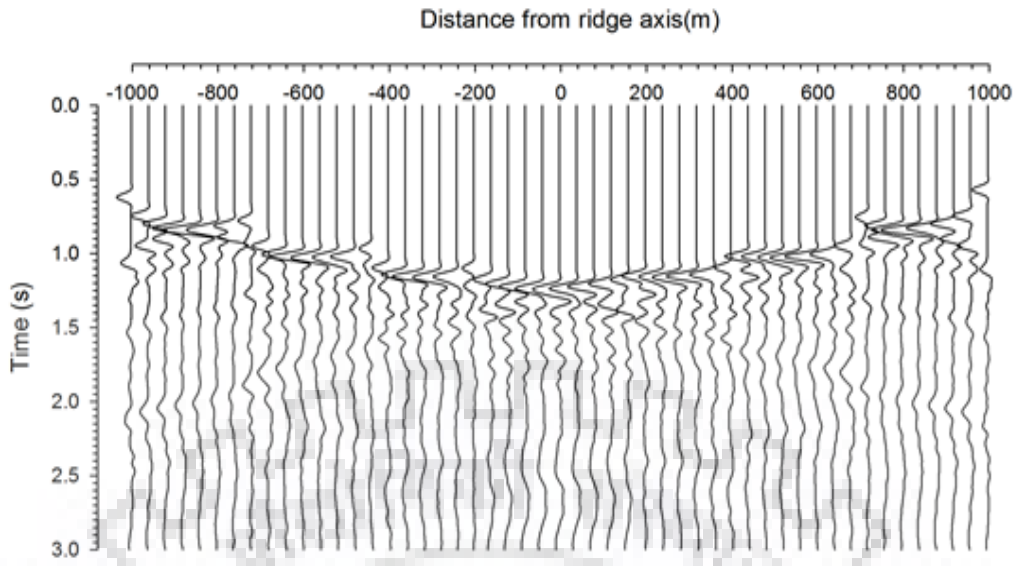

Figure 3.37 Spectral amplitude of ER7 model at various receivers along ridge profile

(d) Spectral amplification factor

Figure 3.38 shows the spectral amplification factors at different recording points along the top of the ER7 ridge topography model. An analysis of table 3.11 reveals that the obtained SAF numerically reveals an increase of differences with the increase of number of ridges in the model. For example, the obtained largest SAF at the top of central ridge is 3.45. Further, at the trough of the valley there is amplification of ground motion as compared to the expected de-amplification. However, ASA at the trough of the valleys depicts a de-amplification of ground motion. The obtained ASA at the crest of the central ridge is not the maximum one.Amplification factor for central ridge is even less that at other ridges even though it has more height because apex angle is more for mid-ridge.It reveals apex angle or shape ratio is major factor for governing amplification factor.

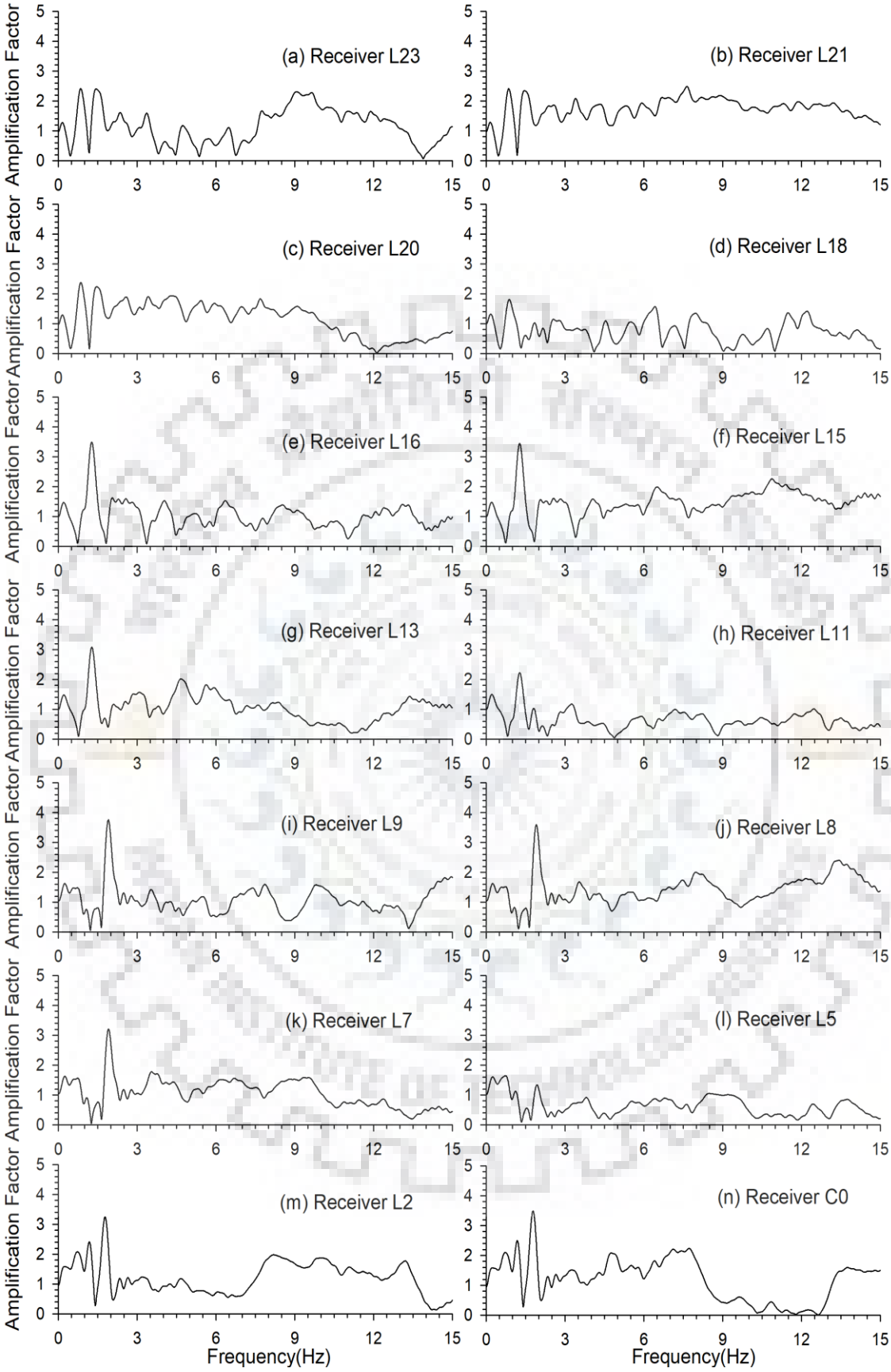

Figure 3.38 Spectral amplification factors at various locations for ER7 model

Table 3.11 A comparison of spectral amplification factor (SAF) and average spectral amplification (ASA) at different receiver points

Receivers	L23 (f)	L21 (c)	L20 (f)	L18 (t)	L16 (f)	L15 (c)	L13 (f)	L11 (t)	L9 (f)	L8 (c)	L7 (f)	L5 (t)	L2 (f)	C0 (c)
Largest SAF	2.4	2.45	2.39	1.8	3.42	3.45	3.05	2.2	3.7	3.6	3.22	1.62	3.22	3.45
Average SAF	1.17	1.72	1.15	0.75	1.02	1.48	1.05	0.65	1.06	1.43	1.06	0.64	1.22	1.2

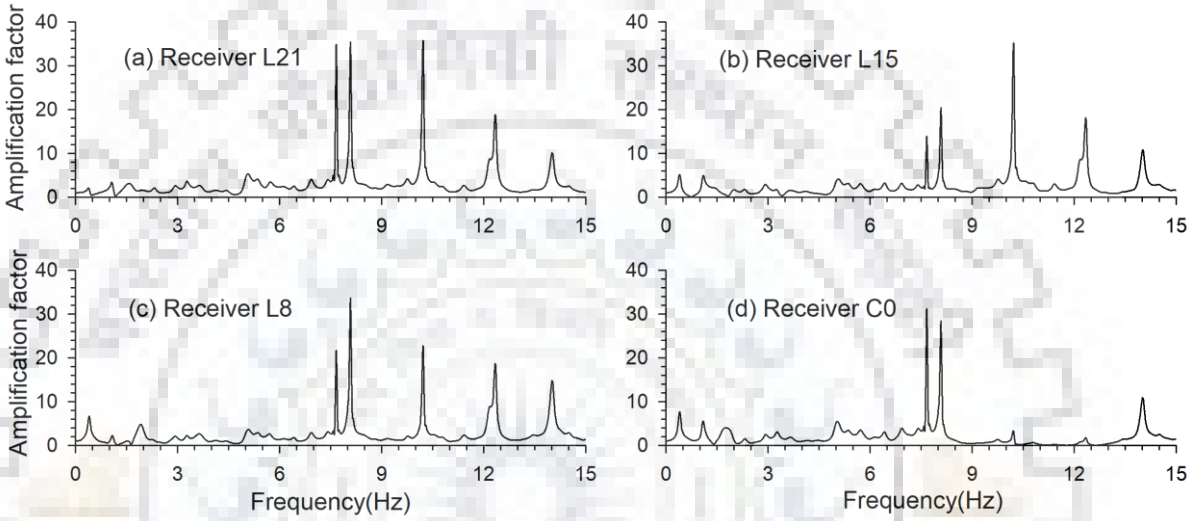

Figure 3.39 Spectral amplification at the top of the ridges wrt the record at the base

The spectral amplification at the top of ridges wrt the record at the base, as shown in figure 3.39, depicts that the obtained largest SAF is 35.5 at frequency 10.21 Hz, 35 at frequency 10.2 Hz, 33.73 at frequency 8.07 Hz at the top of the first ,second, third small ridge respectively. Similarly, the obtained largest SAF is 30.9 at frequency 7.7 Hz at the top of the central ridge. This is much larger than the same obtained using numerical/analytical one. So, it may be the reason behind the reported very large amplification in the case of amplification computed using the record at the top and base of the ridge.

3.6 COMPARISON OF RESULTS BETWEEN TRIANGULAR AND ELLIPTICAL RIDGES

3.6.1 Single triangular ridge (TR1) and elliptical ridge (ER1)

A comparison of SH-wave responses of the TR1 and ER1 model at two locations is shown in the upper panel of figure 3.40. The amplitude at the top of TR1 ridge is more than that on the ER1 ridge. Similarly, a comparison of spectral amplification of the SH-wave along the flank of the TR1 and ER1 model at two locations is shown in the lower panel of figure 3.40. At the ridge top, the average spectral amplification is relatively more at the TR1 model as compared to those on the ER1 model. Further, the spectral amplification is smoother in the case of TR1 model. Table 3.12 depicts that ASA along the flanks of the TR1 model is less than those along the ER1 model.

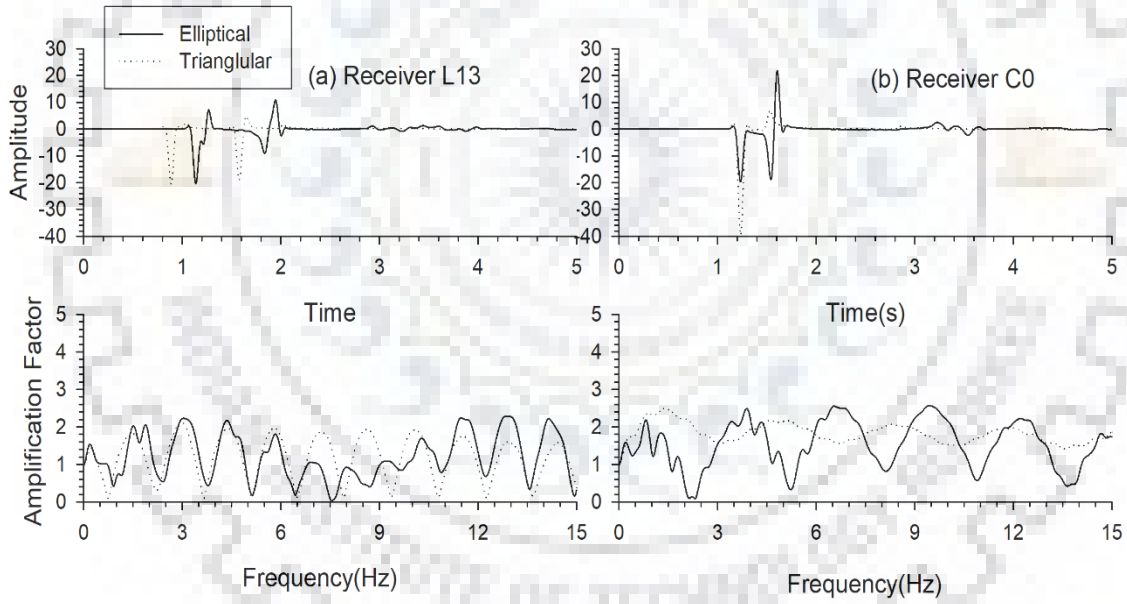

Figure 3.40 A comparison of SH-wave responses and spectral amplification at the TR1 and ER1 model at two locations

Table 3.12 A comparison of average spectral amplification (ASA) obtained of TR1 and ER1 ridge models at different receiver points

Receiver	L13(flank)	C0(crest)
ASA: Triangular	1.178	1.82
ASA: Elliptical	1.21	1.54

3.6.2 Three triangular ridges (TR3) and elliptical ridges (ER3)

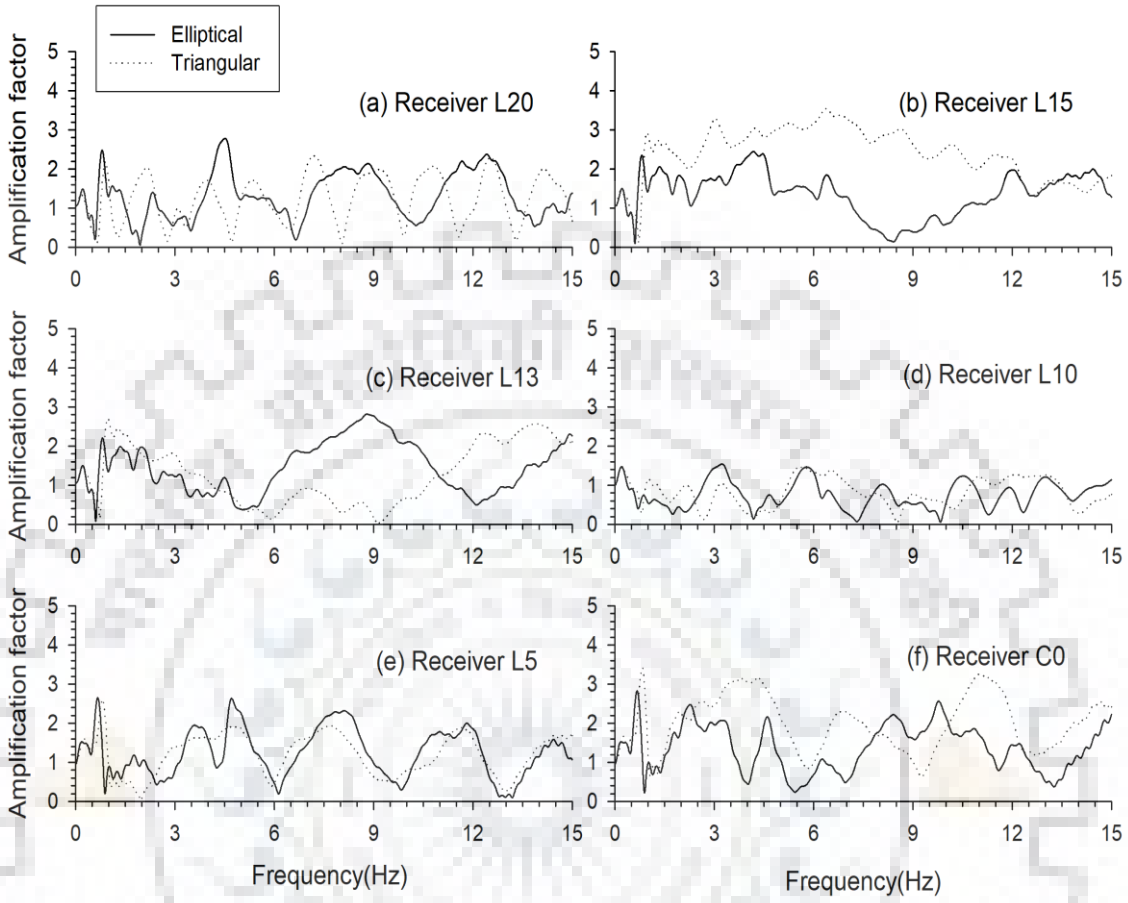

Figure 3.41 Comparison of spectral amplification factors for the TR3 and ER3 topography models

A comparison of spectral amplification of the SH-wave at different locations of TR3 and ER3 models is shown in figure 3.41. At the ridge top of the TR3 ridge, the spectral amplification is relatively more than to those on the ER3 model. Further, at the top of the ridge, the value of largest spectral amplification is also more in the case of TR3 model. Table 3.13 also depicts that ASA at the top of the TR3 model is more than that at the top of the ER3 model. It can also be seen that along the flanks of the ridges ASA is larger in the case of ER3 model than that of TR3 model. For example, at location L13, the obtained ASA are 1.27 and 1.47 in the case of TR3 and ER3 models, respectively. At trough points, value of amplification factor is less in ER3 that means more de-amplification occurs at trough point in ER3.

Table 3.13 A comparison of average spectral amplification (ASA) obtained of TR3 and ER3 ridge models at different receiver points

Receiver	L20(flank)	L15(crest)	L13(flank)	L10(trough)	L5(flank)	C01(crest)
ASA:Triangular	1.25	2.4	1.27	0.82	1.206	2
ASA: Elliptical	1.32	1.36	1.47	0.76	1.24	1.37

3.6.3 Five triangular ridges (TR5) and elliptical ridges (ER5)

A comparison of spectral amplification of the SH-wave at different locations of TR5 and ER5 models is shown in figure 3.42. At the ridge top of the TR5 ridge, the spectral amplification is relatively more than to those on the ER5 model. Further, at the top of the ridge, the value of largest spectral amplification is also more in the case of TR5 model. Table 3.14 also depicts that ASA at the top of the TR5 model is more than that at the top of the ER5 model. At the top of other ridges of the TR5 model, the ASA is larger than that corresponding ridges of the ER5 model. In contrast to this, ASA obtained at the trough of the valleys of the TR5 and ER5 models do not show a specific trend. On the other hand, along the flanks of the ridges at certain location ASA is larger in the case of TR5 model and at certain location ASA is larger in the case of ER5 model.

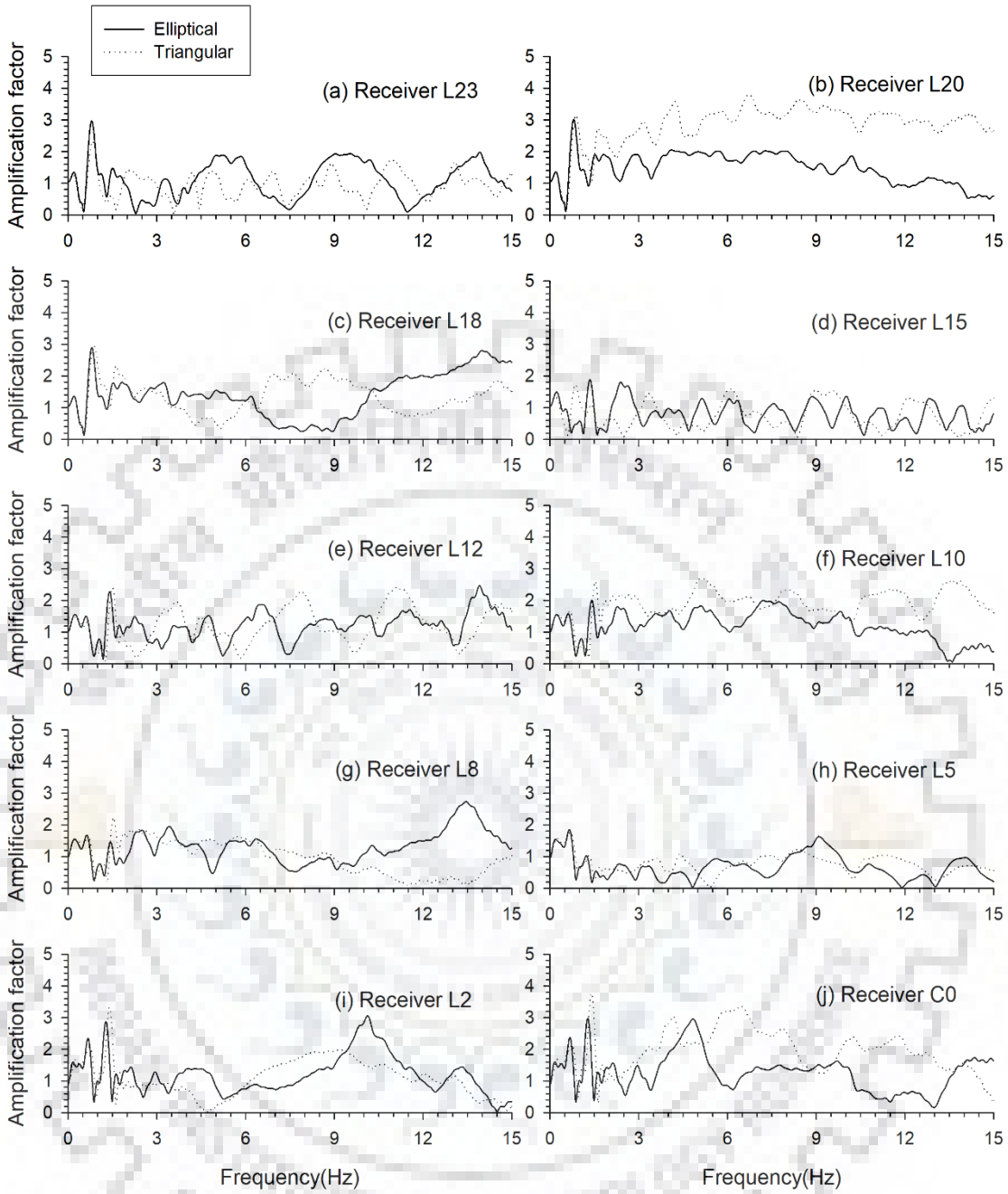

Figure 3.42 Comparison of spectral amplification factors for the TR5 and ER5 topography models

Table 3.14 A comparison of average spectral amplification (ASA) obtained of TR5 and ER5 ridge models at different receiver points

Receivers	L23(f)	L20(c)	L18(f)	L15(t)	L12(f)	L10(c)	L8(f)	L5(t)	L2(f)	C0(c)
ASA Triangular	0.95	2.83	1.34	0.75	1.22	1.9	0.97	0.77	1.11	1.95
ASA Elliptical	1.12	1.47	1.42	0.79	1.21	1.21	1.3	0.67	1.2	1.26

3.6.4 Seven triangular ridges (TR7) and elliptical ridges (ER7)

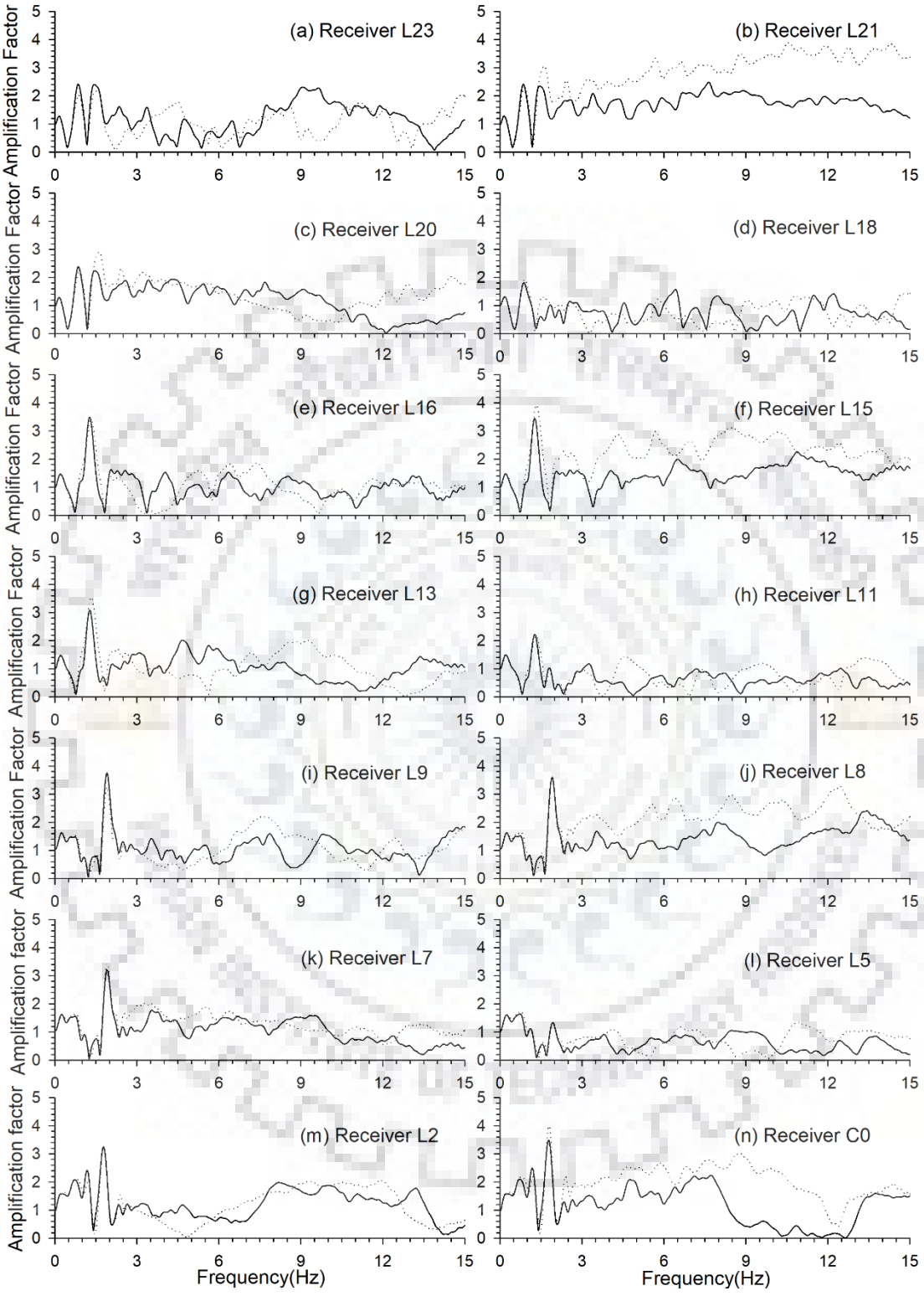

Figure 3.43 Comparison of spectral amplification factors for the TR7 and ER7 topography models

A comparison of spectral amplification of the SH-wave at different locations of TR7 and ER7 models is shown in figure 3.43. At the ridge top of the TR7 ridge, the spectral amplification is relatively more than to those on the ER7 model. Further, at the top of the ridge, the value of largest spectral amplification is also more in the case of TR7 model. Table 3.15 also depicts that ASA at the top of the TR7 model is more than that at the top of the ER7 model. At the top of other ridges of the TR7 model, the ASA is larger than that corresponding ridges of the ER7 model. Similarly, at the trough of the valleys of the TR7 model, the ASA is also larger than those corresponding valleys of the ER7 model means more de-amplification occur at trough points in ER7 than that of TR7. On the other hand, along the flanks of the ridges at certain location ASA is larger in the case of TR7 model and at certain location ASA is larger in the case of ER7 model.

Table 3.15 A comparison of average spectral amplification (ASA) obtained of TR7 and ER7 ridge models at different receiver points

Receivers	L23 (f)	L21 (c)	L20 (f)	L18 (t)	L16 (f)	L15 (c)	L13 (f)	L11 (t)	L9 (f)	L8 (c)	L7 (f)	L5 (t)	L2 (f)	C0 (c)
ASA Triangular	1.05	2.86	1.35	0.77	1.04	2.25	1.07	0.77	1.09	2.12	1.3	0.79	1.22	2
ASA Elliptical	1.17	1.72	1.15	0.75	1.02	1.48	1.05	0.65	1.06	1.43	1.06	0.64	1.22	1.18

CHAPTER #4

QUANTIFICATION OF COMPLEX VALLEY TOPOGRAPHY EFFECTS ON THE GROUND MOTION CHARACTERISTICS

4.1 INTRODUCTION

The literature review on the valley-topography effects on the ground motion shows that most of the researchers have used a single valley with different shape and shape-ratio. The SH-wave responses of the considered complex triangular and elliptical valley-topography models have been computed and analyzed to predict the spatial variation of amplification and de-amplification along the flanks of the sub-ridges and sub-valleys.

4.2 DISCRETIZATION OF MODELS AND INPUT PARAMETERS

Free surface is taken at 400m from top in homogenous and valley models. The plane wave front of the SH-wave have been generated by using shear stress in the form of Gabor wavelet at a depth of 1350 m below the free surface. Other parameters are kept same as in previous chapter.

4.3 SH-WAVE RESPONSE OF HOMOGENOUS MODEL

To compare the effects of valley topography, first response of ground motion without topography is computed and analyzed. Figure 4.1 shows the homogenous model named model PLANE. 51 Recorders are placed from -1000m to 1000 m at an interval of 40 m spacing.

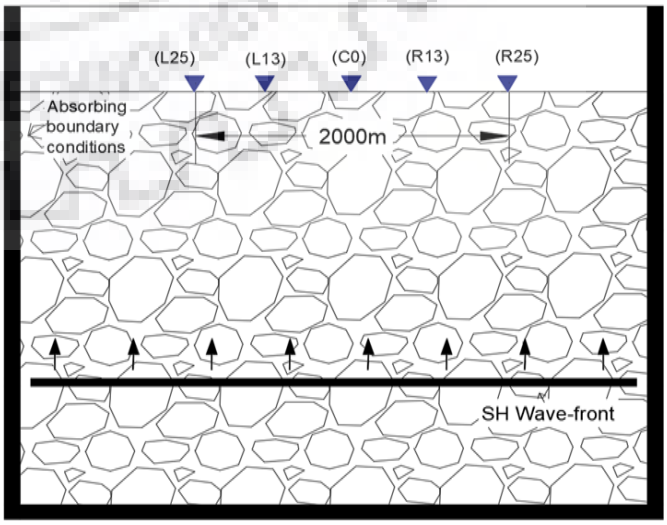

Figure 4.1 Homogeneous half-space model

Figure 4.2 shows the SH-wave response of homogeneous model at different receiver points.

Analysis of figure 4.2 reveals that the amplitude is same for all the receiver points at surface, which is obvious for homogenous medium.

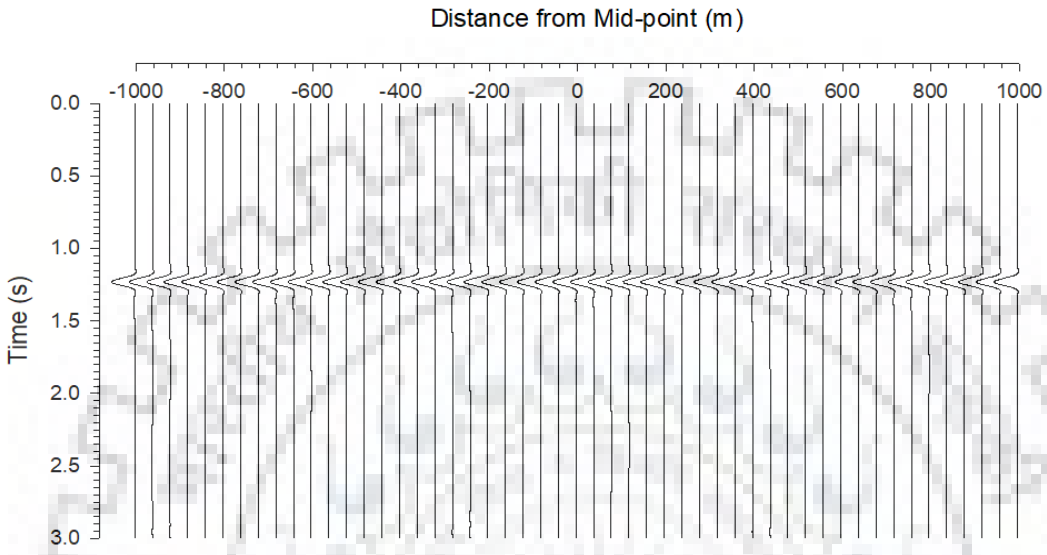

Figure 4.2 SH-wave response of the homogeneous

Figure 4.3 shows the variation of spectral amplitude of SH-wave with respect to frequency for central receiver C0. The frequency bandwidth for generated wave is 0-15 Hz. The dominant frequency is 5 Hz. Figure clearly shows that spectral amplitude stays almost constant at lower frequencies and gradually decreases as frequency increases.

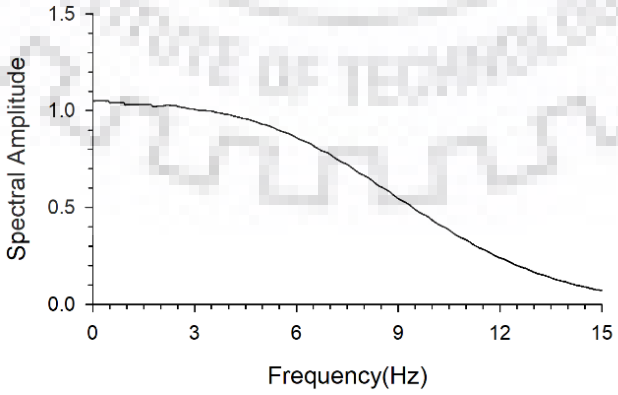

Figure 4.3 Spectra of recorded ground motion

4.4 SH-WAVE RESPONSE OF TRIANGULAR VALLEYS

Table 4.1 Valley models

TV1	Single triangular valley	EV1	Single elliptical valley
TV3	Three triangular valley	EV3	Three elliptical valley
TV5	Five triangular valley	EV5	Five elliptical valley
TV7	Seven triangular valley	EV7	Seven elliptical valley

Four triangular and elliptical valley models have been considered with one, three, five and seven valleys as given in the table 4.1. The overall dimension of all the valley models is same. Further, the receiver array and source are also same.

4.4.1 SH-wave response of single triangular valley

To see the response of single triangular valley, the considered model is named as TV1 with a single triangular valley. 51 Recorders are placed from grid -1000m to 1000m at 10 grid spacing. We have considered valley of height of 1000m and width 2000 m i.e. shape ratio of valley is 1.0

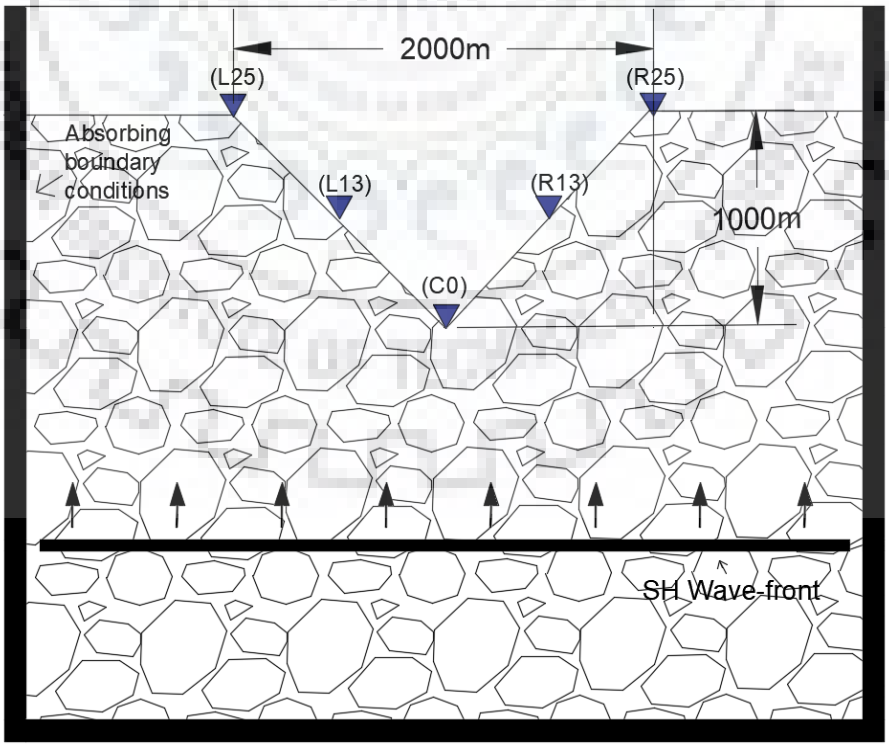

Figure 4.4 Single triangular valley model (TV1) along with receivers array

(a) Time domain response

The seismic response of the TV1 model is shown in figure 4.5. The analysis shows the de-amplification of seismic response at the trough of valley as compared to homogenous half-space model. Figure 4.5 shows that minimum amplitude occurs at the trough of valley due to defocusing of waves. The incident SH-wave and the diffracted waves from the trough and the top corners are very clearly visible.

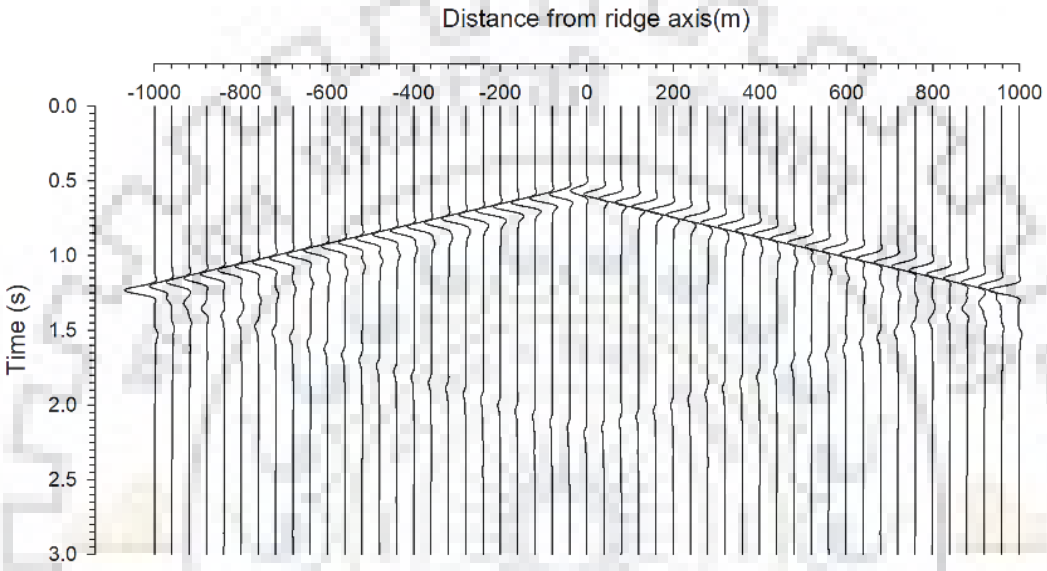

Figure 4.5 Particle velocity response for the TV1 model

(b) Snapshots of wave-field

To infer the behavior of SH-wave after interacting with the valley topography, snapshots have been computed at different moments from 0.5s to 2.25s and shown in Fig 4.6. It can be seen from snapshots that as SH-wave-front moves upwards, first it reaches the trough of valley at time about 0.5s and thereafter it is diffracted by the tip of the valley and reflected by valley flanks. The snapshot at time 0.5s shows only the incident wave in the considered area. The snapshot at time 0.75s shows the incident plane wave front as well as the reflected waves from the flanks of the triangular valley. The incident, diffracted and reflected waves are annotated in snapshots. The snapshots at times 1.5s, 1.75s and 2.0s clearly reveal the downward propagation of the reflected diffracted SH-wave along the flanks of the valley. The diffracted wave at the tip of the

valley has opposite polarity to that of the incident or the diffracted waves propagating downward.

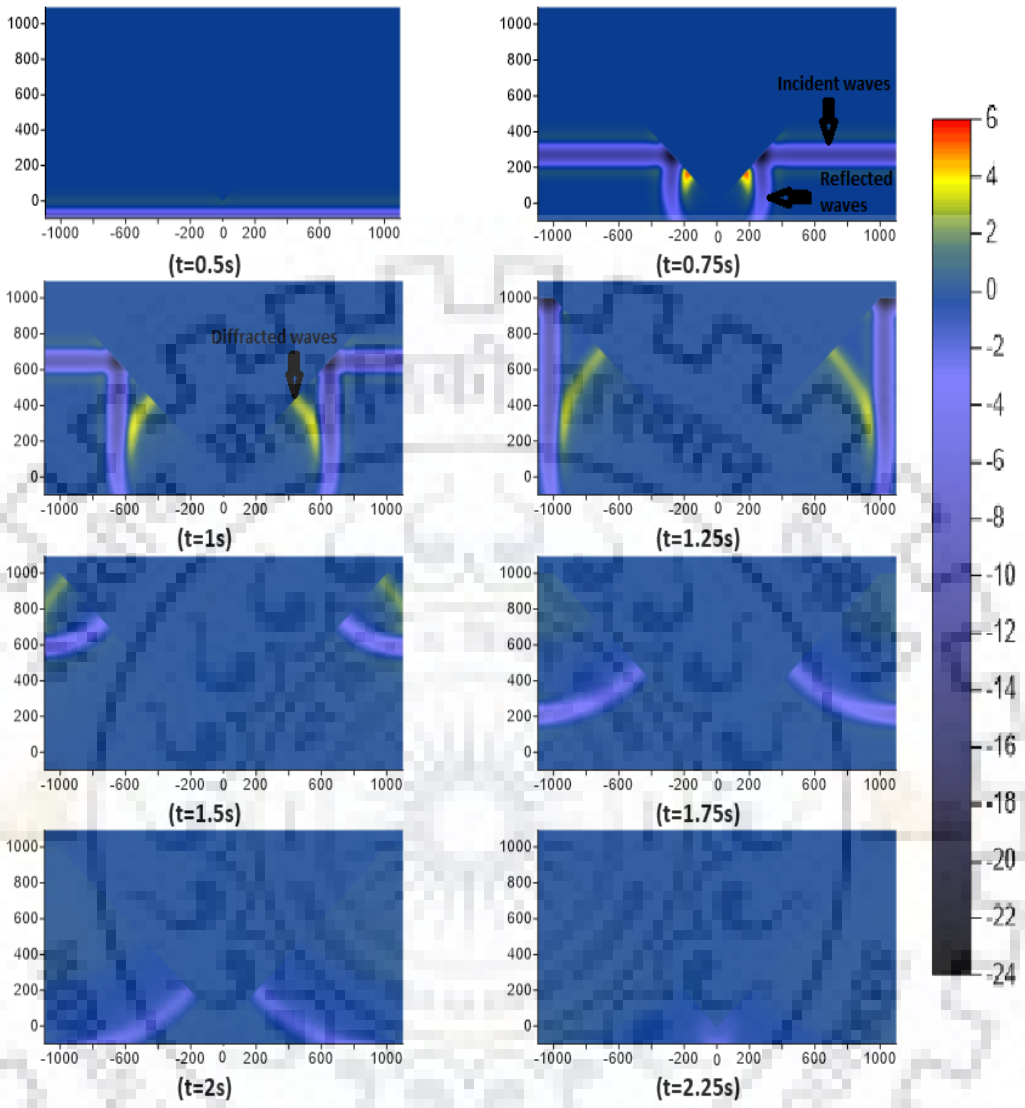

Figure 4.6 Snapshots of SH-wave at different moments for TV1 model

(c) Spectral amplification factor

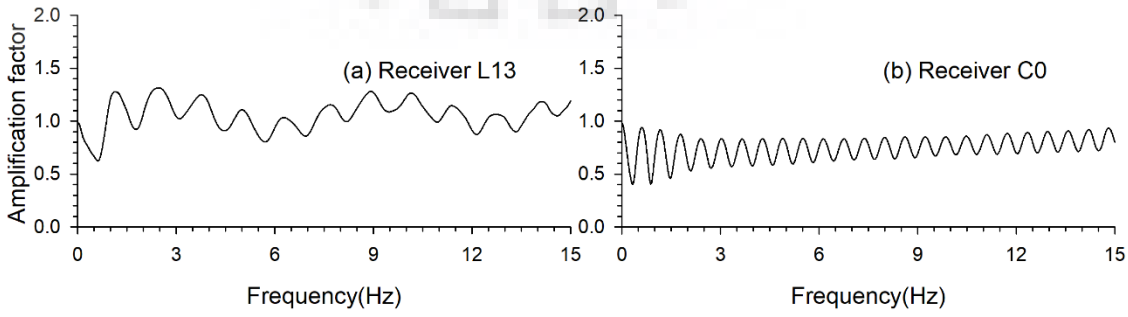

Figure 4.7 Spectral amplification factor at two locations for TV1 model

Figure 4.7a&b shows the spectral amplification factor caused by TV1 at L13 and C0 recording point, respectively which is found by dividing the spectral amplitude of TV1 to that of half-space model at the corresponding location.

Table 4.2 A comparison of spectral amplification factor (SAF), average spectral amplification (ASA) at different receiver points with the analytical one

Receiver location	L13(flank)	C0(trough)
Largest SAF: Numerical value	1.3	0.8 at 0.75Hz
Average SAF: Numerical value	1.05	0.75
SAF : Analytical value	---	0.67 at 0.75Hz

The largest SAF for wavelength matching with the top width of the valley can be obtained analytically as

$\pi/\varphi=0.67$ Angle $\varphi=270^0$

at frequency $f=V/\lambda$ Velocity of SH-wave V= 1500m/s

$f=1500/2000$ Top width of valley λ= 2000m

$= 0.75$Hz

An analysis of table 4.2 reveals that the obtained SAF numerically is 0.8 at frequency 0.75Hz which is larger than that obtained analytically (0.67). Analytical value of amplification factor is found lesser than numerical value, this may be because of non-consideration of diffracted waves in the analytical solution. However, ASA is closer to the analytical value.

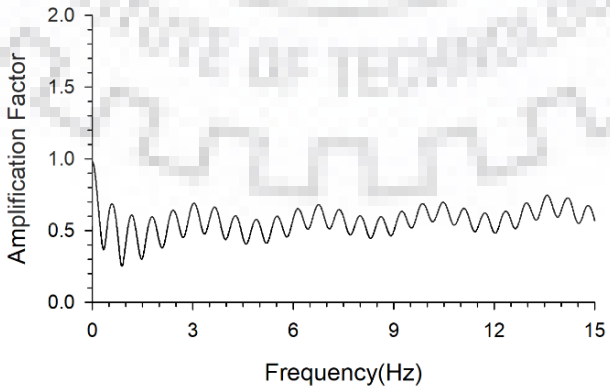

Figure 4.8 Spectral amplification at the center of valley wrt the record at the ground level

The spectral amplifications at the trough of valley wrt the record at the top of the valley, as shown in figure 4.8, depicts that the largest SAF is 0.74 at frequency 13.5 Hz. A comparison of figure 4.7 and 4.8 depicts that the obtained de-amplification at the trough of the valley in figure 4.8 is larger. Means, computation of amplification/de-amplification along the flanks of a valley wrt to the records near the top corners of the valley is not appropriate one.

4.4.2 SH-wave response of three triangular valley

A topography model with three triangular valleys is shown in figure 4.9. The SH-wave response of the model is computed at 51 Recorder points, extending from -1000m to 1000 m at an interval of 40 m spacing in the horizontal direction. The height and width of this multi-valley model 1000 m and 2000 m, respectively.

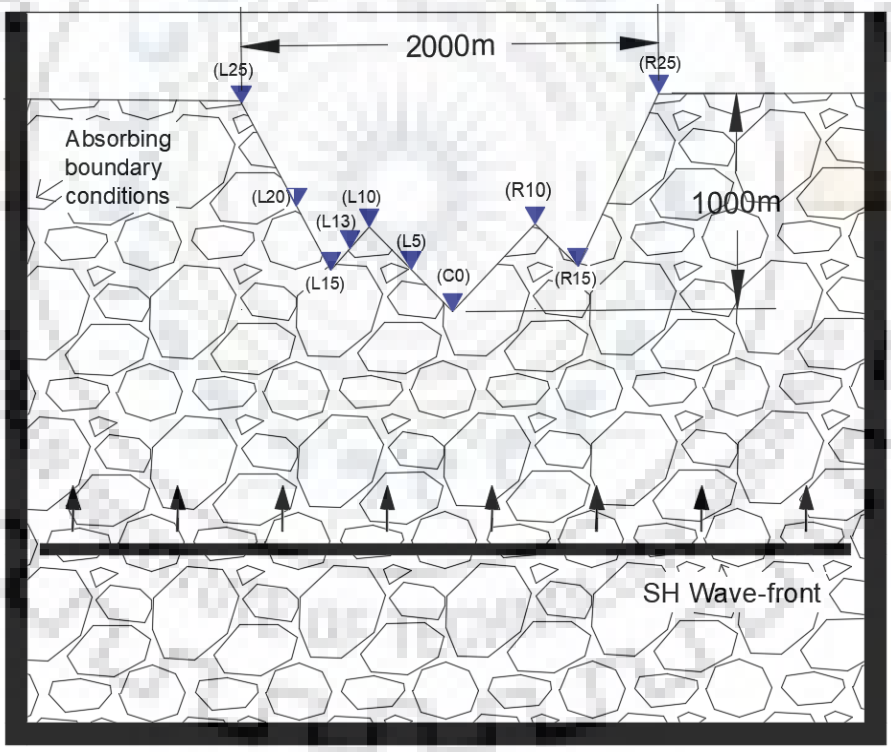

Figure 4.9 Three triangular valleys model (TV3) along with receivers array

(a) Time domain response

The seismic response of the TV3 valley model is shown in figure 4.10. The analysis of this figure shows more amplification of the SH-wave at the top corners of valley and the

top of the sub-ridge in the model. A de-amplification of the SH-wave at trough of the valleys as compared to the amplitude in the case of homogenous half-space model can also be inferred. Figure 4.10 shows that maximum amplitude occurs at the top corners of the valley and minimum amplitude at the trough points of the valley. The incident SH-wave and the diffracted waves from the corners of the valley are very clearly visible. An increase of duration of ground motion in the case of complex valley topography as compared to the solo-topography model can be inferred.

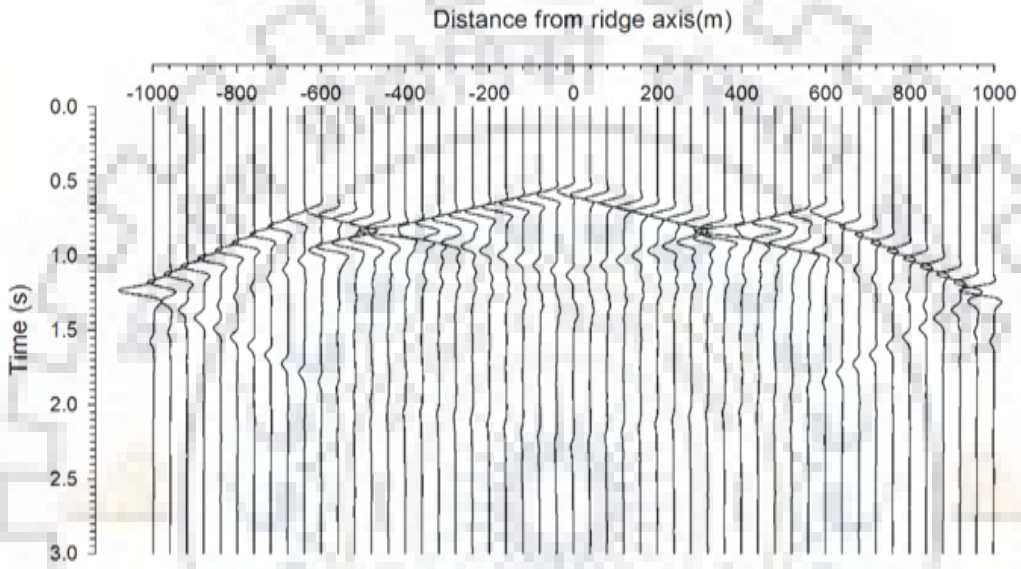

Figure 4.10 SH-wave response of the TV3 valley topography model

(b) Snapshots of wave-field

To infer the behavior of SH-wave after interacting with the complex valley topography, snapshots have been computed at different moments from 0.5s to 2.25s and shown in Fig 4.11. The snapshot at time 0.5s shows only the incident wave in the considered rectangular area. The snapshot at time 0.75s shows the incident plane S-wave front as well as the reflected waves from the flanks of the outer triangular valleys. The incident, diffracted and reflected waves are annotated in the snapshots. A comparison of this snapshot with that of a solo-topography reveals very complex wave fronts due to the presence of multiples valleys and ridges.

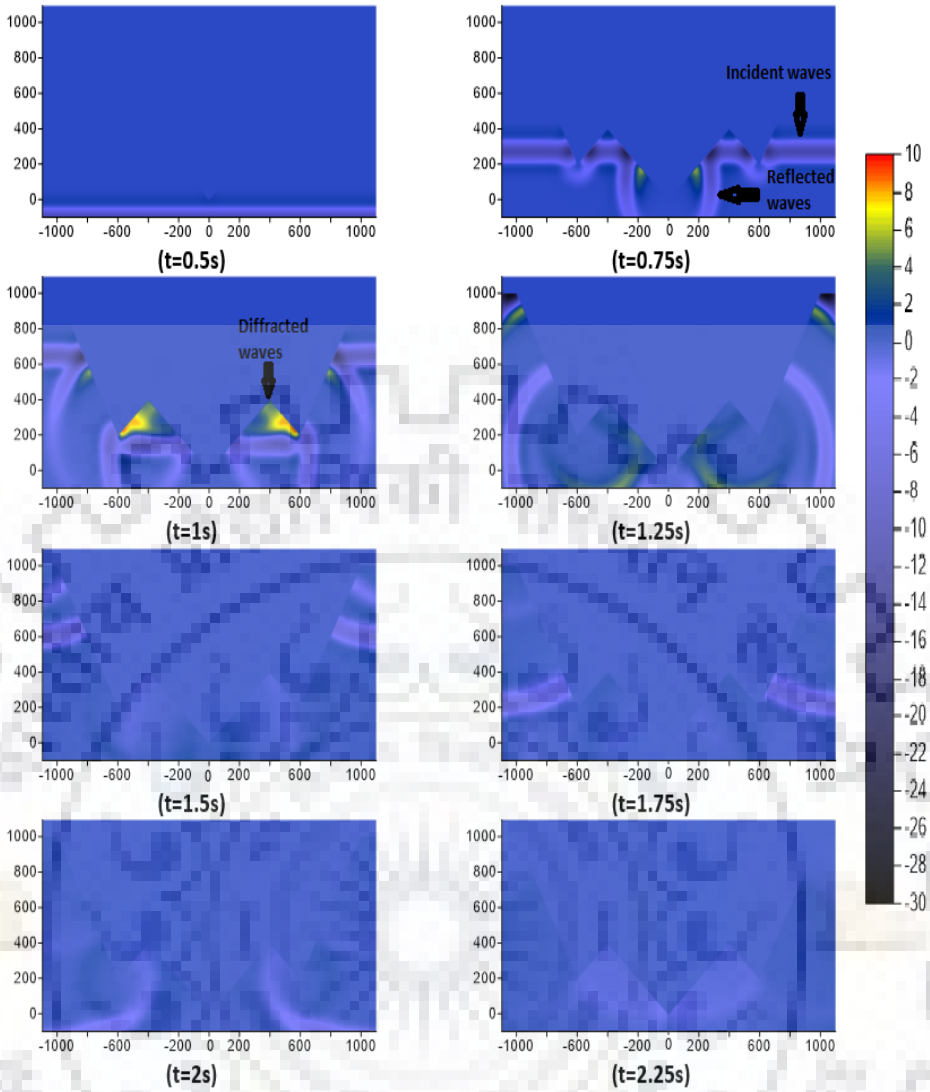

Figure 4.11 Snapshots of SH-wave front at different moments for TV3 model

(c) Spectral amplification factor

Figure 4.12 shows the spectral amplification factors at different recording points along the flanks of the TV3 valley topography model. An analysis of table 4.3 reveals that the numerically obtained SAF increases with the increase of number of valleys in the model. For example, the obtained largest SAF at trough of central valley (1.57) is larger than that obtained analytically (0.67). Analytical value of amplification factor is found lesser than numerical value at the trough of the first valley also. Further, at the trough of the first valley there is amplification of ground motion as compared to the de-amplification obtained analytically (0.63). However, ASA at the trough of the first valley depicts a de-amplification of ground motion. The obtained ASA is largest at the

crest of the first sub-ridge (2.75) and it is more than the analytical value (1.81). Amplification of the SH-wave is found at crest of sub-ridge by both numerical and analytical approaches. Amplification factor for a valley is affected by its own shape features as well as features of surrounding neighboring sub-ridge and valley. The diffractions and reflection of waves occur and may be the reason of some unusual behavior in the case of multi-valley models.

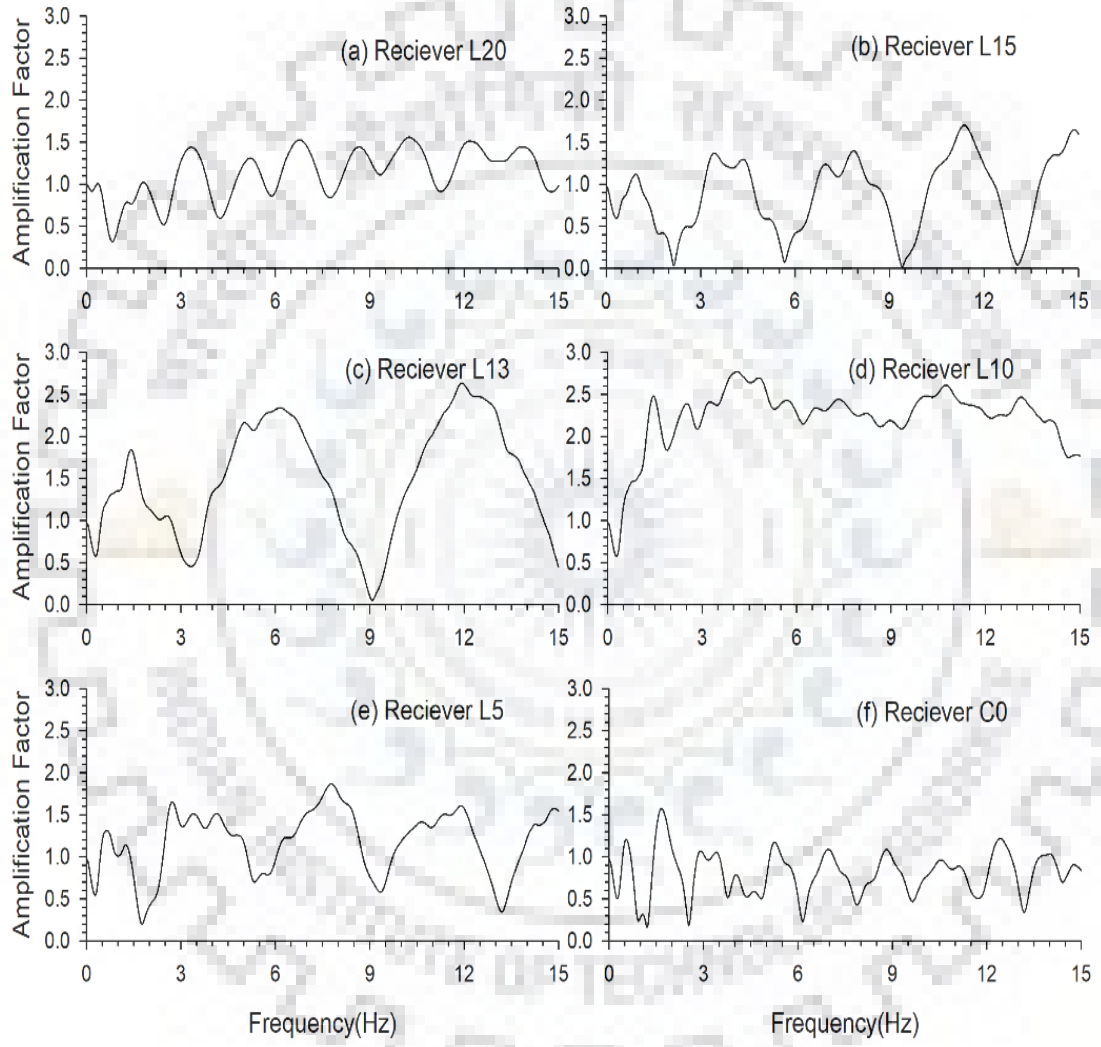

Figure 4.12 Amplification factor at various locations for TV3 model

Table 4.3 A comparison of spectral amplification factor (SAF), average spectral amplification at different receiver points with the analytical one

Receiver points	L20(F)	L15(T)	L13(F)	L10(C)	L5(F)	C0 (T)
Largest SAF: numerical	1.5	1.6	2.6	2.75	1.87	1.57
Average SAF: numerical	1.13	0.88	1.48	2.22	1.17	0.8
Largest SAF: analytical	---	0.63	---	1.81	---	0.67

The spectral amplifications at the trough of the valleys wrt the record at the top of the valley, as shown in figure 4.13, depicts that the obtained largest SAF is 1.15 at frequency 11.35 Hz at the center of the first small valley. Similarly, the obtained largest SAF is 1.3 at frequency 1.6 Hz at the trough of central valley. Overall, the de-amplification of ground motion is lesser than that shown in figure 4.13.

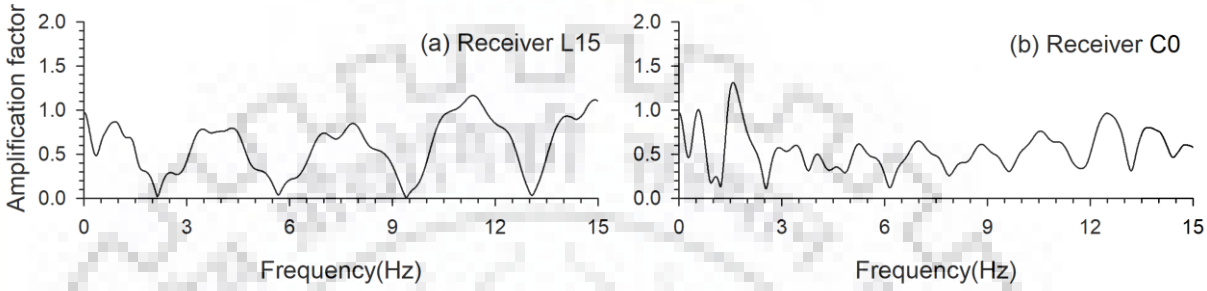

Figure 4.13 Spectral amplification at the trough of the valleys wrt the record at the ground level

4.4.3 SH-wave response of five triangular valleys

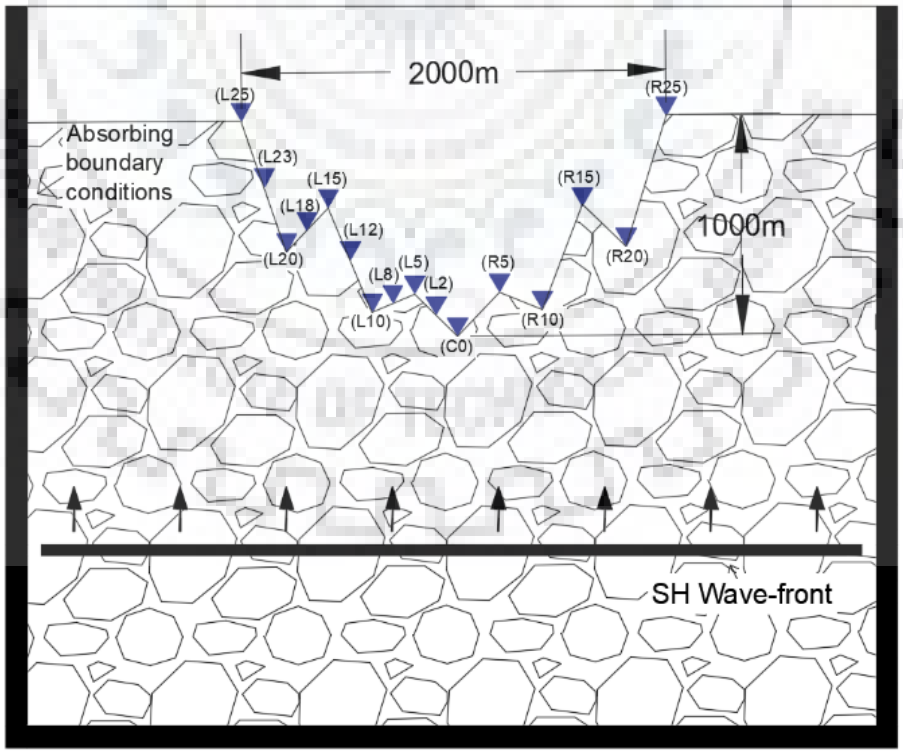

Figure 4.14 Five triangular valley model (TV5) along with receivers array

A topography model with five triangular valleys is shown in figure 4.14. The SH-wave response of the model is computed at 51 Recorder points, extending from -1000m to 1000 m at an interval of 40 m spacing in the horizontal direction. The height and width of this multi-valley model 1000 m and 2000 m, respectively.

(a) Time domain response

The seismic response of the TV5 complex valley model is shown in figure 4.15. The analysis of this figure shows more amplification of SH-wave at the crest of sub-ridges and less amplification of the SH-wave at trough of the valleys as compared to the amplitude in the case of homogenous half-space model. Figure 4.15 shows that maximum amplitude occurs at the top of sub-ridges and minimum amplitude at the trough and flank points of the valley. The incident SH-wave and the diffracted waves from the corners of the valley are very clearly visible. An increase of duration of ground motion in the case of complex valley topography as compared to the solo-topography model can also be inferred.

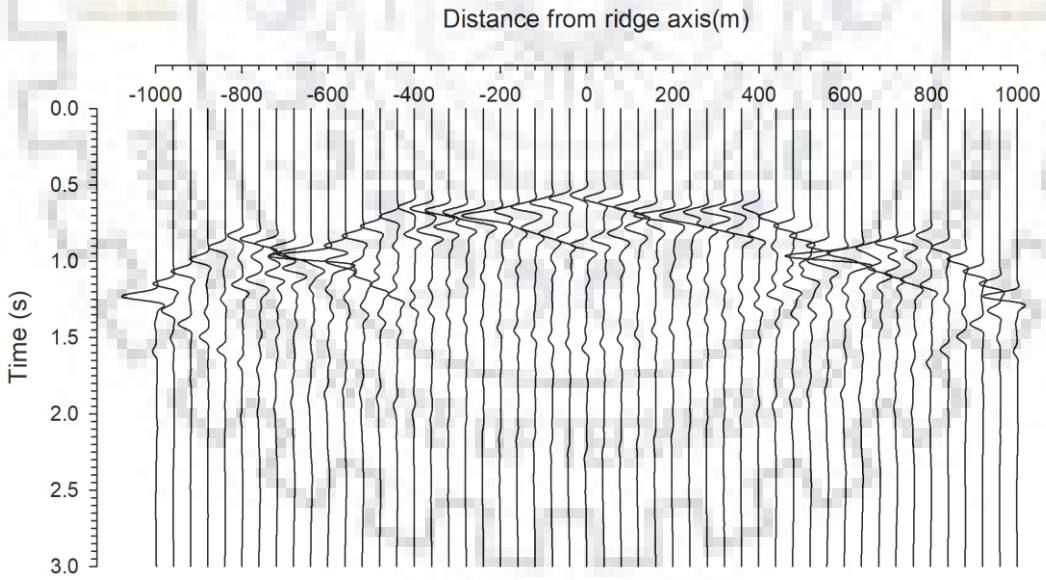

Figure 4.15 SH-wave response of the TV5 valley topography model

(b) Spectral amplification factor

Figure 4.16 shows the spectral amplification factor at different recording points along the flanks and top of the TV5 valley topography model. An analysis of table 4.4 reveals

that the obtained SAF numerically shows an increase of differences with the increase of number of valleys in the model. For example, the obtained largest SAF at the trough of central valley as 1.95 is larger to that obtained analytically (0.67). Analytical value of amplification factor is found lesser than numerical value at the trough of the first and second valleys also. Further, at the trough points of the valleys there is amplification of ground motion as compared to the de-amplification obtained analytically (0.61 & 0.68, at the trough of first and second valley). The obtained very large amplification for most of frequencies at receiver L15 may be its location on the sub-ridge of the TV5 model..

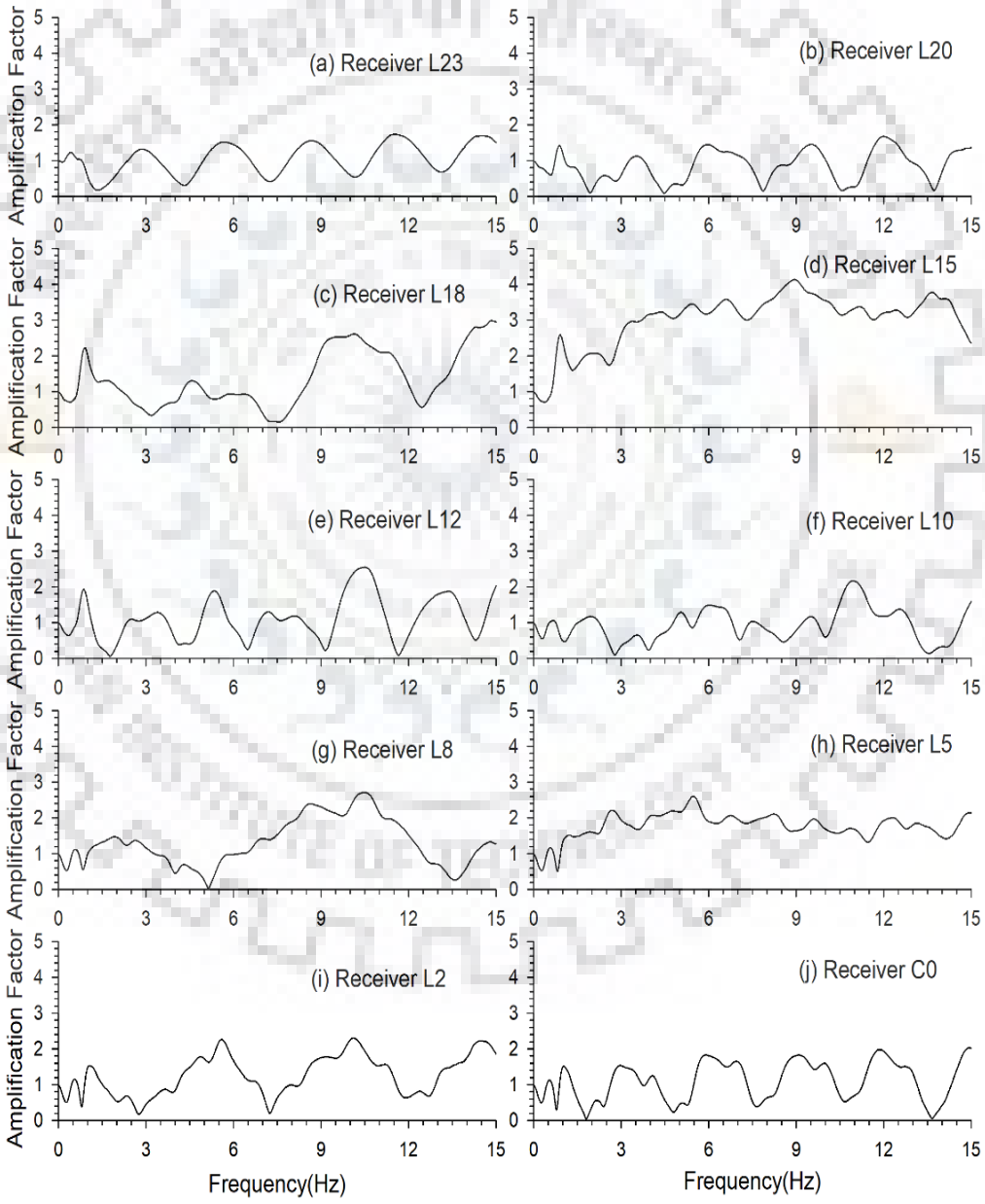

Figure 4.16 Spectral amplification factor at various locations for TV5 model

However, ASA at the trough points of the valleys depicts a de-amplification of ground motion. The obtained ASA is largest at the crest point of the first ridge (3.0).Amplification factor at trough for center valley is lesser than that of adjacent valleys even though it has more depth because apex angle is more for center valley. It reveals apex angle or shape ratio is major factor for governing amplification factor. Amplification factor for a valley is affected by its own shape features as well as features of surrounding neighboring valley and ridge. Diffraction and reflection of waves occur and may be the reason of some unusual behavior in the case of multi-valleys.

Table 4.4 A comparison of spectral amplification factor (SAF), average spectral amplification at different receiver points with the analytical one

Receivers	L23(f)	L20(t)	L18(f)	L15(c)	L12(f)	L10(t)	L8(f)	L5(c)	L2(f)	C0(t)
Largest SAF-Num	1.68	1.73	2.9	4.1	2.53	2.1	2.7	2.61	2.3	1.95
Average SAF-Num	1.04	0.85	1.35	3	1.1	0.92	1.3	1.77	1.26	1.1
SAF-Analytical	---	0.61	---	2.65	---	0.68	---	1.6	---	0.67

The spectral amplification at the trough of the valleys wrt the record at the ground level, as shown in figure 4.17, depicts that the obtained largest SAF is 1.23 at frequency 1.02 Hz, 1.11 at frequency 1.83 Hz at the center of the first and second small valley respectively. Similarly, the obtained largest SAF is 1.72 at frequency 1.11 Hz at the trough of the central valley. This is lesser than the same obtained using numerical/analytical one.

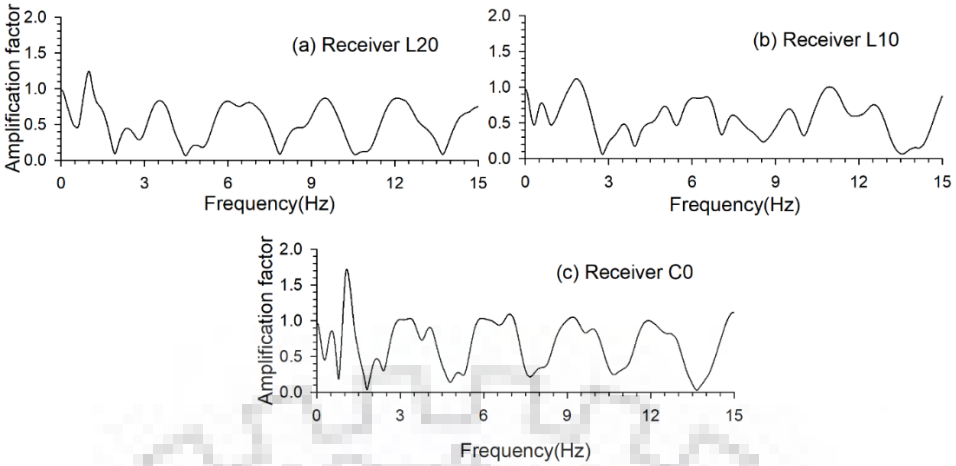

Figure 4.17 Spectral amplification at the trough of the valleys wrt the record at the ground level

4.4.4 SH-wave response of seven triangular valleys

A topography model with seven triangular valleys (TV7 model) is shown in figure 4.18. The SH-wave response of the model is computed at 51 Recorder points, extending from -1000m to 1000 m at an interval of 40 m spacing in the horizontal direction. We have considered total height and width of multi-valleys 1000 m and 2000 m respectively.

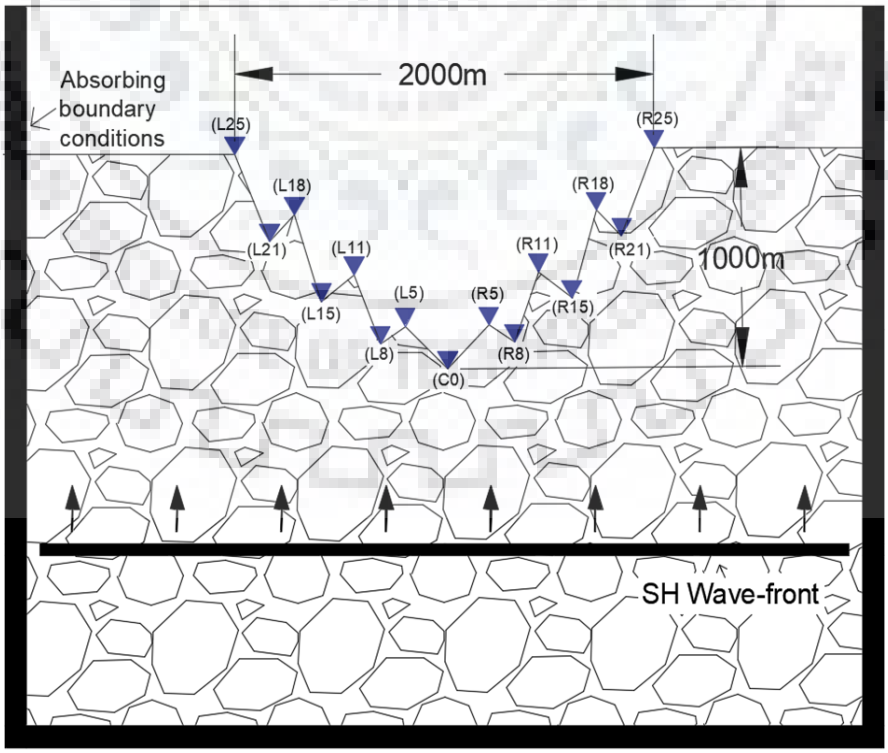

Figure 4.18 TV7 topography model with seven triangular valleys

(a)Time domain response

The SH-wave response of the TV7 model is shown in figure 4.19. The analysis of this figure shows more amplification of the SH-wave at the crest of sub-ridges and top-corners of valley and less amplification of the SH-wave at trough of the valleys as compared to the amplitude in the case of homogenous half-space model. The incident SH-wave and the diffracted waves from the corners of the valley are very clearly visible. An increase of duration of ground motion in the case of complex valley topography as compared to the solo-topography model can be inferred.

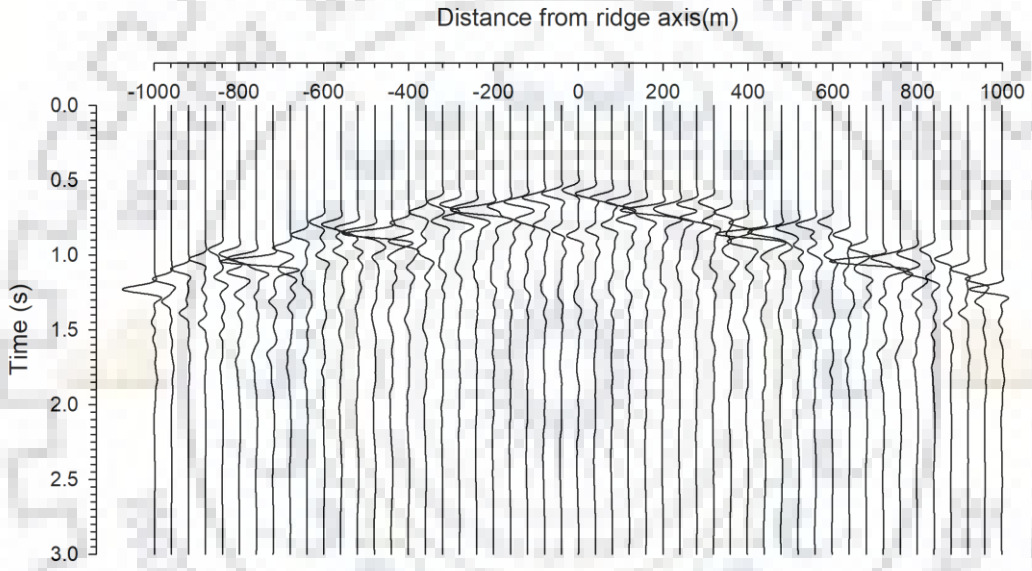

Figure 4.19 SH-wave response of the TV7 valley topography model

(b) Spectral amplification factor

Figure 4.20 shows the spectral amplification factors at different recording points along the top of the TV7 valley topography model. An analysis of table 4.5 reveals that the obtained differences in SAF corresponding to numerical and analytical values increases of with the increase of number of valleys in the model. For example, the obtained largest SAF at the trough of central valley is 1.72 as to that obtained analytically (0.67). Analytical value of amplification factor is found lesser than numerical value at the center of the first, second and third valleys also. Further, at the trough of the valley there is amplification of ground motion as compared to the de-amplification obtained

analytically (0.61, 0.62 & 0.63, at the trough of first, second and third valley). However, ASA at the trough of the valleys depicts a de-amplification of ground motion.

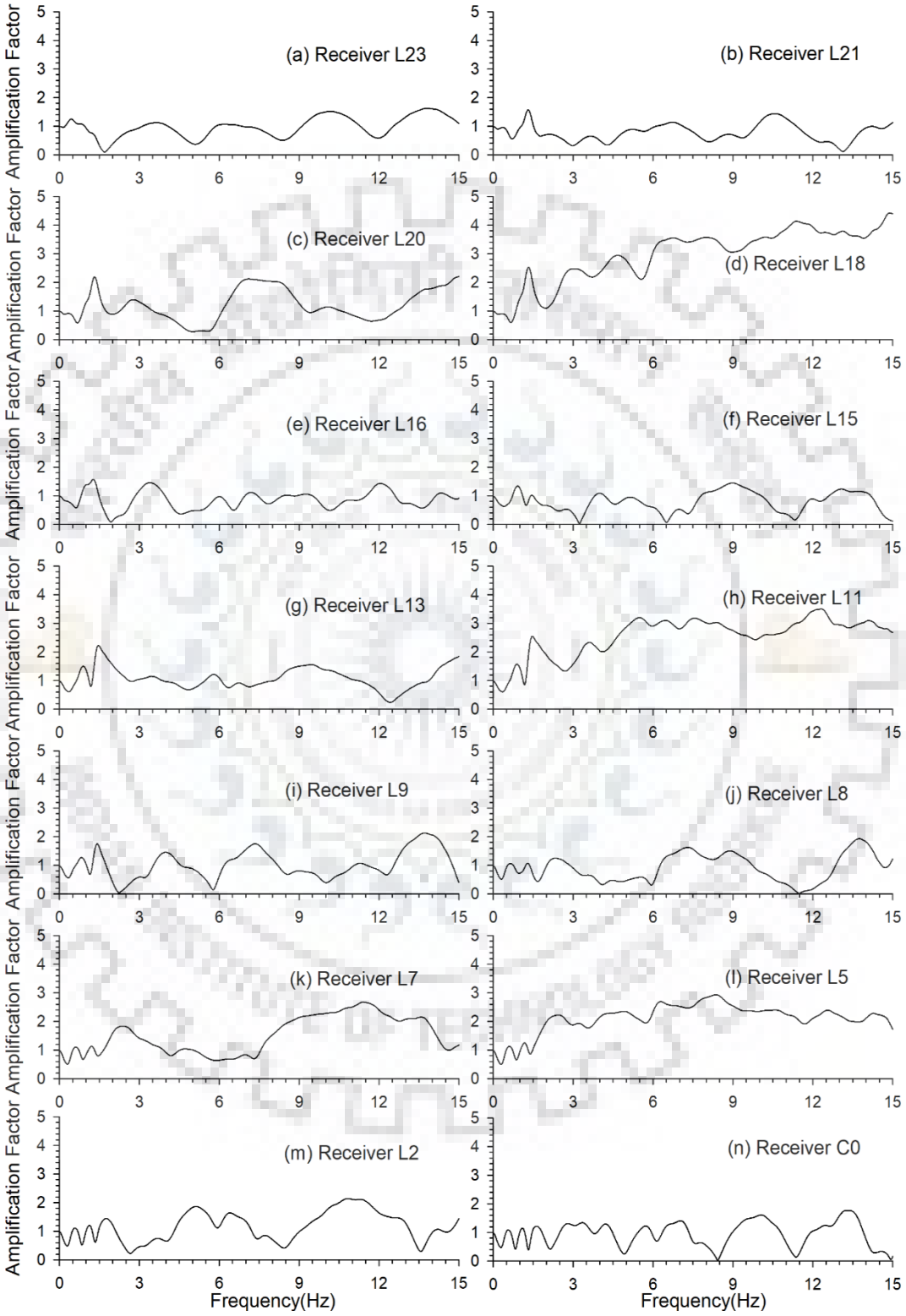

Figure 4.20 Spectral amplification factors at various locations for the TV7 model

The obtained ASA is largest at the crest of the first sub-ridge. Amplification factor for a sub-ridge/valley is affected by its own shape features as well as features of surrounding neighboring ridges. Diffraction and reflection of waves occur and may be the reason of some unusual behavior in the case of multi-valleys.

Table 4.5 A comparison of spectral amplification factor (SAF), average spectral amplification at different receiver points with the analytical one

Receivers	L23 (f)	L21 (t)	L20 (f)	L18 (c)	L16 (f)	L15 (t)	L13 (f)	L11 (c)	L9 (f)	L8 (t)	L7 (f)	L5 (c)	L2 (f)	C0 (t)
Largest SAF:Num	1.6	1.55	2.2	4.35	1.5	1.4	2.18	3.48	2.08	1.9	2.7	2.9	2.07	1.72
Average SAF:Num	0.98	0.78	1.2	3	0.85	0.79	1.07	2.55	1.02	0.91	1.51	2.12	1.17	0.95
SAF:Anal	---	0.61	---	3.6	---	0.62	---	2.43	---	0.63	---	1.81	---	0.67

The spectral amplification at the trough of the valleys wrt the record at the top corner of valley, as shown in figure 4.21, depicts that the obtained largest SAF is 1.4 at frequency 1.5 Hz, 1.33 at frequency 1.5 Hz, 1.13 at frequency 7.13 Hz at the center of the first ,second, third sub-valleys, respectively. Similarly, the obtained largest SAF is 1.74 at frequency 1.6 Hz at the trough of the central valley. This is lesser than the same obtained using numerical.

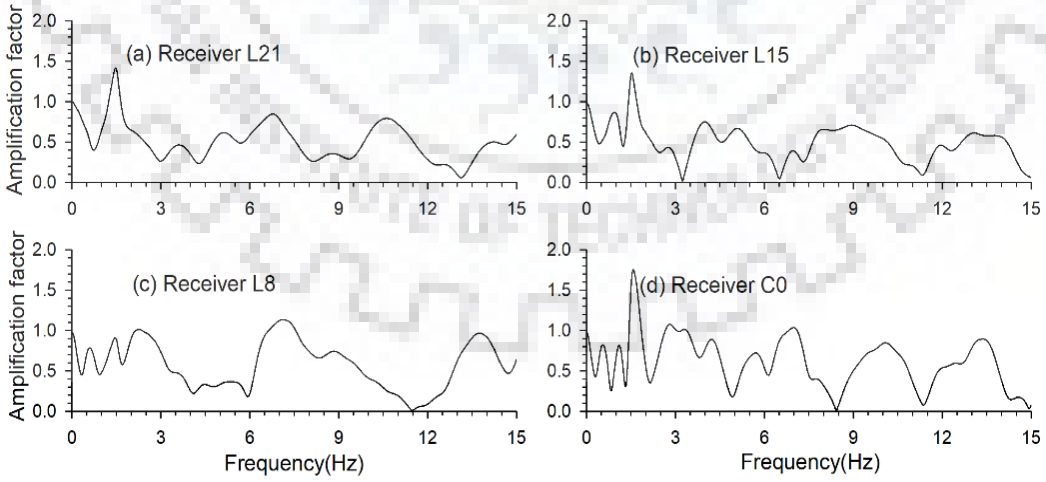

Figure 4.21 Spectral amplification at the trough of the valleys wrt the record at the ground level

4.5 SH-WAVE RESPONSE OF ELLIPTICAL VALLEYS

4.5.1 SH-wave response of single elliptical valley

A topography model with one elliptical valley is shown in figure 4.22. The SH-wave response of the model is computed at 51 recording points, extending from -1000m to 1000 m at an interval of 40 m spacing in the horizontal direction. The height and width of this valley model 1000 m and 2000 m, respectively.

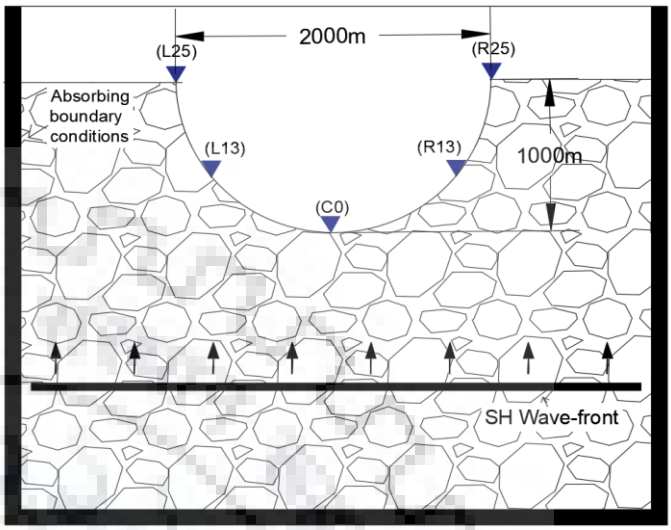

Figure 4.22 Single elliptical valley model (EV1) along with receivers array

(a)Time domain response

The SH-wave response of the EV1 model is shown in figure 4.23. The analysis shows more-amplification of seismic response at the corners of valley at ground level compared to homogenous half-space model. Figure 4.23 shows that minimum amplitude occurs at the trough of valley. The incident SH-wave and the diffracted waves from the corners are very clearly visible.

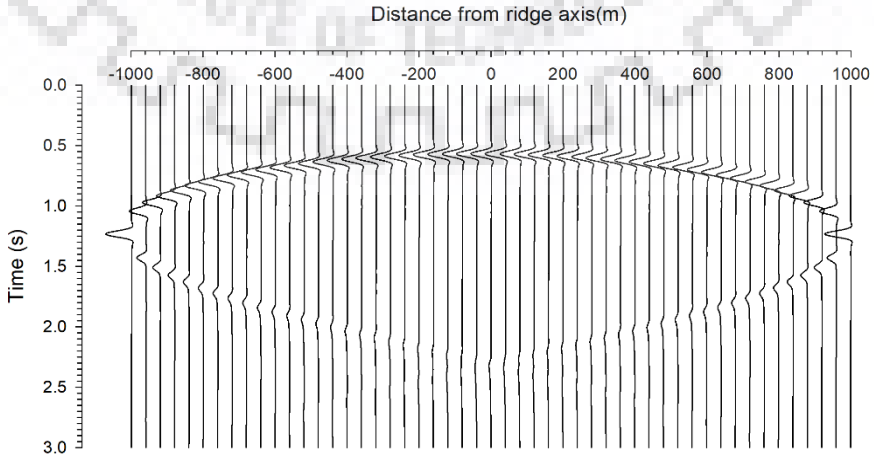

Figure 4.23 SH-wave response of the EV1 valley topography model

(b) Snapshots of wave-field

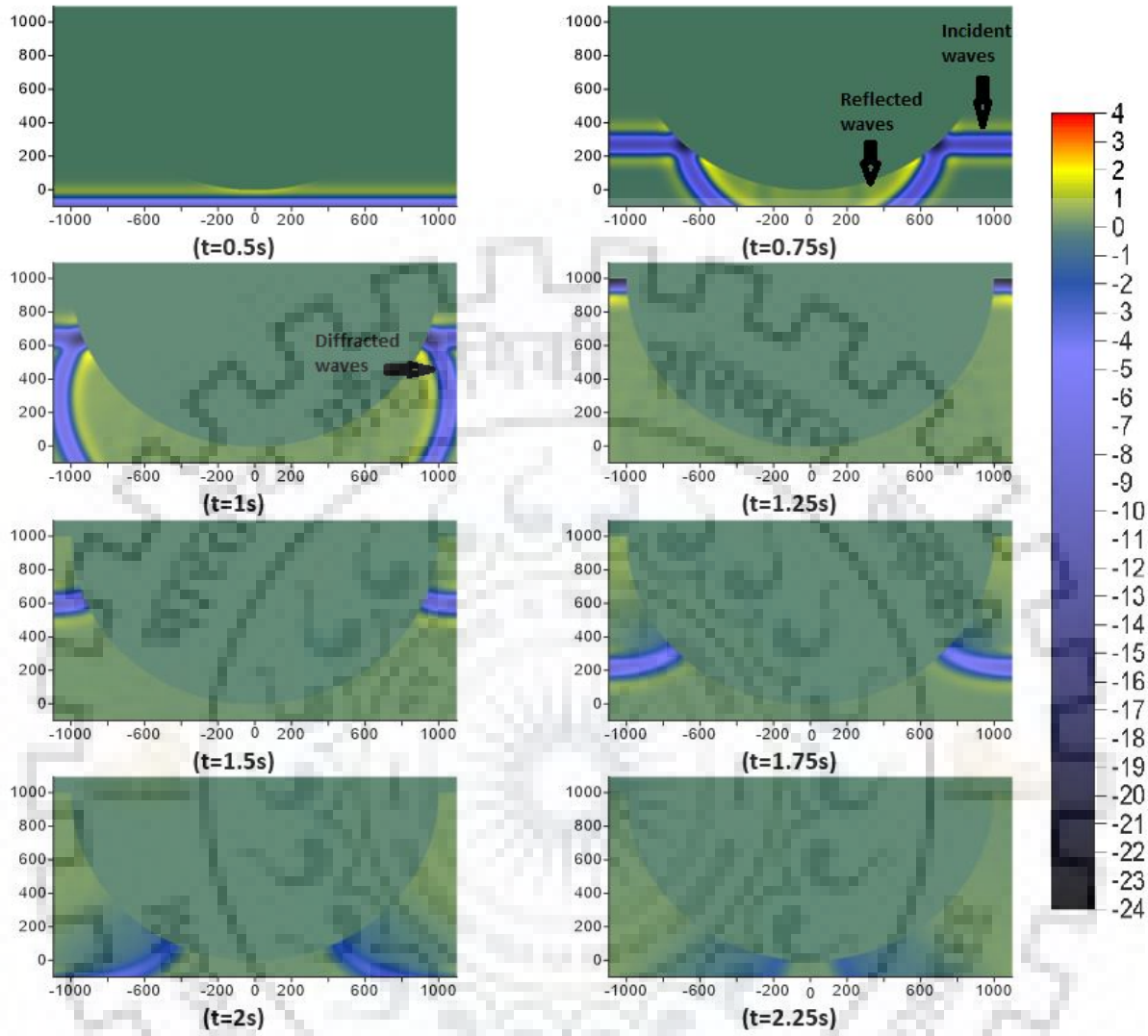

Figure 4.24 Snapshots of SH-wave at different moments for EV1 model

To infer the behavior of SH-wave after interacting with the elliptical valley, snapshots have been computed at different moments from 0.5s to 2.25s and shown in Fig 4.24. It can be seen from snapshots that as SH-wave-front moves upwards, first it reaches the trough of valley at time about 0.5s and thereafter it is reflected by valley flanks. The snapshot at time 0.5s shows only the incident wave in the considered area. The snapshot at time 0.75s shows the incident plane wave front as well as the reflected waves from the flanks of the valley. The incident and reflected waves are annotated in snapshots. The snapshots at times 1.5s, 1.75s and 2.0s clearly reveal the downward propagation of the reflected diffracted S-wave along the flanks of the valley.

(c) Spectral amplification factor

Figure 4.25a&b shows the spectral amplification factor of EV1 at L13 and C0 recording point, respectively. An analysis of table 4.6 reveals that the obtained SAF numerically is 1.27 which is larger than that obtained in case of the corresponding triangular valley.

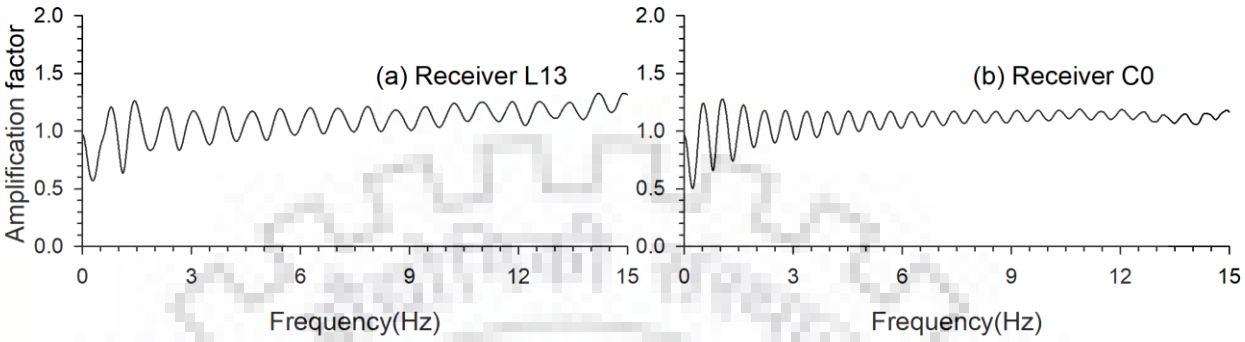

Figure 4.25 Spectral amplification factors at two locations for ER1 model

Table 4.6 A comparison of spectral amplification factor (SAF) and average spectral amplification (ASA) at different receiver points

Receiver	L13(flank)	C0(trough)
Largest SAF: numerical	1.3	1.27
ASA	1.09	1.09

The spectral amplification at the trough of elliptical valley wrt the record at the top corner, as shown in figure 4.26, depicts that the largest SAF is 0.99 at frequency 0.52 Hz. This is lesser than the same obtained using numerical one.

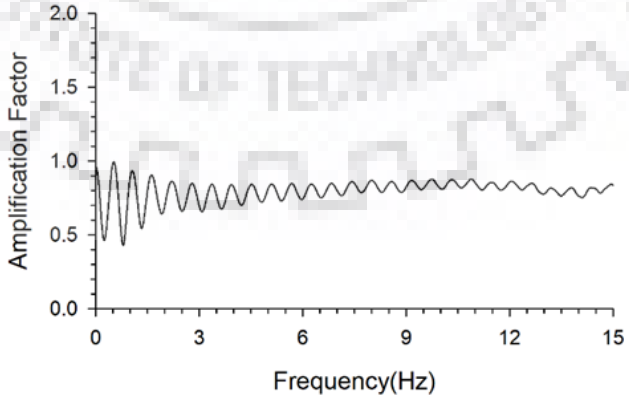

Figure 4.26 The spectral amplifications at the center of elliptical valley wrt the record at the ground level

4.5.2 SH-wave response of three elliptical valleys

A topography model with three elliptical valley EV3 is shown in figure 4.27. The SH-wave response of the model is computed at 51 recording points, extending from -1000m to 1000 m at an interval of 40 m spacing in the horizontal direction.

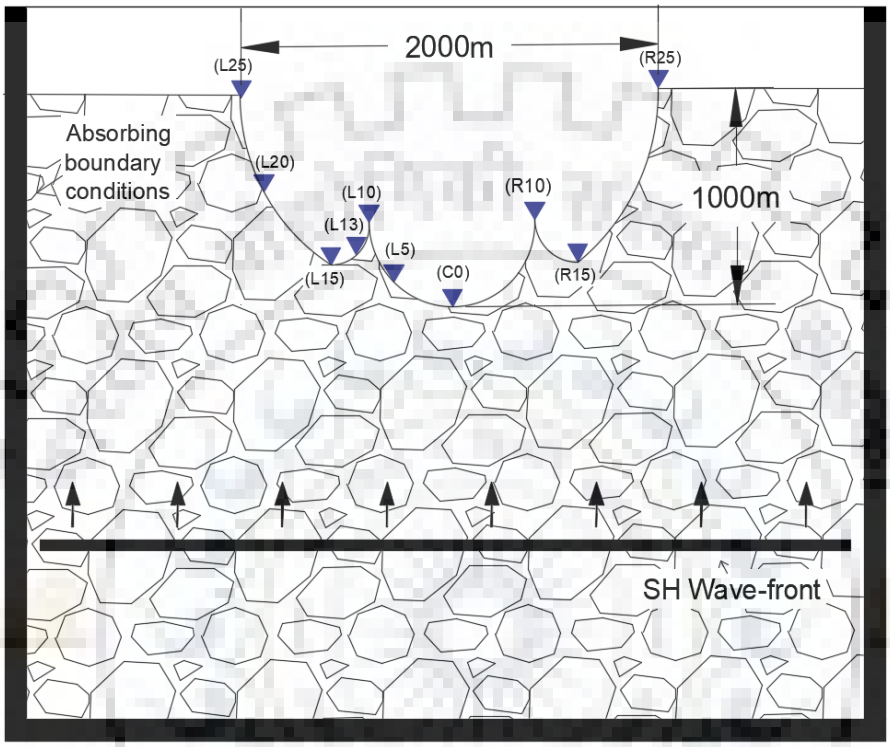

Figure 4.27 Three elliptical valleys model (EV3) along with receivers array

(a)Time domain response

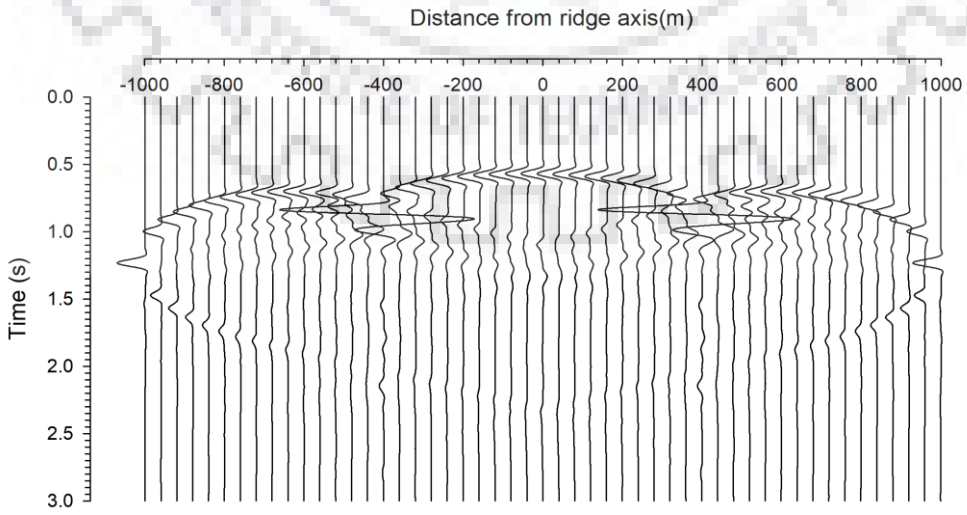

Figure 4.28 SH-wave response of the EV3 Model

The SH-wave response of the EV3 valley model is shown in figure 4.28. The analysis of this figure shows the huge amplification of SH-wave at the crest of sub-ridge and less amplification at the trough of the elliptical valley as compared to the amplitude in the case of homogenous half-space model. A drastic increase of duration of ground motion due to increase of complexity can be inferred. The incident SH-wave and the diffracted waves from the corners of the valley are very clearly visible.

(b) Snapshots of wave-field

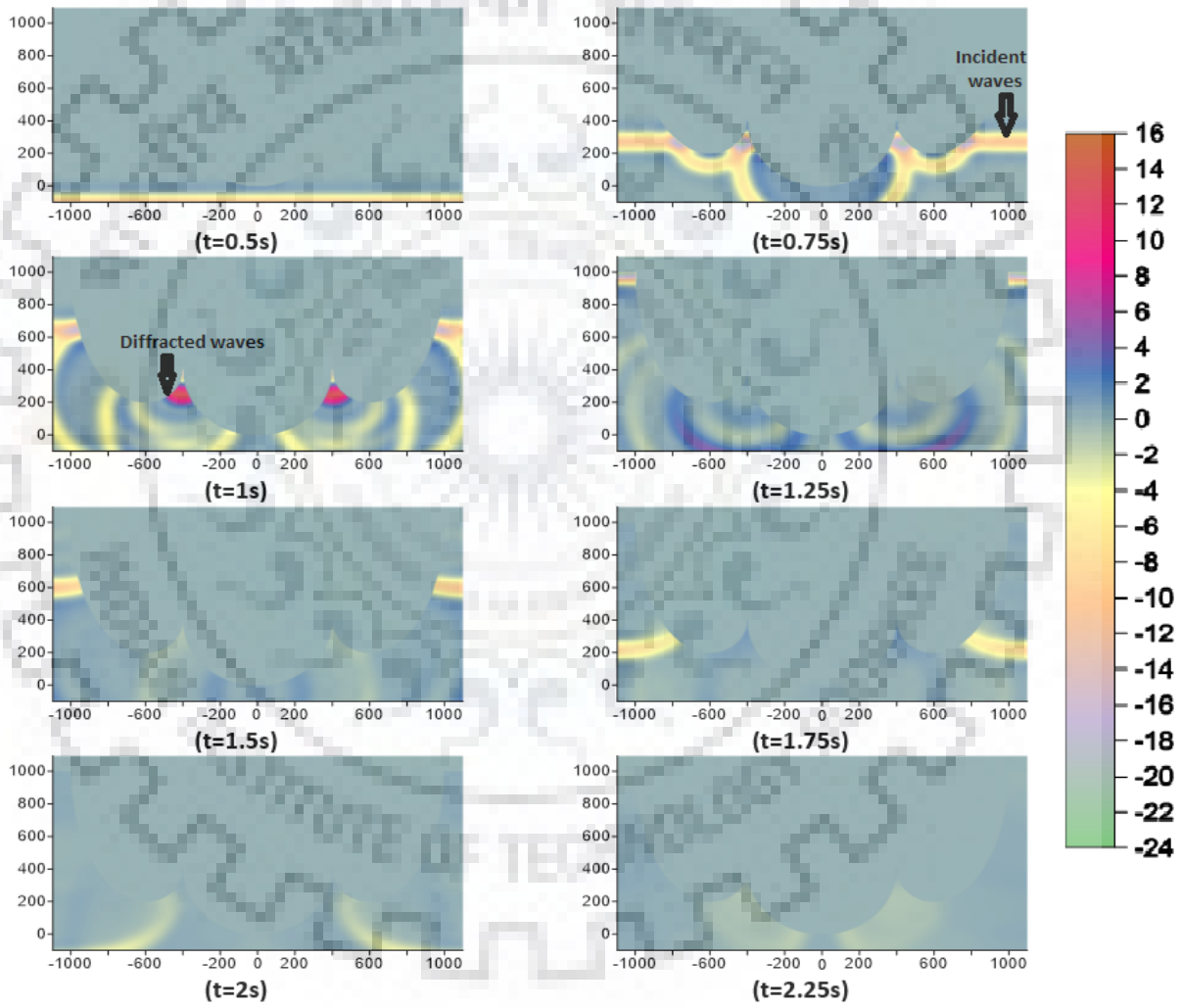

Figure 4.29 Snapshots of SH-wave front at different moments for EV3 model

The snapshots have been computed at different moments from 0.5s to 2.25s and shown in Fig 4.29. It can be seen from snapshots that as wave-front moves upwards, it is reflected by valley topography. The snapshot at time 0.5s shows only the incident wave

in the considered area. The snapshot at times 0.75s and 1.0s show the incident plane wave front, diffracted as well as the reflected waves from the flanks of the elliptical valley. Maximum amplitude can be seen at crest of sub-ridge in the snapshot at time 1.0 s due to proper focusing of waves.

(c) Spectral amplification factor

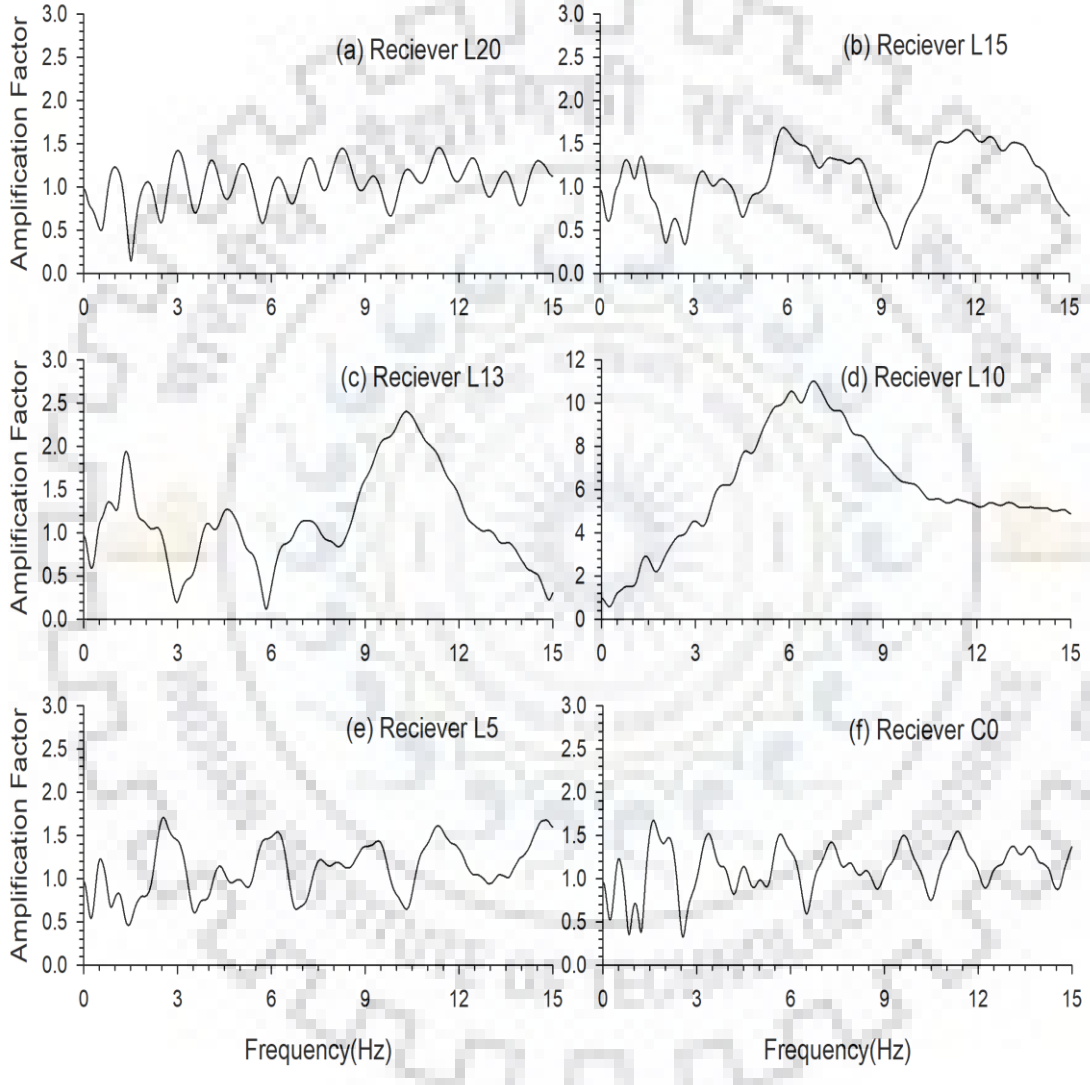

Figure 4.30 Spectral amplification factors at various locations for EV3 model

Figure 4.30 shows the spectral amplification factors at different recording points along the top of the EV3 valley topography model. An analysis of table 4.7 shows that the obtained largest SAF at crest of sub-ridge is 11 which is enormous amplification and proper focusing of reflected and diffracted waves may be the reason for this. Further, at

the trough point of the valley there is amplification of ground motion (1.68) as compared to expected de-amplification. ASA at the trough of the first valley also depicts an amplification of ground motion (1.12). Amplification occurs at the trough point of center valley also (1.67). In this case, not any peak point experiences de-amplification. Amplification factor for a valley is affected by its own shape features as well as features of surrounding neighboring valleys. Diffraction and reflection of waves occur and may be the reason of some unusual behavior in the case of multi-valleys.

Table 4.7 A comparison of spectral amplification factor (SAF) and average spectral amplification (ASA) at different receiver points

Receiver	L20(flank)	L15(trough)	L13(flank)	L10(crest)	L5(flank)	C0(trough)
Largest SAF	1.45	1.68	2.4	11	1.71	1.67
Average SAF	1.04	1.12	1.14	6.05	1.12	1.1

The spectral amplification at the top of elliptical valley wrt the record at the top corners of valley, as shown in figure 4.31, depicts that the obtained largest SAF is 1.25 at frequency 1.37 Hz at the center of the first sub-valley. Similarly, the obtained largest SAF is 1.56 at frequency 1.44 Hz at the trough of central valley. This is much lesser than the same obtained numerically.

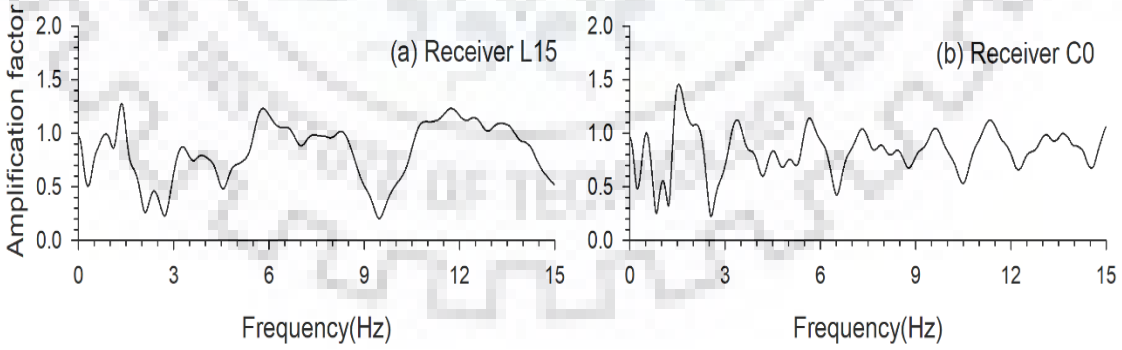

Figure 4.31 The spectral amplifications at the top of the elliptical valley wrt the record at the ground level

4.5.3 SH-wave response of five elliptical valleys

A topography model with five elliptical valleys EV5 is shown in figure 4.32. The SH-wave response of the model is computed at 51 recording points, extending from -1000m to 1000 m at an interval of 40 m spacing in the horizontal direction.

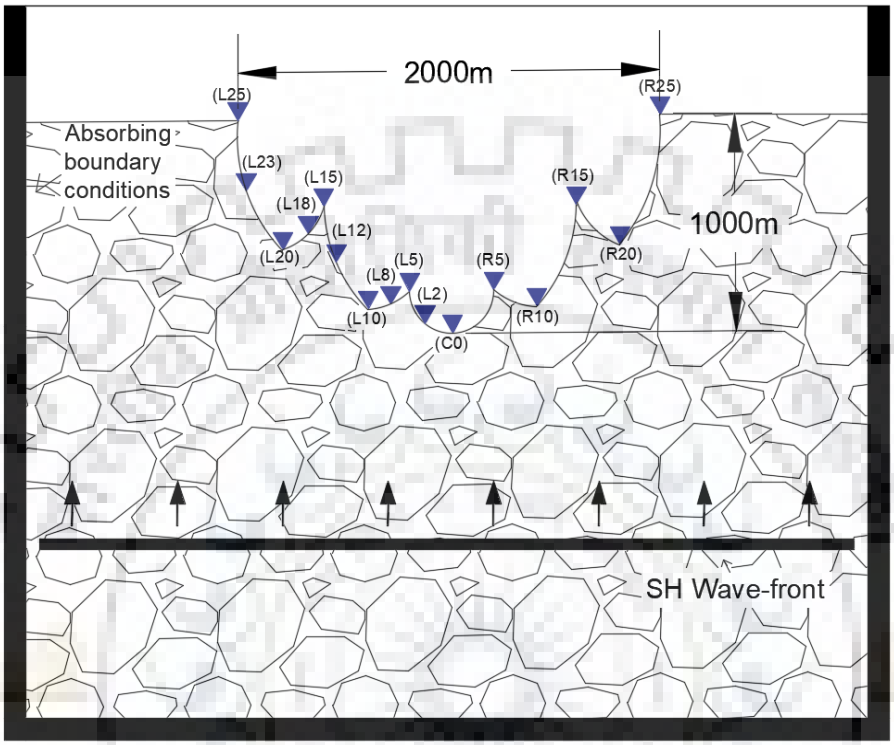

Figure 4.32 Five elliptical valley model (EV5) along with receivers array

(a) Time domain response

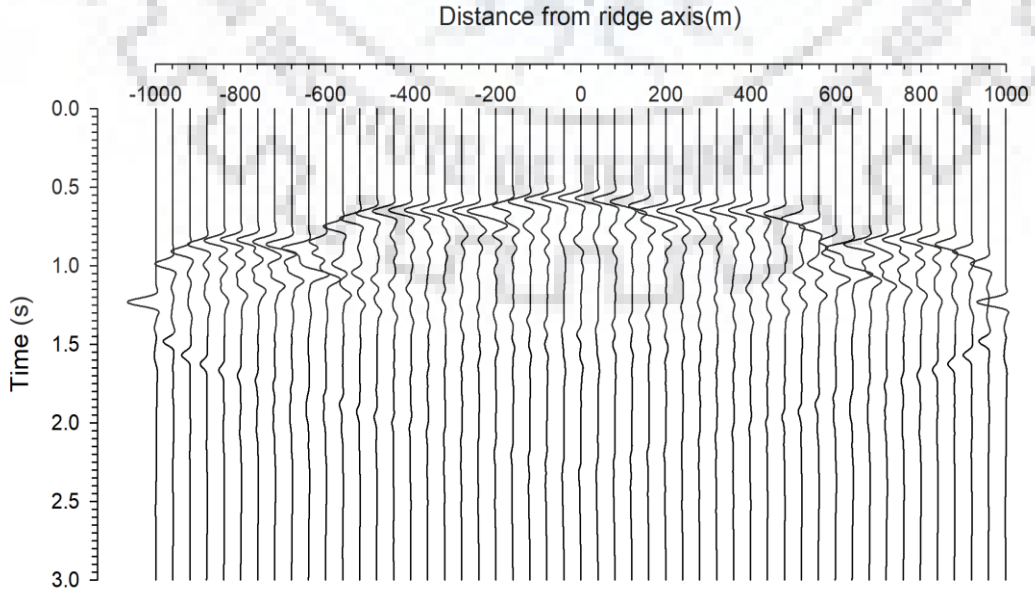

Figure 4.33 Spectral amplitude of EV5 model at various receivers along valley profile

The SH-wave response of the EV5 model is shown in figure 4.33. The analysis of this figure shows the huge amplification of SH-wave at the crest of elliptical sub-ridge and less amplification at the trough of the elliptical valley as compared to the amplitude in the case of homogenous half-space model. A drastic increase of duration of ground motion due to increase of complexity can be inferred. The incident SH-wave and the diffracted waves from the corners of the valley are very clearly visible.

(c) Spectral amplification factor

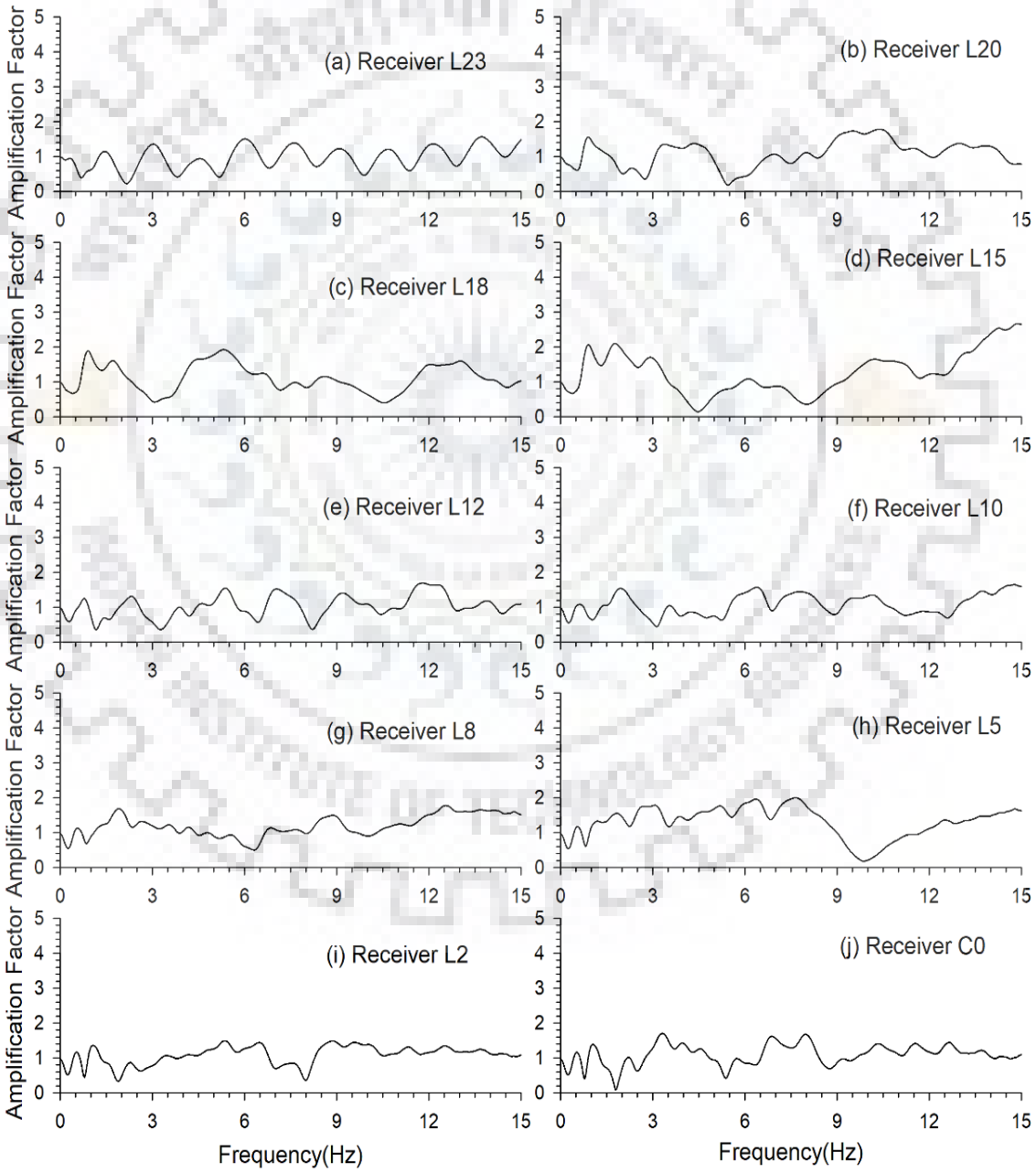

Figure 4.34 Spectral amplitude at various locations for EV5 model

Figure 4.34 shows the spectral amplification factors at different recording points along the top of the EV5 valley topography model. An analysis of table 4.8 shows that the obtained largest SAF is 2.66 and 2.0 at crest point of first and second sub-ridges, respectively. Further, at the trough point of the valley there is amplification of ground motion as compared to expected de-amplification (1.78 & 1.64 at troughs of first and second sub-valleys, respectively). ASA at the trough of the valleys also depicts an amplification of ground motion (1.08 & 1.08 at troughs of first and second sub-valleys). Amplification occurs at the trough point of center valley also (1.7). In this case, not any peak point experiences de-amplification. Amplification factor for a valley is affected by its own shape features as well as features of surrounding neighboring valleys.

Table 4.8 A comparison of spectral amplification factor (SAF) and average spectral amplification (ASA) at different receiver points

Receivers	L23(f)	L20(t)	L18(f)	L15(c)	L12(f)	L10(t)	L8(f)	L5(c)	L2(f)	C0(t)
Largest SAF	1.57	1.78	1.92	2.66	1.69	1.64	1.77	2	1.49	1.7
Average SAF	0.96	1.08	1.1	1.27	1.02	1.08	1.2	1.3	1.08	1.1

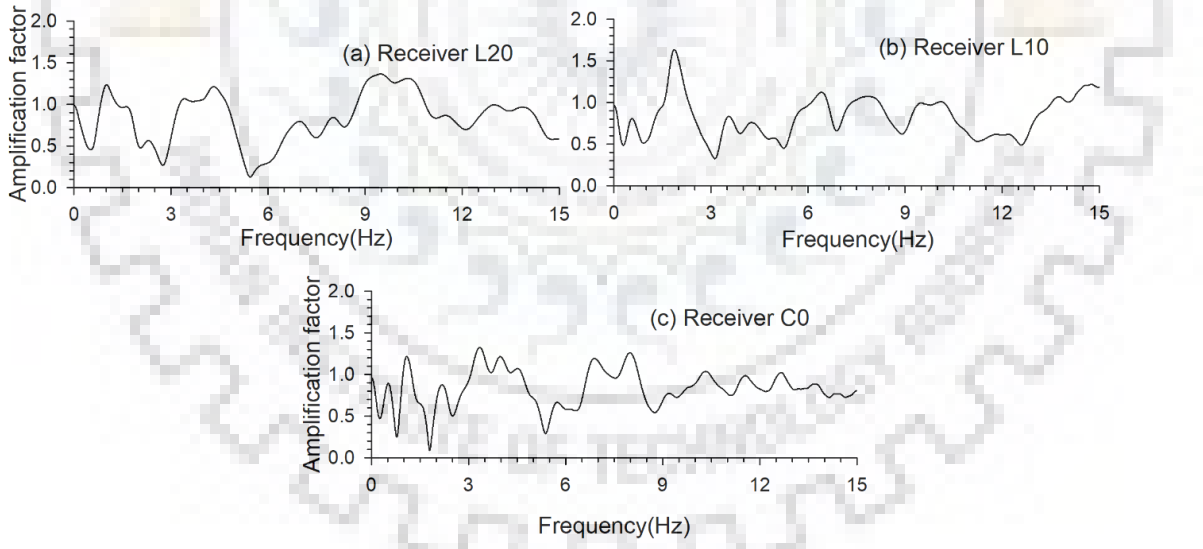

Figure 4.35 Spectral amplification at the trough of the valleys wrt the record at the ground level

The spectral amplification at the trough of the valleys wrt the record at the top corners of the valley, as shown in figure 4.35, depicts that the obtained largest SAF is 1.35 at frequency 9.34 Hz, 1.62 at frequency 1.87 Hz at the center of the first and second sub-valleys, respectively. Similarly, the obtained largest SAF is 1.32 at frequency 3.35 Hz at the trough of the central valley.This is lesser than the same obtained numerically.

4.5.4 SH-wave response of seven elliptical valleys

A topography model with seven elliptical valley EV7 is shown in figure 4.36. The SH-wave response of the model is computed at 51 recording points, extending from -1000m to 1000 m at an interval of 40 m spacing in the horizontal direction.

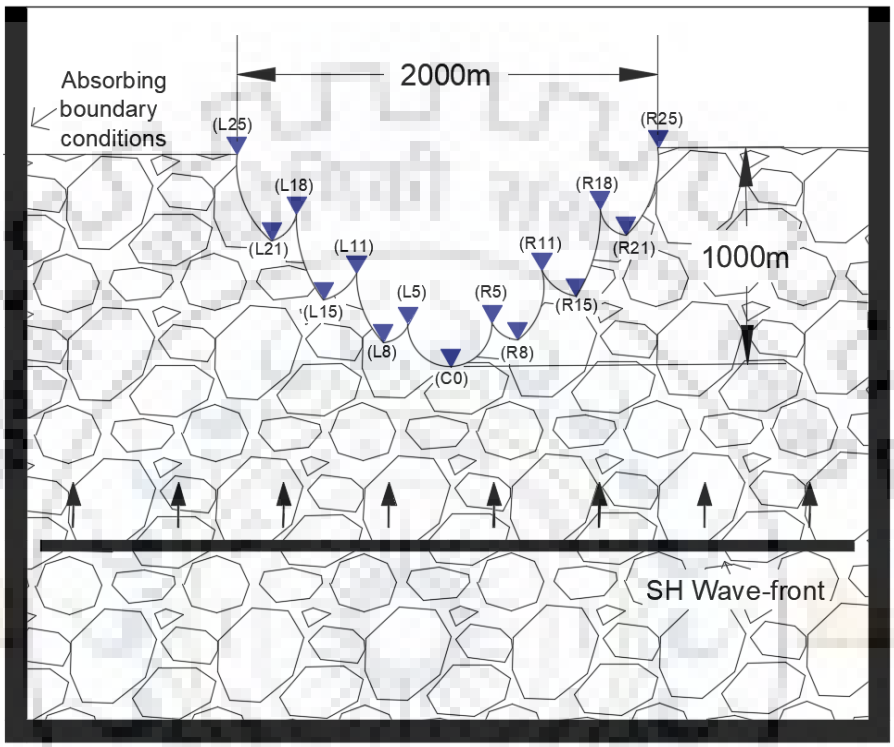

Figure 4.36 Seven elliptical valley model (EV7) along with receivers array

(a) Time domain response

The SH-wave response of the EV7 model is shown in figure 4.37. The analysis of this figure shows the amplification of SH-wave at the crest of elliptical ridge and less amplification at the trough of the elliptical valley as compared to the amplitude in the case of homogenous half-space model. A drastic increase in duration of ground motion due to increase of complexity can be inferred. The incident SH-wave and the diffracted waves from the corners of the valley are clearly visible.

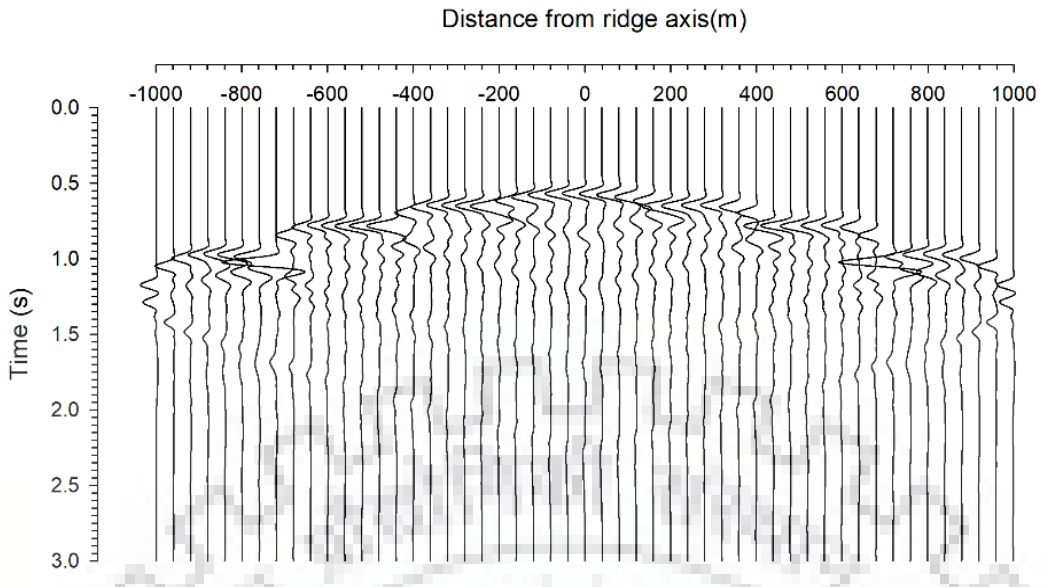

Figure 4.37 Spectral amplitude of EV7 model at various receivers along valley profile

(d) Spectral amplification factor

Figure 4.38 shows the spectral amplification factors at different recording points along the top of the EV7 valley topography model. An analysis of table 4.9 shows that the obtained largest SAF is 3.73, 2.09 and 2.1 at crest point of first, second and third sub-ridges, respectively. Further, at the trough point of the sub-valleys, there is amplification of ground motion as compared to expected de-amplification (1.89, 1.9, 1.7 at the troughs of first, second and third sub-valleys, respectively). However, ASA at the trough of the valleys depicts de-amplification (0.96 at trough of first valley) and amplification (1.08 & 1.1 at troughs of second and third sub-valleys) of ground motion. Amplification occurs at the trough point of center valley also (1.76). Amplification factor for a valley is affected by its own shape features as well as features of surrounding neighboring valleys. Diffraction andrefraction of waves occur and may be the reason of some unusual behavior in the case of multi-valleys.

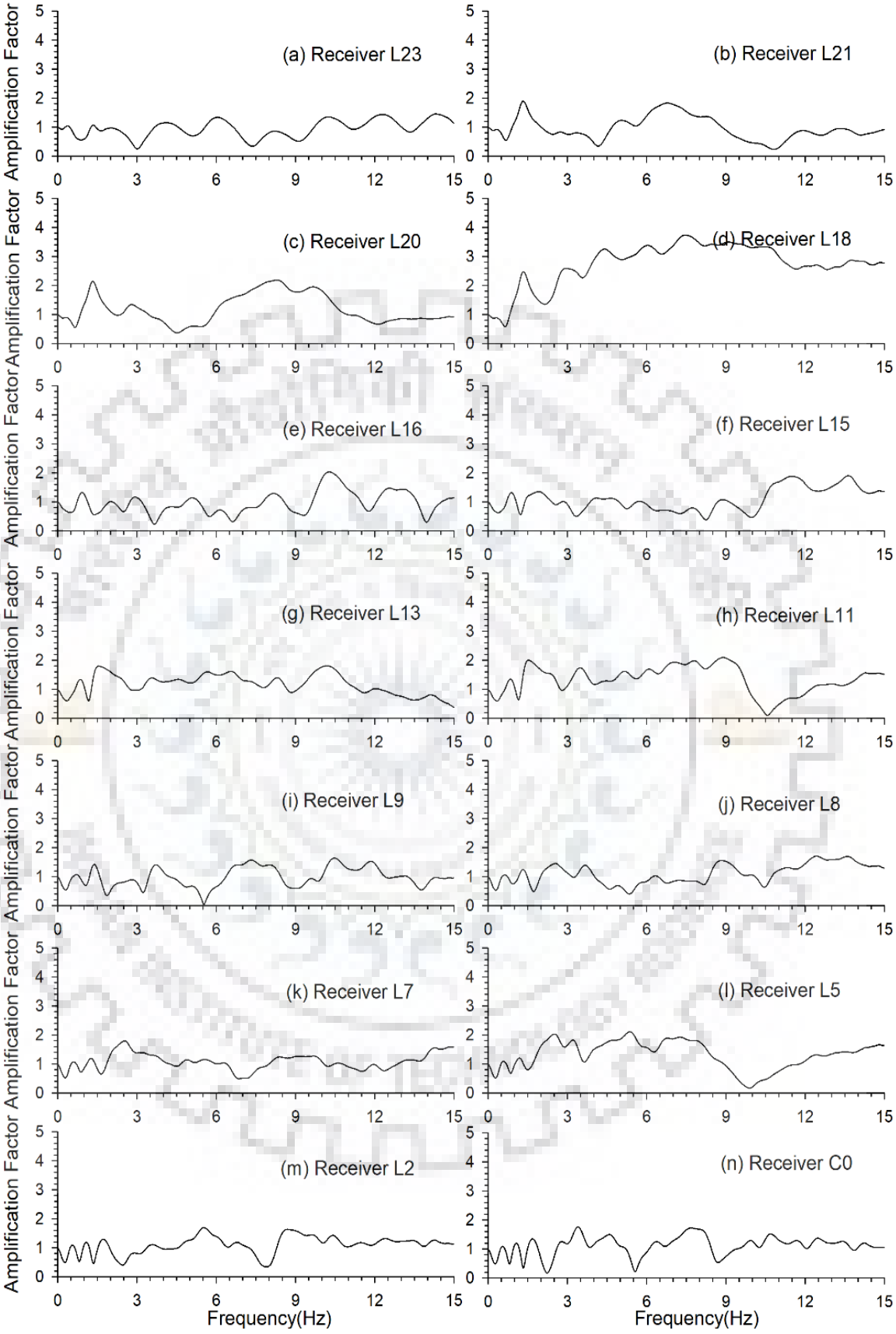

Figure 4.38 Spectral amplification factors at various locations for EV7 model

Table 4.9 A comparison of spectral amplification factor (SAF) and average spectral amplification (ASA) at different receiver points

Receivers	L23 (f)	L21 (t)	L20 (f)	L18 (c)	L16 (f)	L15 (t)	L13 (f)	L11 (c)	L9 (f)	L8 (t)	L7 (f)	L5 (c)	L2 (f)	C0 (t)
Largest SAF	1.45	1.89	2.18	3.73	2.03	1.9	1.8	2.09	1.63	1.7	1.8	2.1	1.69	1.76
Average SAF	0.95	0.96	1.19	2.74	0.96	1.08	1.17	1.33	0.98	1.1	1.08	1.31	1.1	1.11

The spectral amplification at the trough of the valleys wrt the record at the the top corners of valley, as shown in figure 4.39, depicts that the obtained largest SAF is 4.2 at frequency 4.5 Hz, 11.25 at frequency 4.24 Hz, 7.5 at frequency 4.18 Hz at the center of the first ,second, third sub-valleys, respectively which seems unreliable. Similarly, the obtained largest SAF is 12.1 at frequency 4.2 Hz at the trough of the central valley. This is much larger than the same obtained numerically.

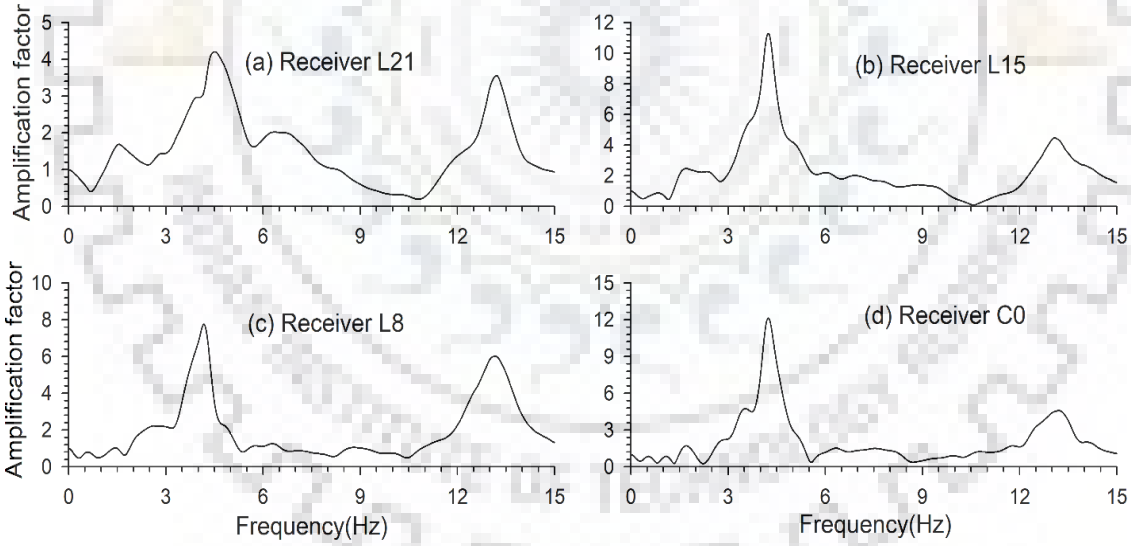

Figure 4.39 Spectral amplification at the trough of the valleys wrt the record at the ground level

4.6 COMPARISON OF RESULTS BETWEEN TRIANGULAR AND ELLIPTICAL VALLEYS

4.6.1 Single triangular valley (TV1) and elliptical valley (EV1)

A comparison of the amplification of SH-wave in the case of TV1 and EV1 models at two locations is shown in the figure 4.40. The amplification at the center of TV1 valley is less than that on the EV1 valley. Table 4.10 also depicts that amplification occurs in the case of EV1 while de-amplification occurs in the case of TV1 at the center of valley. Similarly, a comparison of spectral amplification of the SH-wave along the flank of the TV1 and EV1 model at two locations is shown in figure 4.40. It shows that ASA along the flanks of the TV1 model is less than those along the EV1 model.

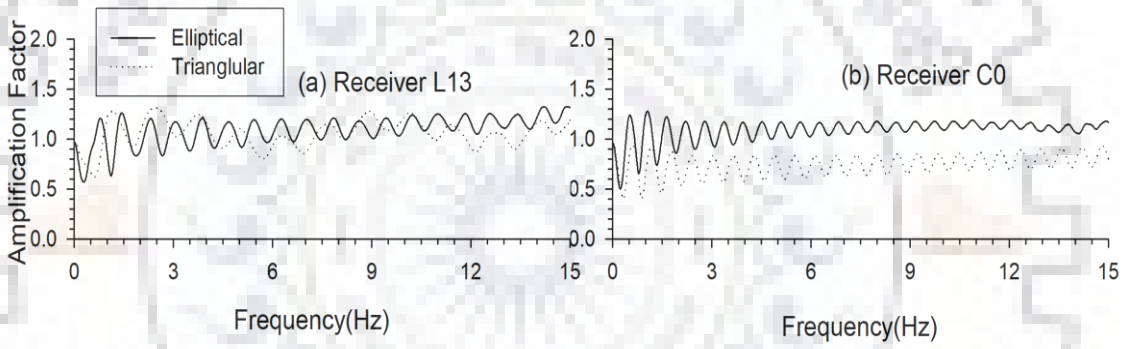

Figure 4.40 A comparison of SH-wave responses and spectral amplification at the TV1 and EV1 model at two locations

Table 4.10 A comparison of average spectral amplification (ASA) obtained along the TV1 and EV1 ridge models at different receiver points

Receiver	L13(flank)	C0(crest)
ASA: Triangular	1.05	0.75
ASA: Elliptical	1.09	1.09

4.6.2 Three triangular valleys (TV3) and elliptical valleys (EV3)

A comparison of spectral amplification of the SH-wave at different locations along the TV3 and EV3 models is shown in figure 4.41. At the trough points of the TV3 valley, the spectral amplification is relatively less than to those on the EV3 model. Table 4.11 also depicts that amplification occurs in the case of EV3 while de-amplification occurs in the case of TV3 at the trough points of valley. Further, at the crest of sub-ridges, ASA for EV3 model is more than that for TV3 model, that means more amplification occurs at crest of sub-ridge in case of EV3 than TV3. On the other hand, along the flanks of the valley ASA is larger in the case of TV3 model than EV3 model. For example, at location L13, the obtained ASA are 1.48 and 1.14 in the case of TV3 and EV3 models, respectively.

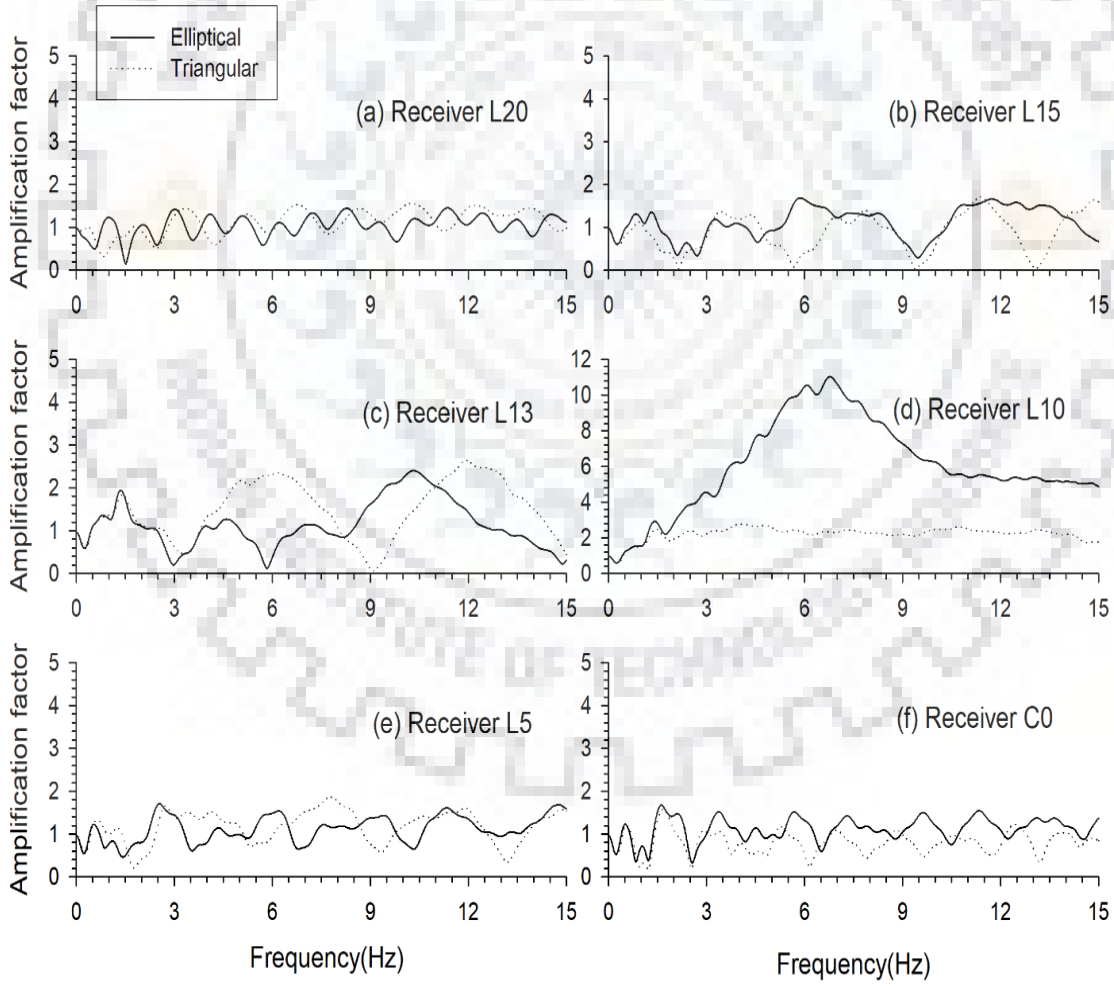

Figure 4.41 Comparison of spectral amplification factors for the TV3 and EV3 topography models

Table 4.11 A comparison of average spectral amplification (ASA) obtained along the TV3 and EV3 valley models at different receiver points

Receiver	L20(flank)	L15(trough)	L13(flank)	L10(crest)	L5(flank)	C01(trough)
ASA: Triangular	1.13	0.88	1.48	2.22	1.17	0.8
ASA: Elliptical	1.04	1.12	1.14	6.05	1.12	1.1

4.6.3 Five triangular valleys (TV5) and elliptical valleys (EV5)

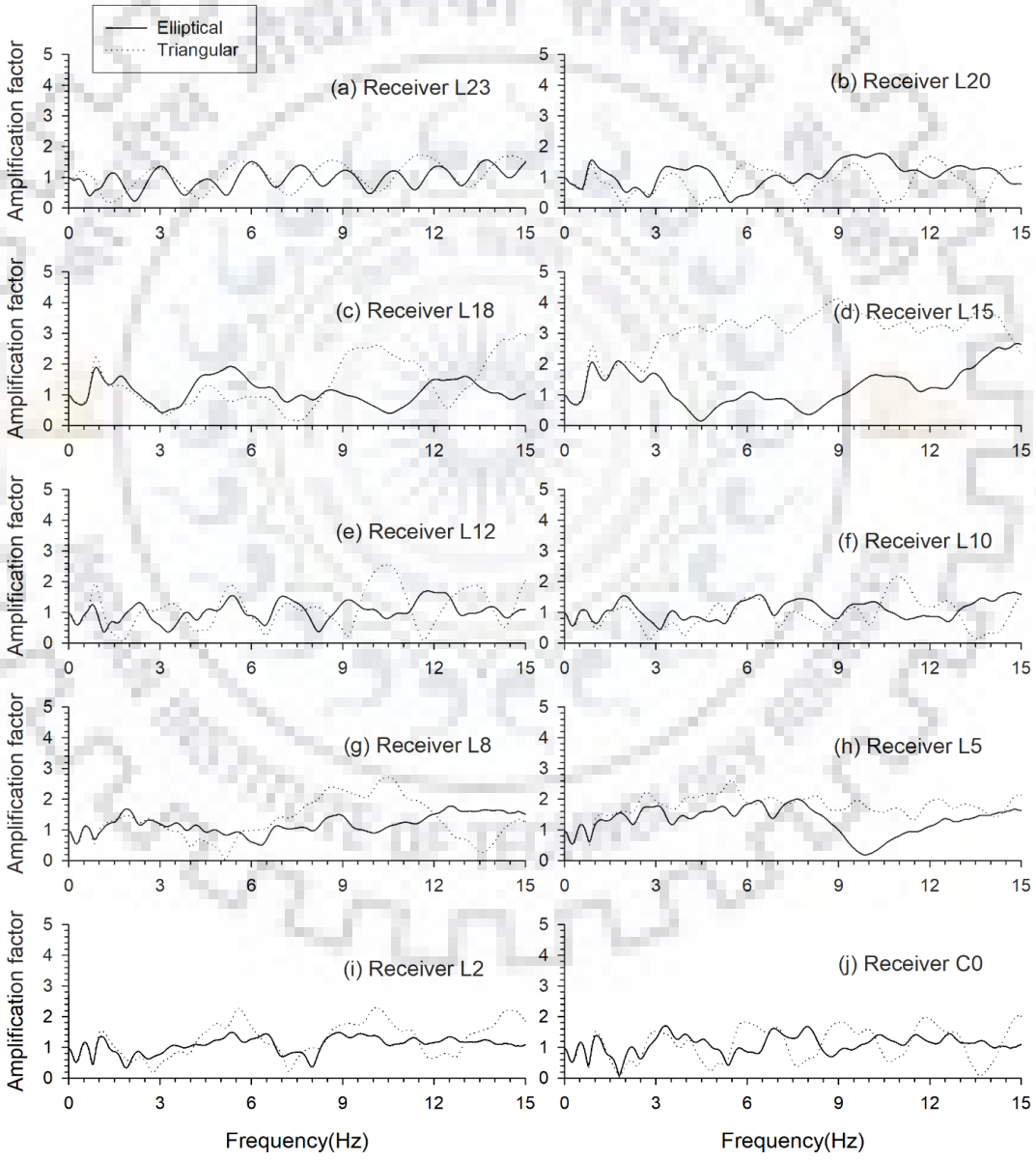

Figure 4.42 Comparison of spectral amplification factors for the TV5 and EV5 topography models

A comparison of spectral amplifications of the SH-wave at different locations along the TV5 and EV5 models is shown in figure 4.42. At the trough points of the EV5 valley, the spectral amplification is relatively more than those on the TV5 model. Table 4.12 also depicts that amplification occurs in the case of EV5 while de-amplification occurs in the case of TV5 at the trough points of valley (except at center valley). Further, at the crest of sub-ridges, ASA for TV5 model is more than that for the EV5 model, means more amplification occurs at crest of sub-ridges in case of TV5 than EV5. Also, along the flanks of the valley, ASA is larger in the case of TV5 model than EV5 model. For example, at location L18, the obtained ASA are 1.35 and 1.1 in the case of TV5 and EV5 models, respectively.

Table 4.12 A comparison of average spectral amplification (ASA) obtained along TV5 and EV5 valley models at different receiver points

Receivers	L23(f)	L20(t)	L18(f)	L15(c)	L12(f)	L10(t)	L8(f)	L5(c)	L2(f)	C0(t)
ASA Triangular	1.04	0.85	1.35	3	1.1	0.92	1.3	1.77	1.26	1.1
ASA Elliptical	0.96	1.08	1.1	1.27	1.02	1.08	1.2	1.3	1.08	1.1

4.6.4 Seven triangular valleys (TV7) and elliptical valleys (EV7)

A comparison of spectral amplification of the SH-wave at different locations along the TV7 and EV7 models is shown in figure 4.43. At the trough points of the EV7 valley, the spectral amplification is relatively more than to those on the TV7 model. Table 4.12 also depicts that amplification occurs in the case of EV7 while de-amplification occurs in the case of TV7 at the trough points of valley (except in first valley). Further, at the crest of sub-ridges, ASA for TV7 model is more than that for EV7 model, means more amplification occurs at crest of sub-ridges in case of TV7 than EV7. On the other hand, along the flanks of the valleys at certain location ASA is larger in the case of TV7 model and at certain location ASA is larger in the case of EV7 model.

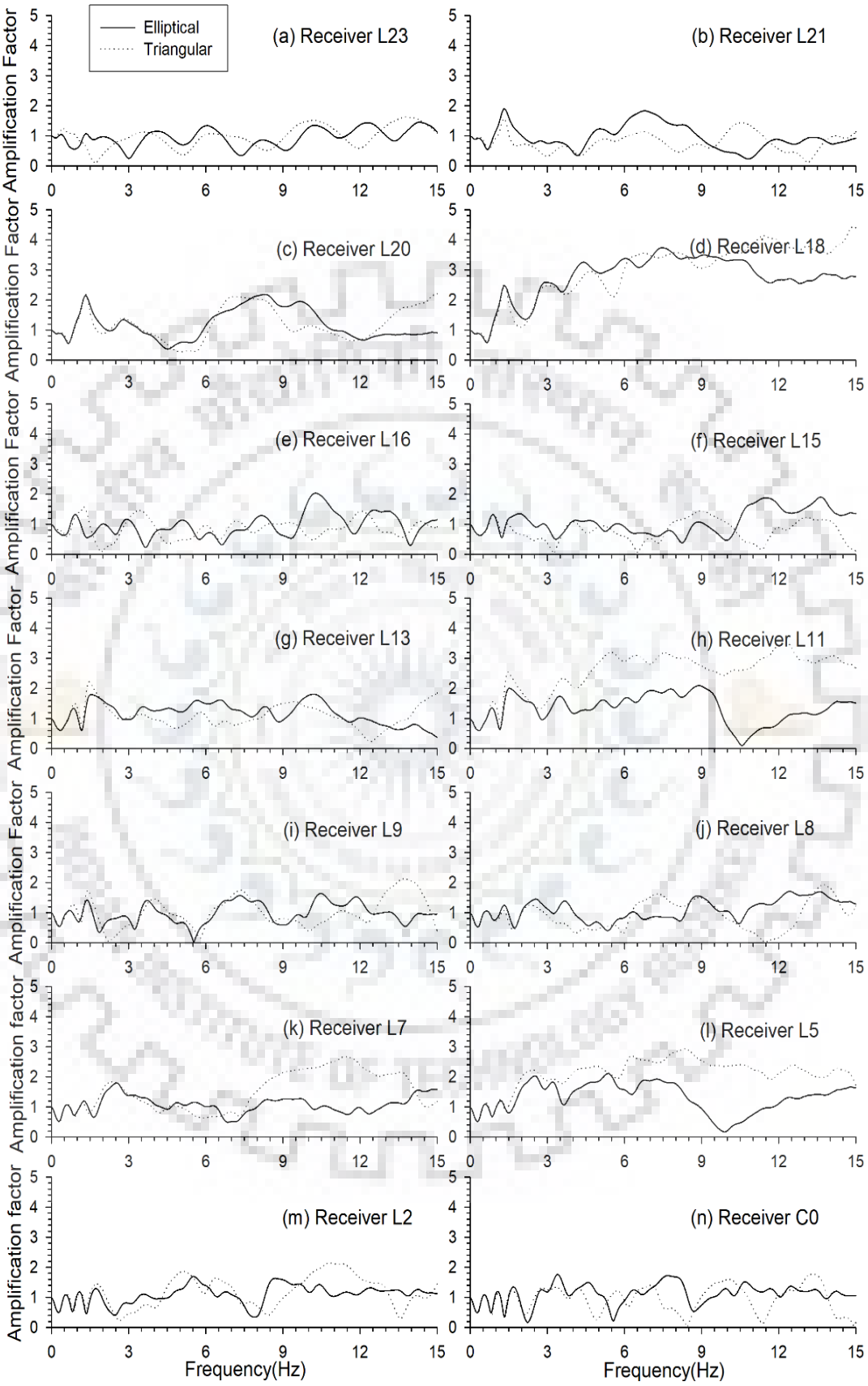

Figure 4.43 Comparison of spectral amplification factors for the TV7 and EV7 topography models

Table 4.13 A comparison of average spectral amplification (ASA) obtained along TV7 and EV7 valley models at different receiver points

Receivers	L23 (f)	L21 (t)	L20 (f)	L18 (c)	L16 (f)	L15 (t)	L13 (f)	L11 (c)	L9 (f)	L8 (t)	L7 (f)	L5 (c)	L2 (f)	C0 (t)
ASA Triangular	0.98	0.78	1.2	3	0.85	0.79	1.07	2.55	1.02	0.91	1.51	2.12	1.17	0.95
ASA Elliptical	0.95	0.96	1.19	2.74	0.96	1.08	1.17	1.33	0.98	1.1	1.08	1.31	1.1	1.11

CHAPTER #5

CONCLUSIONS

The SH-wave responses of single and multi-ridges and valleys of both triangular and elliptical shapes have been simulated and analysed. Based on the result following conclusions can be drawn:

5.1 SEISMIC RESPONSE OF COMPLEX RIDGE TOPOGRAPHY

a) Grounds motions are amplified on tops of ridges due to their convex features which causes focusing of waves.
b) Amplification of seismic waves are frequency dependent in the case of ridges i.e. it has maximum value at wavelength comparable to base width of ridge.
c) Maximum and average amplification factor obtained by numerical modelling is usually greater than analytical value. This may be because of non-consideration of diffracted waves in the analytical solution.
d) In case of multi-ridges, amplification of SH-wave is found at the crest of sub-ridges and de-amplification is found at trough of sub-valleys as compared to the amplitude in the case of homogenous half-space model.
e) Apex angle or shape ratio is major factor for governing amplification factor. Amplification can be found greater at ridges of low height with less apex angle than ridges of more height with more apex angle.
f) Presence of neighbouring ridges affects the amplitude of ground motion. Interference occurs between reflected and diffracted waves from adjacent ridges produces varying amplitude and this may be the reason of some unusual behaviour in the case of multi-ridge topography.
g) The spectral amplifications at the top of ridge with respect to the record at the base, shows much larger value than the same obtained using numerical/analytical one. So, it may be the reason behind the reported very large amplification in the case of amplification computed using the record at the top and base of the ridge.
h) ASA at ridge points is found more in the case of triangular ridges than elliptical ridges. Also, at the trough points, value of ASA is found more in triangular ridges than elliptical ridges that means more de-amplification occurs at trough points in the

elliptical ridges. ASA at flank points do not show specific trends. However it is also seen that difference between the values for these shapes decreases when number of ridges increase.

5.2 SEISMIC RESPONSE OF COMPLEX VALLEY TOPOGRAPHY

a) In the case of single valley, de-amplification is found at trough of valley due to de-focusing of waves.
b) In contrast to de-amplification at trough, amplification can be found at top corners.
c) Maximum and ASA obtained by numerical modelling is usually greater than analytical value. This may be because of non-consideration of diffracted waves in the analytical solution.
d) At trough of sub-valleys, ASA shows de-amplification whereas at crest of sub-ridges, it shows amplification in case of multi-valley.
e) In the multi-valleys, ASA at the trough of sub-valleys are lesser in case of triangular valleys than elliptical valleys i.e. more de-amplification occurs at trough points in case of triangular valleys than elliptical valleys. On the other hand, ASA at crest of sub-ridges are more in case of triangular valleys than elliptical valleys i.e. more amplification occurs at crest points in the case of triangular valleys than elliptical valleys. However, it is also seen that difference between the values for these shapes decreases when number of valleys increases.
f) Amplification near the top-corners are larger in the case of triangular valleys as compared to the elliptical valleys.
g) De-amplification caused by a valley is affected by its own shape features as well as features of surrounding neighboring valleys. Diffraction and reflection of waves occur and may be the reason of some unusual behavior in the case of multi-valleys.

REFERENCES

1. Aki, K. "Local Site Effect on Ground Motion." Earthquake Engineering and Soil Dynamics II: Recent Advances in Ground-Motion Evaluation (1988): 93-111.
2. Ashford, Scott, A., Nicholas, S., Lysmer, J., and Deng, N. "Topographic Effects on the Seismic Response of Steep Slopes." Bulletin of the Seismological Society Of America 87, no. 3 (1997): 701-709.
3. Assimaki, D., and Gazetas, G. "Soil and Topographic Amplification on Canyon Banks and the 1999 Athens Earthquake." Journal of Earthquake Engineering 8, no. 01 (2004): 1-43.
4. Assimaki, D., Gazetas, G., and Eduardo, K. "Effects of Local Soil Conditions on the Topographic Aggravation of Seismic Motion: Parametric Investigation and Recorded Field Evidence from the 1999 Athens Earthquake." Bulletin of the Seismological Society of America 95, no. 3 (2005): 1059-1089.
5. Assimaki, D., and Jeong, S. "Ground Motion Observations at Hotel Montana during the M 7.0 2010 Haiti Earthquake: Topography or Soil Amplification?" Bulletin of the Seismological Society of America 103, no. 5 (2013): 2577-2590.
6. Bard, P. Y. "Diffracted Waves and Displacement Field over Two-Dimensional Elevated Topographies." Geophysical Journal International 71, no. 3 (1982): 731-760.
7. Bard, P. Y. "Local Effects on Strong Ground Motion: Physical Basis and Estimation Methods in View of Microzoning Studies." Proceedings of the Advances Study Course Seismotectonic and Microzonation techniques in Earthquake Engineering: Integrated Training in Earthquake risk reduction practices (1999): 75-124.
8. Boore, D. M. "A Note on the Effect of Simple Topography on Seismic SH Waves." Bulletin of the Seismological Society of America 62, no. 1 (1972): 275-284.
9. Boore, D. M. "The effect of simple topography on Seismic Waves: Implications for the Accelerations Recorded at Pacoima Dam, San Fernando

Valley, California." Bulletin of the Seismological Society of America 63, no. 5 (1973): 1603-1609.

10. Boore, D. M., and Joyner, W. B., "Peak Horizontal Acceleration and Velocity from Strong-Motion Records Including Records from the 1979 Imperial Valley, California, Earthquake." Bulletin of the Seismological Society of America 71, no. 6 (1981): 2011-2038.
11. Boore, D. M., Stephen, C. Harmsen, and Sam, T. H. "Wave Scattering from a Step Change in Surface Topography." Bulletin of the Seismological Society of America 71, no. 1 (1981): 117-125.
12. Bouchon, Michel, and Jeffrey, S. Barker. "Seismic Response of a Hill: the Example of Tarzana, California." Bulletin of the Seismological Society of America 86, no. 1A (1996): 66-72.
13. Bouckovalas, George, D., and Achilleas, G. P. "Numerical Evaluation of Slope Topography Effects on Seismic Ground Motion." Soil Dynamics and Earthquake Engineering 25, no. 7-10 (2005): 547-558.
14. Çelebi, M. "Topographical and Geological Amplifications Determined from Strong-Motion and Aftershock Records of the 3 March 1985 Chile Earthquake." Bulletin of the Seismological Society of America 77, no. 4 (1987): 1147-1167.
15. Celebi, M. “Topographical and Geological Amplification: Case Studies and Engineering Implications.” Structural Safety 10(1) (1991), 199-217
16. Chaljub, E., Moczo, P., Tsuno, S., Bard, P. Y., Kristek, J., Käser, M., Stupazzini, M., and Kristekova, M. "Quantitative Comparison of Four Numerical Predictions of 3D Ground Motion in the Grenoble Valley, France." Bulletin of the Seismological Society of America 100, no. 4 (2010): 1427-1455.
17. Clayton, Robert, W., and Björn, E. "Absorbing Boundary Conditions for Wave-Equation Migration." Geophysics 45, no. 5 (1980): 895-904.
18. Davis, Lawrence, L., and Lewis, R. West. "Observed Effects of Topography on Ground Motion." Bulletin of the Seismological Society of America 63, no. 1 (1973): 283-298.
19. Durand, S., Gaffet, S., and Virieux, J. "Seismic Diffracted Waves from Topography Using 3-D Discrete Wavenumber-Boundary Integral Equation Simulation." Geophysics 64, no. 2 (1999): 572-578.

20. Emmerich, H., and Michael, K. "Incorporation of Attenuation into Time-Domain Computations of Seismic Wave Fields." Geophysics 52, no. 9 (1987): 1252-1264.
21. Faccioli, E. "Seismic Amplification in the Presence of Geological and Topographic Irregularities." International conferences on recent advances in geotechnical earthquake engineering and soil dynamics 13, (1991): 14-34.
22. Gazetas, G., Kallou, P. V., and Psarropoulos, P. N. "Topography and Soil Effects in the M S 5.9 Parnitha (Athens) Earthquake: The Case of Adames." Natural Hazards 27, no. 1-2 (2002): 133-169.
23. Geli, L., Bard, P. Y., and Béatrice, J. "The Effect of Topography on Earthquake Ground Motion: A Review and New Results." Bulletin of the Seismological Society of America78, no. 1 (1988): 42-63.
24. Gianella, Vincent, P., and Callaghan, E. "The Earthquake of December 20, 1932, at Cedar Mountain, Nevada and its Bearing on the Genesis of Basin Range Structure." The Journal of Geology 42, no. 1 (1934): 1-22.
25. Gottschammer, E., and Olsen, K. B. "Accuracy of the Explicit Planar Free-Surface Boundary Condition Implemented in A Fourth-Order Staggered-Grid Velocity-Stress Finite-Difference Scheme." Bulletin of the Seismological Society of America 91, no. 3 (2001): 617-623.
26. Graves, R. W. "Simulating Seismic Wave Propagation in 3D Elastic Media Using Staggered-Grid Finite Differences." Bulletin of the Seismological Society of America 86, no. 4 (1996): 1091-1106.
27. Griffiths, D. W., and Bollinger, G. A. "The Effect of Appalachian Mountain Topography on Seismic Waves." Bulletin of the Seismological Society of America 69, no. 4 (1979): 1081-1105.
28. Hadley, and Bardwell, J. “Landslides and Related Phenomena Accompanying the Hebgen Lake Earthquake of August 17, 1959.” US Government Printing Office, 1964.
29. Hartzell, S. H., Carver, D. L., and King, K. W. "Initial Investigation of Site and Topographic Effects at Robinwood Ridge, California." Bulletin of the Seismological Society of America 84, no. 5 (1994): 1336-1349.
30. Hatzfeld, D., Nord, J., Paul, A., Guiguet, R., Briole, P., Ruegg, J. C., and Armijo, R. "The Kozani-Grevena (Greece) Earthquake of May 13, 1995,

Ms= 6.6, Preliminary Results of a Field Multidisciplinary Survey." Seismological Research Letters 66 (1995): 61-70.

31. Israeli, M., and Orszag, S. A. "Approximation of Radiation Boundary Conditions." Journal of Computational Physics 41, no. 1 (1981): 115-135.
32. Jibson, R. "Summary of Research on the Effects of Topographic Amplification of Earthquake Shaking on Slope Stability." US Geological Survey (1987): 87-269.
33. Kawase, H., and Aki, K. "Topography Effect at the Critical SV-Wave Incidence: Possible Explanation of Damage Pattern by the Whittier Narrows, California, Earthquake of 1 October 1987." Bulletin of the Seismological Society of America 80, no. 1 (1990): 1-22.
34. Kramer, S. L. "Geotechnical Earthquake Engineering Prentice Hall." Upper Saddle River, NJ (1996).
35. Kumar, S., and Narayan J. P. "Absorbing Boundary Conditions in A Fourth-Order Accurate SH-Wave Staggered Grid Finite Difference Algorithm." Acta Geophysica 56, no. 4 (2008): 1090-1108.
36. Lee, S. J., Komatitsch, D., Huang B. S., and Tromp, J. "Effects of Topography on Seismic-Wave Propagation: An Example from Northern Taiwan." Bulletin of the Seismological Society of America 99, no. 1 (2009): 314-325.
37. Levander, A. R. "Fourth-Order Finite-Difference P-SV Seismograms." Geophysics 53, no. 11 (1988): 1425-1436.
38. Maufroy, E., Cruz-Atienza, V. M., Cotton, F., and Gaffet, S. "Frequency-Scaled Curvature as A Proxy for Topographic Site-Effect Amplification and Ground-Motion Variability." Bulletin of the Seismological Society of America 105, no. 1 (2014): 354-367.
39. Narayan, J. P., and Arafat, M. Y. "A Numerical Study of Effects of Valley-Weathering and Valley-Shape-Ratio on the Ground Motion Characteristics." Acta Geophysica 63, no. 1 (2015): 154-175
40. Narayan, J. P., Kumar, N., and Chauhan, R. "Role of Shape and Numbers of Ridges and Valleys in the Insulating Effects of Topography on the Rayleigh Wave Characteristics." Pure and Applied Geophysics (2018): 1-20.

41. Narayan, J. P., and Kumar, V. "A Fourth-Order Accurate Finite-Difference Program for The Simulation of SH-Wave Propagation in Heterogeneous Viscoelastic Medium." Geofizika 30, no. 2 (2013): 173-189.
42. Narayan, J. P., and Rai, D. C. "An Observational Study of Local Site Effects in Chamoli Earthquake." In Proceedings of Workshop on Recent Earthquakes of Chamoli and Bhuj, Indian Society of Earthquake Technology, Roorkee, (2001): 24-26.
43. Nguyen, K. V., and Gatmiri, B. "Evaluation of Seismic Ground Motion Induced by Topographic Irregularity." Soil Dynamics and Earthquake Engineering 27, no. 2 (2007): 183-188.
44. Oprsal, I., and Zahradnik, J. "Three-Dimensional Finite Difference Method and Hybrid Modeling of Earthquake Ground Motion." Journal of Geophysical Research: Solid Earth 107, no. B8 (2002): 2161-2177.
45. Rai, M. "Topographic Effects in Strong Ground Motion." PhD diss., Virginia Tech, 2015.Richter, C. F. Elementary Seismology. W. H. Freeman and Co., San Francisco (1958).
46. Sánchez-Sesma, F. J., and Campillo, M. "Topographic Effects for Incident P, SV and Rayleigh Waves." Tectonophysics 218, no. 1-3 (1993): 113-125.
47. Smith, W. D. "The Application of Finite Element Analysis to Body Wave Propagation Problems." Geophysical Journal International 42, no. 2 (1975): 747-768.
48. Spudich, P., Hellweg, M., and Lee, W. H. K. "Directional Topographic Site Response at Tarzana Observed in Aftershocks of the 1994 Northridge, California, Earthquake: Implications for Main-shock Motions." Bulletin of the Seismological Society of America 86, no. 1B (1996): S193-S208.
49. Trifunac, M. D., and Hudson, D. E. "Analysis of the Pacoima Dam Accelerogram-San Fernando, California, Earthquake of 1971." Bulletin of the Seismological Society of America 61, no. 5 (1971): 1393-1411.
50. Tripe, R., Kontoe, S., and Wong, T. K. C.. "Slope Topography Effects on Ground Motion in the Presence of Deep Soil Layers." Soil Dynamics and Earthquake Engineering 50 (2013): 72-84.
51. Tucker, B. E., and King, J. L. "Dependence of Sediment-Filled Valley Response on Input Amplitude and Valley Properties." Bulletin of the Seismological Society of America 74, no. 1 (1984): 153-165.

52. Wong, H. L., and Jennings, P. C. "Effects of Canyon Topography on Strong Ground Motion." Bulletin of the Seismological Society of America 65, no. 5 (1975): 1239-1257
53. Zahradník, J˘. Í., Moczo, P., and Hron, F. e. "Testing Four Elastic Finite-Difference Schemes for Behavior at Discontinuities." Bulletin of the Seismological Society of America 83, no. 1 (1993): 107-129.